Microwave Interaction With Magnons For Nonlinear Devices

A DISSERTATION
SUBMITTED TO THE FACULTY OF THE GRADUATE SCHOOL
OF UNIVERSITY OF MINNESOTA
BY

ANEESH VENUGOPAL

IN PARTIAL FULFILLMENT OF THE REQUIREMENTS
FOR THE DEGREE OF
DOCTOR OF PHILOSOPHY

RANDALL VICTORA, ADVISOR

SEPTEMBER 2021

Acknowledgment

First and foremost, I thank my advisor, Prof. R. H. Victora, for his invaluable guidance, unfailing support, and motivation. I thank him for all the time and effort he has provided me over the years that helped me grow professionally and, most importantly, for helping me develop immense love for my research. I am grateful to Prof. Jian-Ping Wang and Prof. John Sartori for all the knowledge, help, and advice.

I am very thankful to my dissertation committee members- Prof. Jian-Ping Wang, Prof. Rhonda Franklin, and Prof. Carme Calderer, for their time serving on the committee for both preliminary and final oral exams.

I would like to thank our collaborators from UCLA- Prof. Yuanxun Ethan Wang, and postdocs – Helen Cui and Zhi Jackie Yao for the useful discussions and insights on the M3IC DARPA project.

Thanks are due to Carlos-Brust Soria, Chimai Nguyen and Calvin of ECE IT Support for all their help in ensuring the proper functioning of the Victora group's workstations. Their guidance and promptness in resolving issues have ensured a smooth and continuous research experience over the duration of my PhD; my family – Venugopal Krishnan, Omana Raveendran and Archana Venugopal for their love and support; my wife, Vismaya Adekattu Vijayan, for her understanding. Special thanks to my cousins Prajida P.V, Prathiba P.V and Lekshmi.

Abstract

Perturbations of the magnetic order, known as spin-waves or magnons, within a ferri- or ferromagnet can exhibit nonlinear properties. The nonlinearity of the magnons can be exploited for information processing applications and for understanding fundamental aspects of nonlinear processes. When using insulators such as Yittrium iron garnet (YIG), various functionalities such as signal processing can be realized in the absence of Ohmic losses. Moreover, the small wavelengths of spin waves can also help with the miniaturization of devices. Such advantages have made magnons attractive for a wide variety of applications ranging from communications to logic circuits.

Although magnons have been studied in the past, precise understanding and the details of various nonlinear processes are still largely lacking. Device design is often based on trial-and-error approaches with regard to magnonic properties. Efficient and robust design, however, requires a deterministic understanding of material behavior. Moreover, given the long experimental cycles involved in device design, the ability to predict properties accurately is crucial. In this thesis, I will discuss the development of a high-speed CUDA-GPU (graphics processing unit)-based parallel platform to study magnons that are created by microwave excitation of magnetic materials. The goal is twofold: to enable a better understanding of nonlinear properties and to improve device design capabilities.

Device characteristics of magnet-based frequency-selective limiters (FSLs) used for microwave signal processing are studied using simulations involving rigorous

calculations of dipolar-, exchange-, and thermal-magnetic fields. These studies offer beneficial insights into the role of physical processes like higher-order scattering on the device behavior. A key requirement in many applications is the dynamic control of the *threshold field* -the minimum microwave field needed to turn on the nonlinear behavior in a magnetic sample. The ability to dynamically vary the threshold field using an additional microwave is explained analytically and demonstrated using simulations. The importance of magnon-phase in the nonlinear processes is also explicitly demonstrated. Despite the crucial role of magnon-phase in nonlinear physics, few studies focus on the impacts of magnonic phase-noise. I have developed an analytical theory to understand the impacts of magnon phase noise. The conclusions of the theory are verified using micromagnetic simulations.

Magnetic recording comprises highly nonlinear processes that, unlike perturbative effects, involve the reversal of magnetization. Using micromagnetic simulations, I designed a high-density magnetic recording scheme employing state-of-the-art heat-assisted and bit-patterned techniques. Even after considering noise factors such as jitter and track misregistration, the design provides an extremely high density of 16 Terabits per square centimeters (Tbpsi).

Table of Contents

List of Tables

List of Figures

Chapter 1 Introduction

Due to the ever-improving understanding of nonlinear magnetic physics, is increasingly becoming popular for a wide variety of applications. In this thesis, we study the interaction of electromagnetic waves with magnetic materials. Such interactions can be broadly divided into three categories: (1) Low magnetic field-intensity studies, e.g., FMR studies that are largely linear. These studies employ microwave or radio-frequency (RF) intensities approximately in the range of deci-Oersteds. **(2)** Moderate field-intensity studies, e.g., microwave-magnet interactions in communication devices like radars. These lead to lower-degree nonlinear processes in magnetic materials, e.g., three- and four-magnon processes. These are also termed high-power studies when compared to (1) with RF intensities around a few Oersteds (Oe). **(3)** Extremely high magnetic field-intensity studies, e.g., magnetic hard disk recording application. These lead to highly nonlinear processes in the magnetic material involving magnetization reversal. The intensity of magnetization is often thousands of Oersteds.

For the first two, a strong DC bias field is used to saturate the magnetic material and the microwave excitation with a field intensity of up to a few Oe acts as a perturbation. The material, consequently, remains magnetically saturated. In the last case, however, the magnetic field is strong enough to exceed the coercivity of the magnetic material. The goal is to switch the magnetic state of the material- a highly nonlinear process. Such recording studies are often performed in the near-field approximation of electromagnetic propagation. The first two studies should ideally be carried out in the far-field approximation; however, due to the relatively small dimensions of the magnetic samples

involved (a few 10s of micrometers) when compared with the wavelength of the microwave involved (a few centimeters), we make use of the quasi-static approximation while setting up simulations, wherein the propagation effects are ignored, and a uniform field distribution is assumed throughout the sample at any instant.

The high-power studies are capable of giving rise to interesting nonlinear interactions that are important not just from a fundamental physics perspective but also from the point of view of applications. In this thesis, I will discuss aspects of nonlinear processes in magnetic materials from both viewpoints.

1.1 Magnetic nonlinear phenomena: Overview and Significance

Due to its nonlinear characteristics, magnetics has been predicted to be capable of providing unprecedented technological advancement to diverse fields like communication (mobile phones, GPS, satellite, radars) [1-4], computation [5], [6], information transfer [7], [8], cavity magnonics [9], [10], etc. The widespread applications are due to the ability of *magnons* or quantized *spin waves* to carry, transport, and process information similar to electrons in electrical/electronic circuits. A spin wave is a 'perturbation' in the magnetic ordering of a material that can propagate in the form of a wave. Wave-particle duality allows us to consider this wave as a quasiparticle known as a magnon. (In this thesis, I use the two terms - spin-wave and magnon, interchangeably. Although initially, the term spin wave was reserved for exchange modes.)

Magnons in insulators are free of ohmic losses, thereby providing a highly efficient paradigm by minimizing energy dissipation compared with the traditional charge-based

paradigm. Moreover, spin-wave-based applications can take advantage of nonlinear wave interactions, leading to smaller footprints than conventional electron-based devices. In addition, their nonlinear properties can be controlled using material parameters (e.g., film thickness, magnetization, magnetic damping, etc.) and external stimuli (e.g., microwave signal, electric currents, etc.), making them suitable for nonlinear frequency-sensitive applications. Magnons have opened new perspectives and are being used to solve hitherto intractable problems [5], [11].

Experimentally, the recent research interest in magnonics can be attributed to the developments in the growth and characterization techniques for magnetic materials. There has been a concomitant increase in computational research due to the availability of modern-day advanced computational prowess. The use of parallel programming languages like CUDA [12], [13] on Graphics Processing Units (GPU) [14] provides unprecedented compute capabilities that allow detailed studies of magnon processes. Such studies were unreasonable in the past due to the overwhelming resource and time requirements. The CUDA-GPU-based parallel programming has allowed speed up of computations of approximately 100x, allowing results that would have needed close to a year to be obtained in a few days. Such parallel programming approaches have allowed studies to be performed with significantly improved spatial and temporal resolution. In Chapter 2, I will describe the construction of such a scientific computational tool for studying the behavior of magnons under microwave excitation. It is to be noted that there are aspects of magnon studies that are still inaccessible using laboratory-based experiments, making simulation-

based studies beneficial for understanding magnon behavior. Such considerations make accurate computational capabilities even more important.

Exciting phenomena have been discovered due to research improvements leading to a better understanding of the physical principles involved in magnetics. This has resulted in the proposal of various interesting magnon-based technologies. Some of the major examples include magnon spintronics [15], [16], microwave signal processing devices [17]-[21], novel computational paradigms (like reservoir [22] and neuromorphic computation [23], [24], etc.). However, be it from the perspective of magnetics-based logic devices that can aid the traditional CMOS technology or from the perspective of more exotic applications like quantum devices [25], significant challenges exist in nonlinear magnetics at a fundamental level.

One of the major limiting factors is the lack of understanding of nonlinear processes and the consequent inability to predict the behavior of the magnetic system under external inputs, e.g., microwave or radio-frequencies, lasers, etc. The overall goal of this thesis is to enable and develop a better understanding of the physics of such nonlinear processes from the perspective of engineering applications. Mathematically, nonlinearity can be brought about by the higher-order terms in the Taylor expansion of a physical parameter. For example, consider the Talyor expansion of the energy Hamiltonian, $\mathcal{H}$, in terms of, as yet, abstract variables b^* and b. (These variables will be introduced later as the magnon creation and annihilation operators.)

$$\mathcal{H} = \sum_k \omega_k b_k b_k^* + \frac{1}{2}\sum_k hV_k b_k^* b_{-k}^* \cos(\omega_p t) + \cdots \tag{1.1}$$

The ω_k in the first term identifies the energy of the *k*th mode. The inclusion of the higher-order terms provides a more accurate description of the energy by providing successive corrections. Another notion closely related to nonlinearity is the *parametric excitation* wherein an external agency, e.g., a microwave field of a particular frequency, excites in a ferromagnet, oscillations of the magnetic moments at a different frequency. This is shown schematically in Fig. 1.1.

Nonlinearity and parametric excitation will be recurring themes in much of this thesis; however, they are not just limited to the field of magnetics. Nonlinearity is an

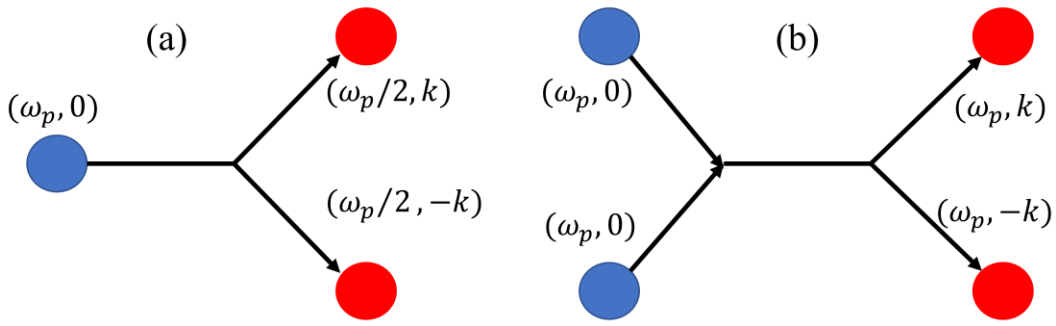

Fig 1.1. Schematic of parametric process. (a) An incoming particle of frequency, ω_p, giving rise to two particles of half the energy with opposite wave-vectors. (b) Two incoming particles of frequency, ω_p, giving rise to two particles of the same energy with opposite wave-vectors.

unavoidable facet of many natural processes. It often governs crucial processes in multiple fields of science and engineering, e.g., hydrodynamics [26], oceanic waves [27], weather patterns [28], optics [29], plasma physics [30], electronic circuits [31]-[33], liquid crystals [34], chemical reactions [35], etc. At the heart of all such fields is the ability to excite parametrically the oscillations of some order parameter using an external agency. The

excited modes can further interact amongst each other, giving rise to interesting nonlinear and scattering phenomena. For example, sea/oceanic waves during extreme weather conditions like hurricanes, storms, etc., can give rise to very destructive rogue waves in oceans [36]. Not accounting for nonlinear ~1 Hz oscillations (1/2 of the human walk frequency of ~2 Hz) while designing the *Millienium Bridge* (U.K, 2000) lead to strong oscillations when the number of people on the bridge exceeded a certain threshold. (Subsequently, it was closed down for two years before reopening in 2002 after a further expenditure of several million Pounds [37], [38].) Nonlinearity can hence be a boon or a bane depending on the application; it is worthwhile to understand such effects for efficient design. Thanks to the underlying mathematical similarity, results obtained in a field can motivate discoveries in other fields. An example of this is described in Chapter 6, wherein I have used principles from hydrodynamics to understand phase-noise in ferromagnets. Historically though, it is often the studies in magnetism that have led to insights and discoveries in other fields, e.g., weather [39], hydrodynamics [40], chaos theory [41], [42], etc.

1.2 Frequency Selective Limiter: A Nonlinear Application

Nonlinear behavior is much sought after in many electrical applications, as mentioned earlier. In this thesis, we try to understand the governing physical principles of nonlinear processes that arise when ferro(ferri)magnetic materials are subjected to microwave signals. We will explore these processes in the light of practical applications; specifically, I would use the example of the *Frequency Selective Limiter* (FSL), a

frequency-sensitive device used in communication. FSLs are devices used at the front end of communication receivers to selectively reduce the incoming high-power noise. Applications such as radars must handle undesired high-power microwave signals while distinguishing them from information signals. Other applications of FSL include filter bank receivers for signal spectrum identification, multi-channel satellite communication, and anti-jamming receivers.

a) FSL functionality

The input to the FSL can be thought of as a sequence of microwave frequencies of various strengths. The signals above a certain preset strength threshold must be *limited* in order to protect the receiver. Fig. 1.2 shows a schematic input to the FSL and the corresponding output signal. The P_{th} represents the power threshold beyond which the signals are limited. The limiting of strong signals can be achieved using a transfer function that dynamically develops notches corresponding to those frequencies that exceed the threshold; the goal is hence to realize such a transfer function.

b) FSL basic model

Next, let us look at a basic functional model that illustrates qualitatively the role played by the nonlinear ferromagnetic material in the realization of the FSL. Consider two resonant tanks with frequency ω_p and $\omega_p/2$. The latter tank contains a nonlinear element. The schematic is shown in Fig. 1.3. When the input signal at the frequency ω_p is below the threshold power (P_{th}), it appears without any attenuation at the output. However, if the

incoming frequency has strength above the threshold, oscillations at the frequency $\omega_p/2$ are excited by the nonlinear element in the subsidiary tank. Consequently, part of the input energy is coupled to the subsidiary tank to maintain the subharmonic oscillation, thereby reducing the strength of the signal that makes it to the output. It is primarily this mechanism that restricts or limits the signal strength in Fig. 1.2. As the input strength increases, the subharmonic oscillations increase, maintaining the output power constant.

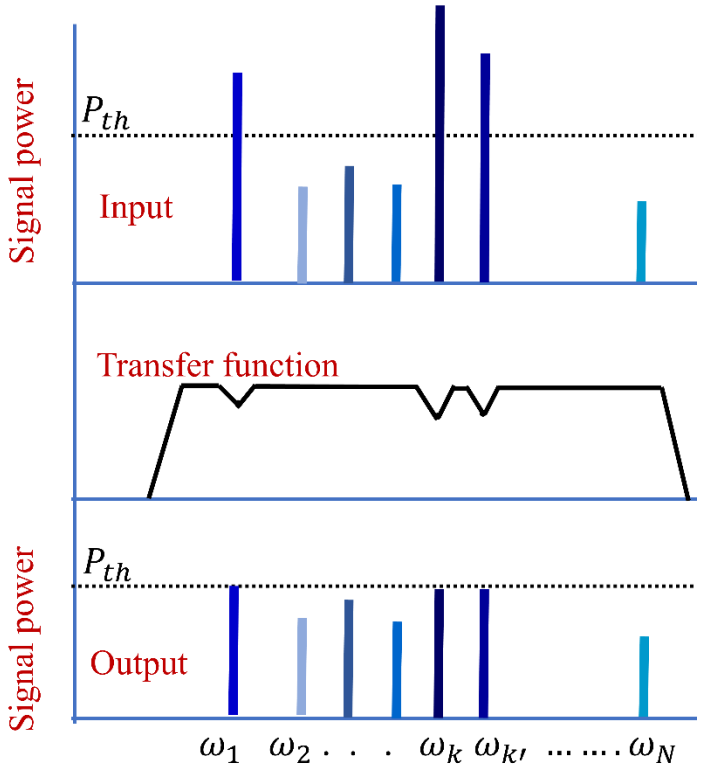

Fig. 1.2. Frequency Selective Limiter (FSL) functionality. Signals at frequencies ω_1, ω_k, and $\omega_{k'}$ that exceed the threshold power, P_{th} , are limited by the FSL.

The nonlinear element, in our case, is basically a parametric oscillator wherein the incoming high-power microwave initiates oscillations of magnetizations leading to the absorption of microwave power.

It would be appropriate to discuss the notion of spin waves and magnons at this point. However, let us briefly discuss ferromagnetic resonance, for it not only introduces the need and significance of spin waves but would also serve to establish basic terminologies and concepts involved in the study of spin waves and magnons that will be used throughout this thesis.

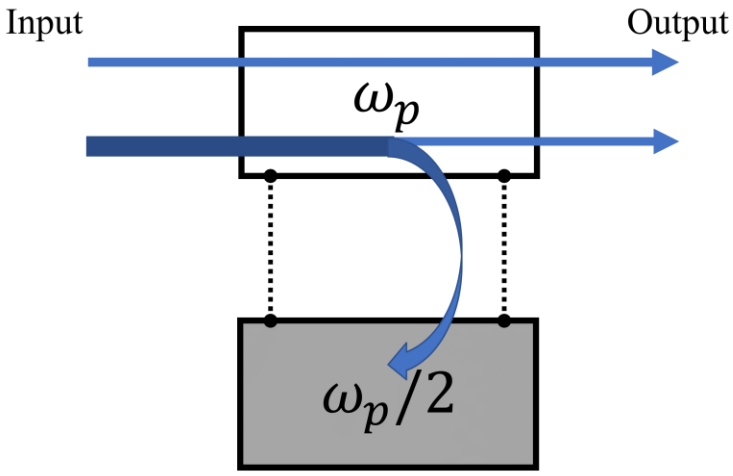

Fig. 1.3. A simple subharmonic oscillator model of FSL. The main tank has a resonant frequency of ω_p, while the subsidiary tank has a parametric oscillator at $\frac{\omega_p}{2}$, that dissipates away part of the energy of the high-power signal.

1.3 Ferromagnetic Resonance (FMR)

Ferromagnetic resonance (FMR) constitutes one of the widely studied and used magnetic characterization techniques. The first FMR studies were performed by V. K. Arkad'ev in 1912 [43]. However, it was in the 1940s that rapid development of this technique was first observed. FMR was actively employed for radar and radio-frequency

(RF) spectroscopy applications. To understand the phenomenon of FMR, we begin with the classical equation of motion of magnetization proposed by Landau and Lifshitz [44] in 1935:

$$\frac{d\boldsymbol{M}}{dt} = -\gamma \boldsymbol{M} \times \boldsymbol{H} \tag{1.2}$$

Where **M** is the magnetization; $\boldsymbol{M} = \frac{\sum_{\Delta V} \boldsymbol{\mathcal{M}}}{\boldsymbol{\Delta V}}$, $\sum_{\boldsymbol{\Delta V}} \boldsymbol{\mathcal{M}}$ is the magnetic moment of a small but macroscopic volume, $\boldsymbol{\Delta V}$, $\boldsymbol{H}$ represents the net magnetic field, and γ is the gyromagnetic ratio. (The equation does not allow for losses which will be phenomenologically introduced later.) Multiplying both sides of Eq. (1.2) by $\boldsymbol{M}$ gives $\frac{dM^2}{dt} = 0$. This shows an important feature of the Landau Lifshitz equation – the amplitude of the magnetization, i.e., $M = |\boldsymbol{M}|$ is conserved. Hence, with one end of the vector $\boldsymbol{M}$ fixed, the other can be visualized to be moving on the surface of a sphere. This observation of M conservation is very useful for computational studies to be discussed in later chapters.

A rigorous treatment of the considerations involved in the analysis of the Landau Lifshitz equation can be found in [45], [46]. We assume the magnetic field $\boldsymbol{H}$ to be comprised of two fields: a bias magnetic field, H_0, to saturate the magnetic material and the RF (microwave) field, h_{rf}. We can then write:

$$\boldsymbol{H} = \boldsymbol{H_0} + \boldsymbol{h_{rf}}; \boldsymbol{M} = \boldsymbol{M_0} + \boldsymbol{m_{rf}} \tag{1.3}$$

and assume that $h_{rf} \ll H_0$ and $m_{rf} \ll M_0$.

Using Eq. (1.3) in Eq. (1.2) and retaining only the steady-state quantities, we get: $\boldsymbol{M_0} \times \boldsymbol{H_0} = 0$. In the first approximation, neglecting the product of ac quantities, i.e., *linearizing*, gives:

$$\frac{d\boldsymbol{m_{rf}}}{dt} + \gamma \boldsymbol{m_{rf}} \times \boldsymbol{H_0} = -\gamma \boldsymbol{M_0} \times \boldsymbol{h_{rf}} \tag{1.4}$$

If we assume h_{rf} to be harmonic in time, the linearity of Eq. (1.4) implies $m_{rf}$to be harmonic as well, i.e., $\boldsymbol{h_{rf}} \equiv \boldsymbol{h} \cos(i\omega t)$ and $\boldsymbol{m_{rf}} \equiv \boldsymbol{m} \cos(i\omega t)$, using this in Eq. (1.4), we have:

$$i\omega \boldsymbol{m} + \gamma \boldsymbol{m} \times \boldsymbol{H_0} = -\gamma \boldsymbol{M_0} \times \boldsymbol{h} \tag{1.5}$$

In Cartesian coordinates, with z-axis along $\boldsymbol{H_0}$ (or $\boldsymbol{M_0}$) we get:

$$i\omega m_{\boldsymbol{x}} + \gamma m_x H_0 = \gamma M_0 h_y;\ i\omega m_{\boldsymbol{y}} - \gamma m_x H_0 = -\gamma M_0 h_x; \text{ and } i\omega m_z = 0 \tag{1.6}$$

The solution of Eq. (1.6) is:

$$m_{\boldsymbol{x}} = \chi h_x + i\chi_a h_y;\ m_{\boldsymbol{y}} = \chi h_y - i\chi_a h_x;\ m_{\boldsymbol{z}} = 0 \tag{1.7}$$

$$\chi = \frac{\gamma M_0 \omega_H}{\omega_H^2 - \omega^2};\ \chi_a = \frac{\gamma M_0 \omega}{\omega_H^2 - \omega^2} \text{ with } \omega_H = \gamma H_0 \tag{1.8}$$

The quantities χ and χ_a represent the susceptibilities or simply the response of the magnetic system to the microwave:

$$\boldsymbol{m} = \overleftrightarrow{\chi}\boldsymbol{h} \text{ with } \overleftrightarrow{\chi} = \begin{bmatrix} \chi & i\chi_a & 0 \\ -i\chi_a & \chi & 0 \\ 0 & 0 & 0 \end{bmatrix} \tag{1.9}$$

A few important observations can be made from the case of a lossless ferromagnet considered above. First, the longitudinal component of the microwave field does not

produce any ac magnetization. Second, the transverse component of the microwave field excites a time-varying magnetization component parallel to the field and also a component perpendicular to the field but with a phase difference of $\pi/2$, as indicated by Eq. (1.7) and Eq. (1.9). This property of non-symmetry is called gyrotropy. Most importantly, it can be noted that the susceptibilities exhibit a resonant dependence with respect to ω and H_0 as indicated by the denominators in Eq. (1.8), i.e., when $\omega = \omega_H = \gamma H_0$. It is this resonant dependence that gives rise to the phenomenon of ferromagnetic resonance. It is to be kept in mind that in the treatment above, we had linearized the equation of motion by ignoring the terms involving the product of ac terms.

a) Accounting for dissipation: Landau Lifshitz Gilbert equation

Gilbert [47] introduced a dimensionless *damping parameter*, α, to account for the losses. The original Landau Lifshitz equation now becomes the Landau Lifshitz Gilbert (LLG) equation:

$$\frac{d\boldsymbol{M}}{dt} = -\gamma \boldsymbol{M} \times \boldsymbol{H} + \frac{\alpha}{\boldsymbol{M}} \boldsymbol{M} \times \frac{\boldsymbol{dM}}{\boldsymbol{dt}} \tag{1.10}$$

The LLG equation represents one of the most important equations in magnetics-based theoretical studies. It is the workhorse equation for *micromagnetics*, a numerical paradigm wherein a magnetic material is divided into multiple cells, each assigned with certain magnetization; the LLG equation is then solved for each of the cells to understand various static and dynamic properties of the system. Chapter 2 will discuss in detail the setup of a parallel-computation-based micromagnetics solver.

It can be shown that we can determine the new susceptibilities using the following substitution in Eq. (1.8): $\omega_H \rightarrow \omega_H + i\omega\alpha$. Using $\chi \equiv \chi' - i\chi''$ and $\chi_a \equiv \chi_a' - i\chi_a''$:

$$\chi' = \frac{1}{D}\gamma M_0 \omega_H [\omega_H^2 - (1-\alpha^2)\omega^2];\ \chi'' = \frac{1}{D}\gamma M_0 \omega_H [\omega_H^2 + (1+\alpha^2)\omega^2]$$

$$\chi_a' = \frac{1}{D}\gamma M_0 \omega [\omega_H^2 - (1+\alpha^2)\omega^2];\ \ \chi_a'' = 2\alpha\gamma M_0 \omega_H \omega^2$$

$$D = [\omega_H^2 - (1+\alpha^2)\omega^2]^2 + 4\alpha^2\omega_H^2\omega^2 \qquad (1.11)$$

Certain crucial observations can be made. First of all, the damping constant prevents divergences at resonance in Eq. (1.8), giving the more familiar FMR curves. It can be seen from equations Eq. (1.11) that when closer to the resonance, the smaller the damping, the higher is the absorption of microwave energy. However, when far from the resonance, the smaller the damping, the smaller the absorption.

Note that in the mathematical analysis considered above, we have linearized the LLG equation. But in doing so, we set up equations that fail to capture nonlinear phenomena. Later, in this thesis (Chapter 3), we will take into account the pertinent higher-order terms in order to capture and better understand the nonlinear behavior of the system. It must be pointed out, however, that there exist a large number of studies and/or applications where a linear model is all that is needed. Further, the only magnetic fields considered in this section were the bias and the microwave fields. This leads to a uniform precession of the magnetization units within the magnetic material. In the description so far, we have ignored two of the important fields, namely, the exchange and

demagnetization fields, which can lead to non-uniform precession, thereby leading to spin waves.

The most widely used materials are ferrimagnets (dielectrics), as ferromagnetic metals result in strong skin effects. In almost all my studies, I use Yttrium iron garnet (YIG) as the material of choice unless mentioned otherwise. YIG has been shown to possess the lowest magnetic damping of all known materials. This leads to spin-wave modes with longer lifetimes as well as larger propagation distances, making YIG interesting from a technological standpoint.

1.4 Spin-Wave and Magnon

During the operation of an FSL, the nonlinear element, ferro(i)-magnet, can absorb energy from the high-power microwave signal by creating spin waves or magnons. As described earlier, these are perturbations in the otherwise saturated magnetic material. The concept of spin waves was introduced by Bloch in 1930 [48]. For simplicity, consider a linear chain of magnetic moments biased (using an external magnetic field) to point along the same direction, as shown in Fig. 1.4. If, to this chain, we apply an external excitation, e.g., a microwave frequency, we can bring about perturbations of the magnetic moments in the form of precession. We can identify a wave with the resulting response of the chain, which is termed the spin-wave. Like any wave, we can associate with it- a wavevector, k, and a frequency, ω. (It can be seen that any given spin of the chain is out of step with the next by a certain angle, thereby defining a wavelength, $\lambda = 1/k$.)

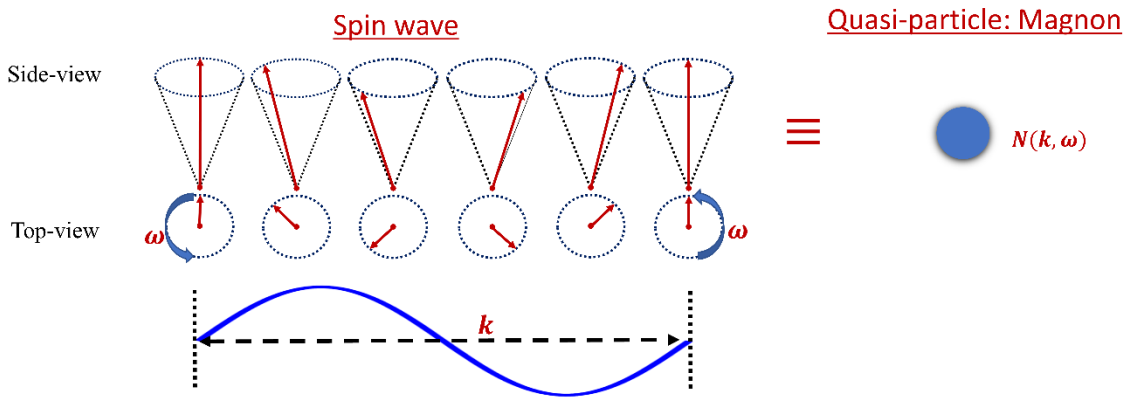

Fig. 1.4. Oscillations of the magnetic moments in a chain constitutes a wave known as spin wave, with wavevector, k, and frequency, ω. This wave can be interpreted as a *quasi*-particle known as magnon.

When $k = 0$, the spin-wave mode is called a uniform mode, wherein all the spins precess coherently. When $k \neq 0$, the waves constitute the non-uniform modes. The precessional frequency, ω, of the spins defines the frequency of the spin-wave. The second quantization allows waves to be interpreted as particles; these quantized spin waves are termed magnons. The pivotal role of the spin waves necessitates their studies both for

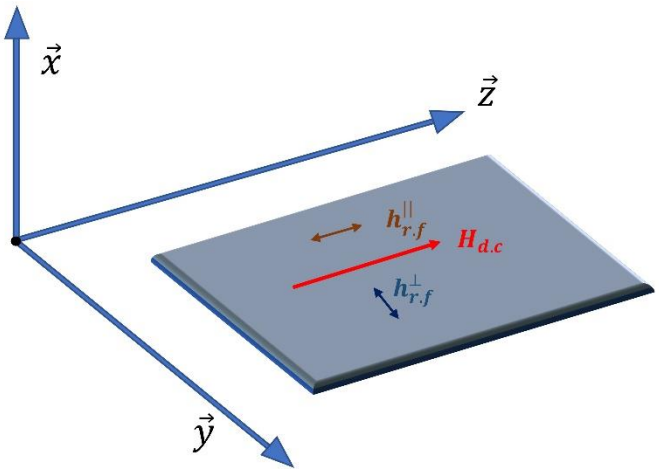

Fig. 1.5. Sample (thin film of ferri(ferro)magnet) and field configuration. $h_{r.f}^{||}$ ($h_{r.f}^{\perp}$) used for the parallel (perpendicular)-pump configuration studies in which the microwave (or RF) field is applied parallel (perpendicular) to the bias magnetic field $H_{d.c}$.

understanding their properties from a physics perspective and for the development of

design rules for engineering applications. Understanding the static and dynamic behavior of spin waves using simulation-based studies and analytical formulation is one of the main objectives of the thesis. It is to be noted that the description above is a simplistic view of the magnons. Magnetic moments in higher dimensions would similarly lead to higher dimensional spin waves. A real magnetic system would allow a wide variety of magnon modes depending on its sample size and geometry and external conditions like the magnetic bias field and temperature. In other words, the magnetic dispersion relation can be altered easily, unlike the electronic bandstructure, thus allowing for a larger degree of controllability.

1.5 Pumping Configurations

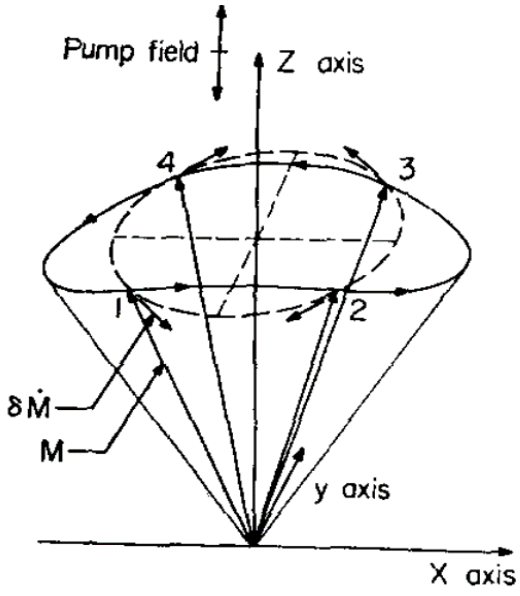

Fig. 1.6. The frequency of oscillation along z-direction is twice that of the in-plane direction, in a parallel pumping. Source: [51].

The first resonance studies carried out used perpendicular pump configuration, which still remains the most used pumping configuration. In this configuration, the microwave field is polarized in a direction perpendicular to the direction of the applied bias field. The other configuration, known as parallel pumping, was predicted independently in 1960 by Morgenthaler [49] and Schlomann *et al.* [50]. In this thesis, I make use of the latter for studying magnon properties. Fig. 1.5 shows the two configurations.

Parallel pumping allows for direct excitation of non-uniform spin-waves without the need for the intermediary uniform modes, as is usual in perpendicular pumping. In Fig. 1.6, both the bias-field and the microwave field are along the z-direction; this leads to magnetization precession, as shown therein. The precession of the magnetization is such that the frequency along the z-direction, ω_z, is twice that of the in-plane precession frequency (ω_y or ω_x) [51]. To see this, let us follow the trajectory from 1 to 4 as marked in Fig. 1.6. Since the length of the magnetization vector is constant during the precession, it can be seen that during the half-cycle of elliptical in-plane precession, the z-component executes a complete cycle.

1.6 Microwave-Magnet High-Power Interaction Studies: A Review

In this section, I include a brief list indicating some of the important nonlinear studies relevant to the current work. I must, however, mention that this by no means is a complete list.

The research of Bloembergen and Damon in 1952 [52] and that of Bloembergen and Wang in 1954 [53] on FMR at high microwave powers revealed unexpected energy absorption when the microwave strength exceeded a well-defined threshold. This was later explained theoretically by Suhl in 1957 [54], ushering in a new age of nonlinear magnetics studies. In 1959, Schlomann *et al.* [55] demonstrated that it was necessary to take into account the nonlinear interaction of parametrically generated spin waves amongst each other. He suggested that the main contribution to such interactions was through 4-magnon interactions. As mentioned before, in 1960, Morgenthaler [49] and Schlomann *et al.* [50] independently predicted parallel pumping. The parametric excitation of spin waves by a microwave parallel to the bias-field was soon demonstrated experimentally in YIG. In the late 60s the research of V.E. Zakharov, V. S. L'vov, and S. S. Starobinets [56], [57] lead to the development of S-theory, which shed new insights into the nonlinear phenomena involved with the microwave-based parametric excitation of spin waves in ferromagnets [58], [59]. Many of the claims of the S-theory were verified in the experimental works of V. Zautkin [60], [61], G. Melkov [62], and others [63]-[66]. Auto-oscillations discovered in the experiments of Hartwick, Peressini and Weiss [67] in 1961 were also explained by the S-theory. As seen earlier, there has been a tremendously increasing interest in magnon-based applications since the late 90s. The magnon-based paradigm of applications—*magnonics*—has emerged as one of the promising candidates for information transfer and data-processing technology; with the magnon phase playing an important role in notable *novel applications* like spin-wave-based logic circuits [68], reservoir computing & machine learning [22], spin-wave conduits for interconnects [69], spin-wave lens [70],

spin-based majority gate [71], and other waveguide applications [8]. They are also valuable for spintronic applications. e.g., spin-torque oscillators (STO) [72] and neuromorphic computing [23]. *Conventional applications* like telecommunication, satellite communication, and radar also use nonlinear magnetic devices to reduce energy consumption. Devices used in these applications, e.g., magnetics-based FSLs, Signal to Noise ratio Enhancers (SNEs), parametric amplifiers, etc., rely on nonlinear absorption of microwave signals. Among the linear spin-wave-based devices are delay lines, filters, resonators, directional couplers, multi-channel receivers, and Y-circulators, etc. [73]. A Bose Einstein condensate (BEC) of magnons was first demonstrated by S. O. Demokritov *et al.* in 2006 [74]. Similarly, cavity magnonics is another frontier of physics that relies on magnon-based phenomena [9, 75].

YIG-based spin-wave explorations peaked during the time frame of 1960 to 1980. YIG is still the material of choice for spin-wave-based studies, so much so that C. Kittel once said YIG is to ferromagnetic research what the fruit fly is to genetics research. It is primarily the low damping of YIG and the consequent long spin-wave (or magnon) lifetimes that allow detailed study of magnonic phenomena.

1.7 The Initial Problem

The realization of the importance of nonlinear studies in the field of magnetics is not new, and in fact, the earliest such studies date back to the times of World War II. At the time, resonance-based studies were being pursued primarily for radar, radio-frequency

spectroscopy, and radio-astronomy applications. Most of these studies were performed with low-power microwave signals. The results of high-power studies carried out in the early 50s confounded the researchers. Let us now briefly look at the results of some of the first high-power experiments [52]. These studies are pertinent even today as the exact details of some of the phenomena involved continue to remain areas of active research. Even though the materials and their geometries used in modern experiments may have changed, the results from the earliest studies are still highly relevant. This section would hence serve as an introduction to the general theme of research discussed in this thesis.

FMR studies conventionally assume small precession amplitudes of the magnetization; the response of the magnetization to the microwave under such circumstances is proportional to the strength of the microwave field. However, under high microwave power, the assumption of linearity is found to break down, resulting in nonlinear or instability effects. Phenomenological equations proposed by Bloch (similar to the Landau Lifshitz Eq. (1.2)) were successful in explaining the resonance experiments on paramagnets. The imaginary part of permeability, μ'', and the longitudinal component of magnetization, M_z, were expressed as [20], [76]:

$$\mu'' = \frac{\mu_0''}{1 + 0.25\,\gamma^2 h_{rf}^2 T_1 T_2};\; M_z = \frac{M_{z0}}{1 + 0.25\,\gamma^2 h_{rf}^2 T_1 T_2}$$

Quantities with a 0-subscript indicate the values at low microwave powers, h_{rf} is the amplitude of the microwave field, γ is the gyromagnetic ratio and T_1 and T_2 are the longitudinal and transverse relaxation times, respectively.

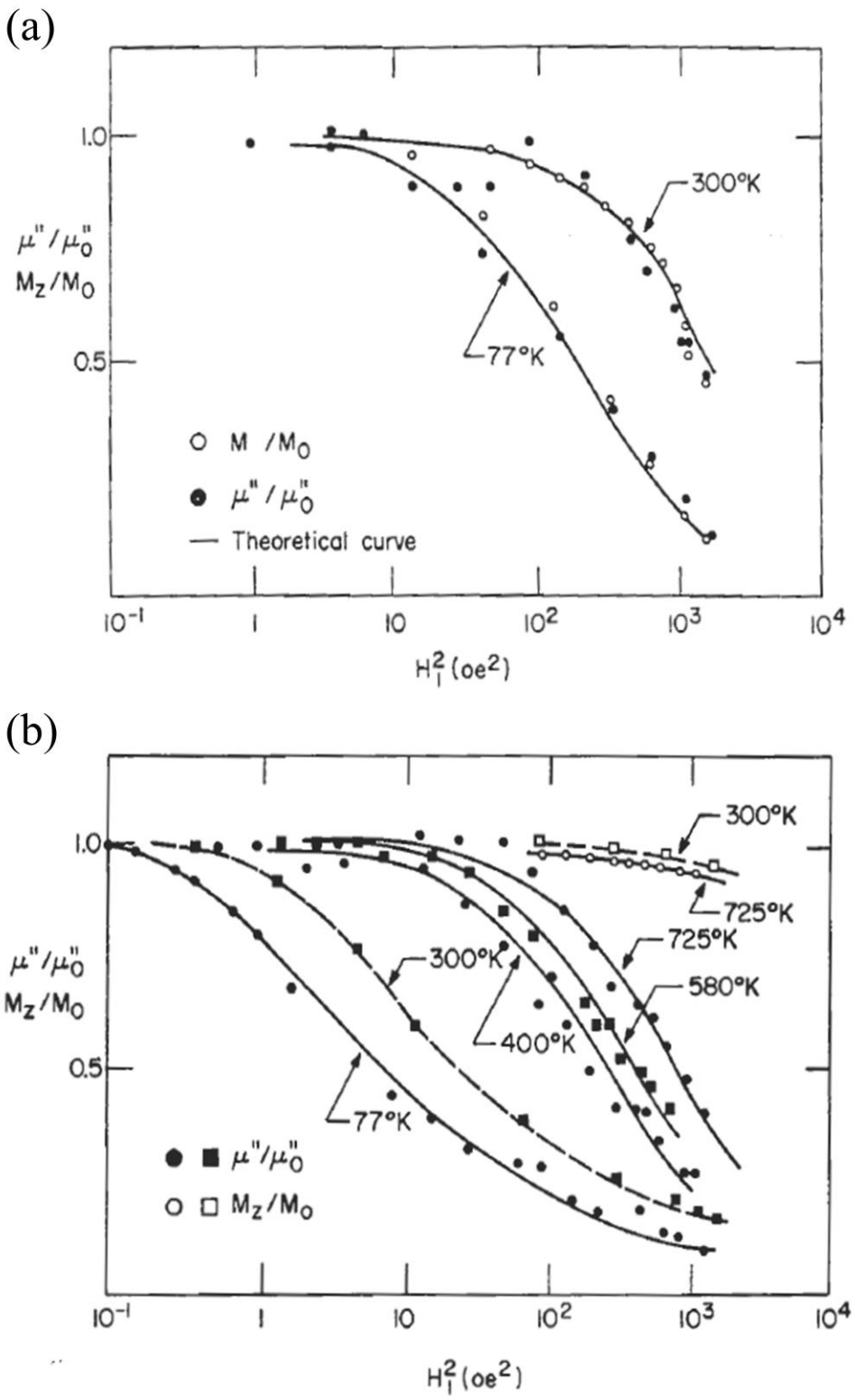

Fig. 1.7. (a) The variation of permeability (imaginary part) and magnetization ratio with the microwave field strength, H1, at resonance for paramagnet $MnSO_4.4H_2O$ at two different temperatures. (b) Similar curves for Nickel ferrite crystals.(Source: [20].)

As shown in Fig. 1.7, while a good agreement was found for paramagnetic materials (Fig. 1.7(a)), it was not the case for ferromagnetic materials (Fig. 1.7(b)). It is found that while the ratios μ''/μ_0'' and M_z/M_{z0} decrease with increasing microwave power; they do not coincide for the case of ferrimagnets as expected from the theory. Also, the absorption saturates at powers much lower than that needed to produce an appreciable change in M_z.

Finally, an unexpected broad absorption maxima was also observed in the experiments at lower fields. These abnormalities were later explained by the theories developed by Suhl and Anderson [54], [77]-[79]. An explanation of the disparity as developed by Suhl would be given in Chapter. 3, before leading to the application of the theory to FSL devices. These early studies lead to subsequent discoveries of numerous other physical phenomena; understanding these phenomena is vital not just from a physics perspective but also from the perspective of engineering applications.

1.8 Extreme Nonlinearity: Magnetic Recording, An Application

Most discussions up to now were based on *perturbations* induced in saturated magnets using microwave excitation. It was found that a high-power microwave can lead to nonlinear effects. At the extreme end of nonlinearity is *switching*, wherein the magnetization of the magnetic medium reverses. Deterministic switching of magnetization forms the basis of information storage using hard disk drives (HDDs).

The data storage needs of the world continue to increase, with the pace pushed even higher recently thanks to the growth of cloud-based services. The total stored data of the

world is expected to be ~160 ZB by 2025 [80]. In order to efficiently meet the ever-increasing data storage needs, the data density of the HDDs must increase. Numerous state-

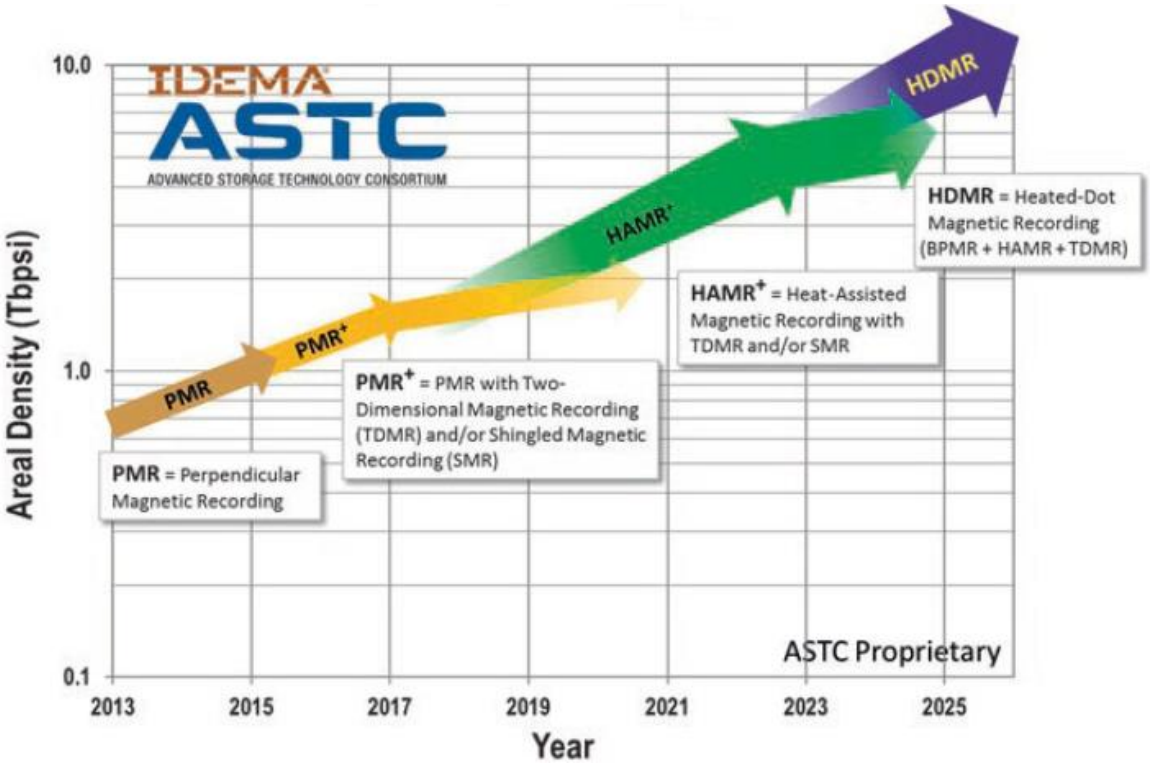

Fig. 1.8. Technology roadmap for HDD industry issued by Adavnced Storage Technology Consortium (ASTC). (Source: [80])

of-the-art magnetic recording technologies are being explored as suggested by the ASTC [80], as shown in Fig. 1.8.

Attempts to increase the data density with good data stability and signal-to-noise ratio (SNR**),** however, lead to a trilemma (Fig. 1.9). A *bit* can be defined as a collection of magnetic grains that defines a 0 or 1, also called a magnetic domain. It can be thought of as the smallest unit of information. As SNR is proportional to the number of grains, the need for a sufficiently high SNR would imply a large number of grains per bit. In order to

increase the data density while maintaining a high SNR would imply that the size of the grains be reduced so that more bits can be packed per unit area. However, a reduction in the size of grains makes them susceptible to switching under thermal fluctuations. In order to prevent the resulting noise, a high anisotropy media can be chosen that is more resistant to such thermal fluctuations. The problem now is that the high anisotropy media would need extremely high magnetic fields to switch the domains.

A. Heat Assisted Magnetic Recording (HAMR)

In order to address the trilemma, a heat pulse, for example, from a laser, can be employed to locally heat the magnetic media momentarily reducing its anisotropy [81]. This would allow the use of a smaller magnetic field to write the bits while enabling high data-densities (> 3 Tbpsi (Terabits per square inch)). This novel technology is called heat

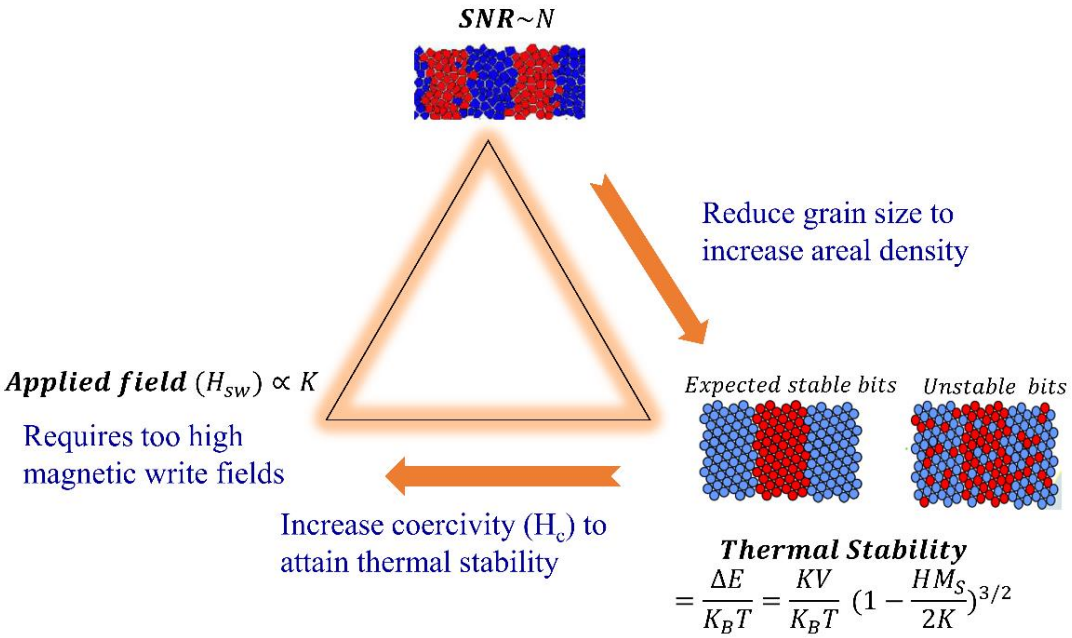

Fig. 1.9. Design Trilemma captures the challenges faced as the areal density of hard disks is increased.

assisted magnetic recording (HAMR) [82], [83]. Fig. 1.10 illustrates the principle of HAMR, schematically.

Understanding heat flow through the various layers of the media would be crucial for designing robust HAMR-based media. One of the major problems is the adjacent track erasure (ATE) wherein bits on the tracks adjacent to the track being written can be unintentionally erased due to the diffusion of the heat away from the heat spot.

In this thesis, I present a realistic calculation of heat flow by first employing a finite difference time domain (FDTD)-based optical calculation to determine the optical power input the media (code due to A. Ghoreyshi [84]). The optical power from FDTD is then used in a heat equation solver (self-developed code) to determine the realistic temperature profiles for recording-media design.

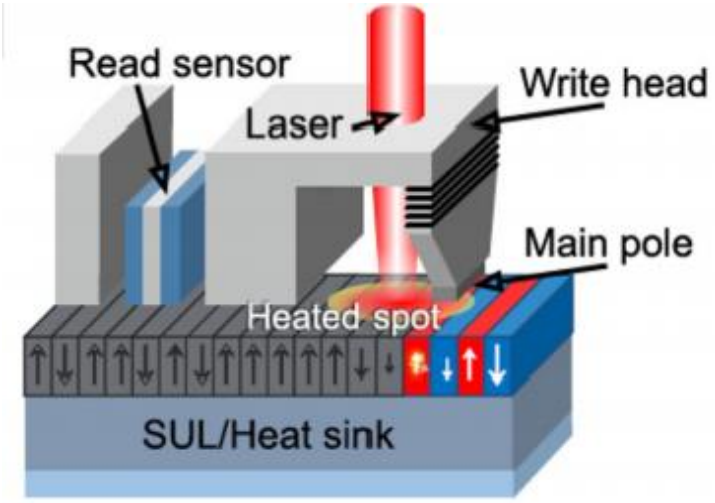

Fig. 1.10. Heat Assisted Magnetic Recording (HAMR) uses laser to enable easier writing of the magnetic media. The magnetic material is heated to reduce its coercivity. (Source: [82])

B. Bit Patterned Media Recording (BPMR)

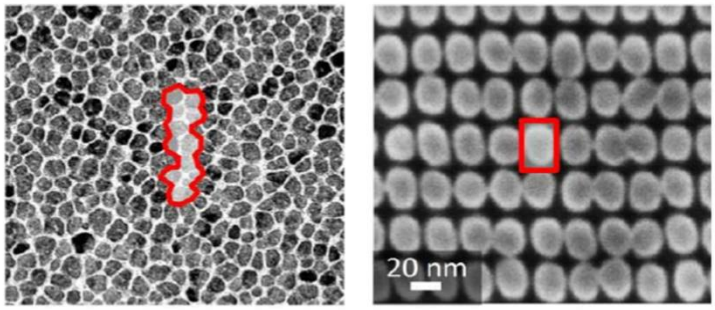

Fig. 1.11. (a) Traditional granular media records individual bits as a collection of grains. (b) BPM records bits in the form of magnetic islands or dots. (Source: [85])

Traditional magnetic recording media consists of a thin-film of magnetic recording layer, which comprises single-domain grains. The grains, however, are neither arranged in a regular pattern nor are they of the same size owing to the variabilities in the manufacturing process. The recording process deals with the randomness in the grain size and grain growth pattern by defining a bit to be a collection of such grains so that properties

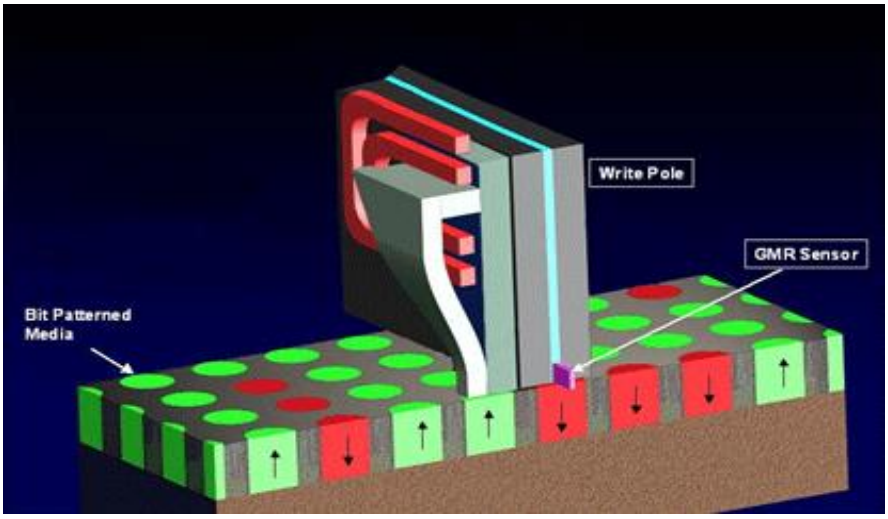

Fig. 1.12. BPM Schematic. Bits are recorded on magnetic islands. A write pole is used to switch the magnetic dot and reading is performed by a sensor. (Source: [92])

are averaged over a number of grains. An improvement would be to use a single but relatively bulkier grain (sometimes called a dot) to define a bit. This is called bit patterned media recording (BPMR) [85]-[88]. Fig. 1.11 compares traditional granular and BPM and Fig. 1.12 shows BPMR schematically. Since the bit edge is defined by the physical edge of the dot, BPM leads to lower jitters (a type of noise based on the location of the bit). BPM can resolve the ATE problems associated with HAMR recording to some extent by using a matrix with a low-conductivity heat material, which can help to reduce heat diffusion to the adjacent tracks [86].

Exchange coupled media (ECC) uses two layers of magnetic material for recording [86], [89]-[91]. A magnetically soft layer helps to switch the magnetically hard layer which stores the data. Such an arrangement helps to reduce the writing field. The efficiency of such a scheme goes down due to the exchange coupling amongst the grains and also due to the grain size distribution, both of which are unavoidable in traditional media. BPM is ideal for exchange-coupled media since it can provide magnetic isolation between the dots.

Together, HAMR and BPMR constitute the heated dot magnetic recording (HDMR). Although the nonlinear magnetic processes play an important role in HDMR, the nature of this nonlinearity is very different from that involved in resonance studies, where the nonlinearities were largely perturbative. In other words, while the material remains saturated in resonance studies, it is forced to switch in recording applications. Such higher degrees of nonlinearities are very difficult to be studied theoretically, and most

studies are often simulation-based. In Chapter 8, I explore the simulation-based design of HDMR for high-density data recording.

1.8 Challenges and Research Outline

Much of the potential of magnons, either as exploratory tools in uncovering fundamental physics or as additional degrees of freedom in engineering applications, remain under-utilized. The bottleneck, as mentioned earlier, is often the lack of understanding of the nonlinear scattering mechanisms involving magnons and their dynamics. For example, the miniaturization of devices like magnetics-based FSLs needs a deeper understanding of magnon scattering phenomena and their dependence on material parameters. From a fundamental physics perspective, the dynamics of the interaction between magnons and cavity photons is still not well understood; these are important for cavity-based quantum information research. These are just two of the myriads of active problems in the research field. I intend to develop a deeper understanding of the nonlinear magnon scattering processes both by developing analytical formulations and by constructing computational tools that provide qualitative and quantitative modeling capabilities. The projects described in this thesis make use of the two theoretical approaches to varying degrees.

The immense computational resource requirement has stymied micromagnetic investigations of microwave-magnet interactions in the past. In micromagnetics, the magnetic system is divided into multiple cells. The LLG is then solved for each cell of the

system under the influence of short-range (e.g., exchange) and long-range (e.g., dipolar or demagnetization) magnetic fields. The wavelengths of spin waves are of the order of 100s of nm, while the spatial dimensions of devices exceed 100s of micrometers. To accurately capture the behavior of the magnetic system, cell dimensions should be lower than the dominant magnon wavelength. This leads to a large number of cells, increasing the computational complexity. Moreover, while the time-step of simulations is restricted to a few 100s of fs (due to solver stability issues), the total simulation time required could be as high as a few microseconds to enable steady-state studies. This often leads to a large number of time steps leading to extremely long code runtimes. For example, many of the simulations in the current work require about 5 μs of simulation time, at a time step of 500 fs, needing about 10 million time-steps. Such a system when employed with 16384 cells needs a runtime of about 3-5 days on a CPU-only machine. A usual project would need hundreds of such simulations, thereby making traditional sequential studies unreasonable. Computational paradigms based on graphics processing units (GPUs) and a parallel language (e.g., CUDA) can offer tremendous benefits to micromagnetics. It is primarily the inherent nature of the physical parameters being computed using micromagnetics that allows for such parallelizations. More details will be described in Chapter 2. Micromagnetic simulations are performed using GPUs (NVIDIA K40, K80, P100, V100, etc.) at various supercomputers. Local workstations used consumer-grade GPUs like GTX 980, 1080, and P5000. MATLAB-based tools have also been developed to help analyze data from the solver.

Using the propagation direction of spin waves, I have also implemented an additional layer of optimization to specifically enable parallel-pump-based micromagnetics studies. This has allowed vital physical phenomena to be captured using a resource-conserving 2D simulation system instead of a full-fledged 3D system. For example, this has provided the ability to successfully capture nonlinear phenomena like the three- and four-magnon scattering using the simulation system. These processes govern the nonlinear characteristics of materials used in devices like FSLs. The simulations also allowed accurate predictions of the threshold microwave field, h_{th}. The threshold microwave field is the minimum field that triggers the onset of nonlinearity. The quantitative knowledge of the threshold-field is vital for designing various crucial characteristics, e.g., in the case of FSLs – the bandwidth of operation, frequency selectivity, etc. Further details will be discussed in detail in Chapter 2, 3, and 4.

An important issue addressed in this thesis is the dynamic control of the threshold field. Threshold field (h_{th}) plays an important role in the physics of instability processes. However, the ability to vary the h_{th} dynamically is not well understood. In Chapter 5, I provide a comprehensive explanation of the considerations involved in dynamically altering the threshold field using a subsidiary signal. This technique is highly desirable as the secondary microwave frequency needs only be a few MHz in order to enable sufficient dynamic control. The dependence of this phenomenon on the damping factor of the magnetic material and secondary field intensity is also studied.

Another important quantity studied is the phase-noise. The phase of the magnons plays a key role in magnon-magnon interactions. Due to its direct involvement in nonlinear

properties, the phase is also significant from a practical viewpoint, more so as the magnon-based devices become increasingly miniaturized. In fact, numerous applications that rely *directly* on the magnon phase have been proposed in the recent past. The operations of *novel applications* like magnon transistors, spin-wave lens, and logic circuits strongly depend on the phase of the dominant magnons. In other devices, the magnon-phase indirectly controls essential phenomena that determine the device functionality. Magnon-based devices such as FSLs, Signal to Noise ratio Enhancers (SNEs), etc., used in *conventional applications* like - telecommunication, rely on magnon-phase governed interaction phenomena to reduce unwanted microwave frequencies. Despite the importance of the magnon phase, the physical effects of magnon phase-noise remain relatively unexplored in the larger context of magnon-based magnetics. Studies of noise in the past are largely based on thermal noise, where phase noise is often considered only in terms of macro-spin models or as a by-product of thermal noise in the context of specific applications, e.g., spin torque oscillators (STO). A direct study of the phase-noise is, hence, timely. In Chapter 6, I present a more general and fundamental treatment of the consequences of phase noise, which is applicable across multiple magnon-based nonlinear applications.

In Chapter 7, I discuss the secondary interactions amongst the parametrically excited magnons. Above the threshold field, the number of magnons is so high that we can no longer assume that the excited magnons are non-interacting. These secondary interactions can lead to interesting phenomena like microwave-based hysteresis effects. A discussion of such phenomena and the underlying analytical considerations are presented.

Finally, in Chapter 8, I present some of the design considerations in Shingled BPMR for data storage applications. The study involves highly nonlinear processes that result in switching the magnetic grain (of FePt) during the process of data recording. The theoretical limits of data-density possible using BPMR are explored under noise considerations like jitter and track misregistration.

Chapter 2 Parallel Program-based Micromagnetics Solver and Data-Analysis Tools

Computational research has earned its pedestal when it comes to scientific research and is now seen as the third leg of exploration in addition to traditional analytical and experimental research [93]. This is true for magnetics research, wherein ground-breaking physical phenomena have been discovered and/or studied using simulations [5], [94]-[97]. The use of a high-speed computational tool has become indispensable for exploring microwave-induced magnon physics due to the complexity of the processes involved. Simulations are made even more important due to the fact that even state-of-the-art experimental techniques fall short when it comes to probing/studying certain aspects, e.g., the ability to track individual magnon modes, high-resolution studies of magnon scattering processes such as confluence and splitting, etc. The lack of such capabilities in the past has prevented crucial research into magnonic phenomena, including nonlinear processes.

In this chapter, I describe the construction of the high-speed micromagnetics solver used for simulation-based studies discussed in this thesis. The solver is realized using parallel programming and helps to address the computational limitations of the past [107]. Special attention is paid to code optimization details, especially regarding the parallel code for the GPU. The techniques used by some of the important tools that I developed to analyze the solver data are also described. The solver and tools have helped us uncover important aspects of magnon behavior that are presented later in the thesis. The micromagnetics solver is ~100x faster than sequential micromagnetics tools and ~1.5 to 2 times faster and more accurate than certain other GPU-based implementations. Together

with the GPUs and other computational resources at various supercomputers, these tools have made possible studies that would have been otherwise very unreasonable timewise.

2. 1 Landau Lifshitz Gilbert Equation

The Landau Lifshitz Gilbert (LLG) equation governs the magnetization dynamics and therefore is the fundamental equation for simulation-based studies:

$$\frac{dM}{dt} = -\frac{\gamma}{1+\alpha^2}\left[M \times H - \frac{\alpha}{|M_S|} \times M(M \times H)\right] \tag{2.1}$$

α, γ and M_S represent the three constants involved in the LLG. α, represents the dimensionless Gilbert damping constant; γ is the gyromagnetic ratio with a magnitude $1.76 \times 10^7 \frac{rad}{sOe}$; M_S is the saturation magnetization of the magnetic system. The two terms of physical importance that are evaluated during the process of solving the LLG are the magnetization, *M*, and the effective magnetic field, *H*. The first term within the brackets in Eq. (2.1) determines the precession of *M*, while the second controls its damping, i.e., the rate at which energy is lost. Together the two determine the dynamics of *M*, under the influence of *H*. Perhaps not directly evident from the above form is the nonlinear nature of the LLG - a torque equation.

Furthermore, thermal fluctuations due to the ambient temperature can lead to an effective magnetic field that contributes to *H*. The presence of a noise-term inside *H* makes LLG a *Fokker-Planck equation* (a stochastic equation). LL and/or LLG is, hence, often a suitable tool to study a wide variety of mathematical aspects, e.g., stochastic properties and behavior [98], [99], chaos [41], solitons [100], etc. to name a few. The mathematical richness of LLG perhaps is suggestive of the plethora of physical phenomena exhibited by

magnetic materials, which in turn make comprehensive analytical studies of such materials very challenging.

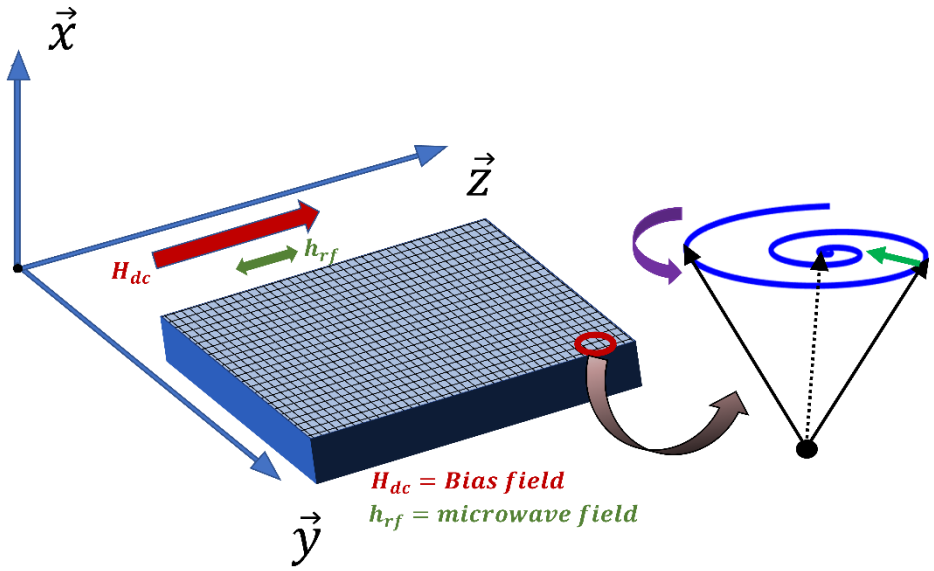

Fig. 2.1 Micromagnetics involves dividing the magnetic system to be studied into multiple cells. To each cell a magnetization is assigned, the evolution of which is then determined under the influence of the net magnetic field experienced by the cell.

2.2 Micromagnetics Solver Implementation

The technique of micromagnetics involves the discretization of the magnetic system into multiple cells. To each cell, I assign a magnetization, as shown in Fig. 2.1. This is in contrast to the macroscale approach in which the magnetization of a device or a sample is assumed to be uniform. The whole of the magnetic sample is consequently treated in a macroscopic treatment by a single magnetization. While the macroscopic treatments can be very useful for certain applications, they miss out on the details of the processes at smaller spatial scales. In other words, processes that involve non-uniform magnetization across the sample cannot be studied properly using macroscale approaches. In

micromagnetics, discretization is often determined by the process under investigation. The possibility of higher resolution makes micromagnetics highly suitable for studying phenomena involving domain walls, vortices, skyrmions, magnons, etc. It must also be pointed out that micromagnetics while providing higher resolution when compared with macroscopic approaches, is still a classical/semiclassical approach and does not capture true quantum phenomena. Quantum mechanical calculations, e.g., electronic structure calculations, need to be employed in order to study quantum phenomena.

From a computational point of view, we can associate with each cell of the micromagnetic system a set of static and dynamic properties. The main dynamic properties of each cell that need to be evaluated are the 3 components (one for each Cartesian direction) of:- the magnetization and the various magnetic fields. Since the net magnitude of the *M* in the LLG is not allowed to vary (Chapter 1, Section 1.3), the degrees-of-freedom are the polar (θ) and azimuth (ϕ) angles such that: $M_z = M_S \cos\theta, M_y = M_S \sin\theta \sin\phi$ and $M_x = M_S \sin\theta \cos\phi$. In this work, we consider the following magnetic-field intensities that together comprise the effective intensity *H*: exchange field h_{ex}, demagnetization field h_d, thermal field h_t, externally applied fields: H_{dc} (magnetic bias-field), and h_{rf} (microwave-field).

A. Parallelisms in magnetic system

The magnetic system, from a computational perspective, is a highly parallel system. We can identify two levels of parallelisms, which can be exploited to design a high-speed parallel micromagnetic solver.

(a) Intracellular parallelism: Various attributes of a cell, e.g., the magnetic fields, can be computed independently of each other.

(b) Intercellular parallelism: Most attributes of a cell are independent of the other cells of the system. For example, except for the exchange and demagnetization fields (which exhibit short and long-range dependence, respectively), the other fields can be computed independently of other cells.

The parallelisms inherent in the magnetic system can be leveraged to provide independent tasks to a suitable parallel computational device, e.g., the graphics processing units - that have been optimized both at the hardware and software levels to perform parallel tasks. Such accelerators can help in achieving enormous computational speeds when compared with traditional CPU (central processing unit)-only solvers. The subsequent sections will provide more details on the use of graphics processing units pertinent to micromagnetic simulations.

B. Graphics Processing Units (GPUs)

GPUs have played a pivotal role in the simulations studies described in this thesis.

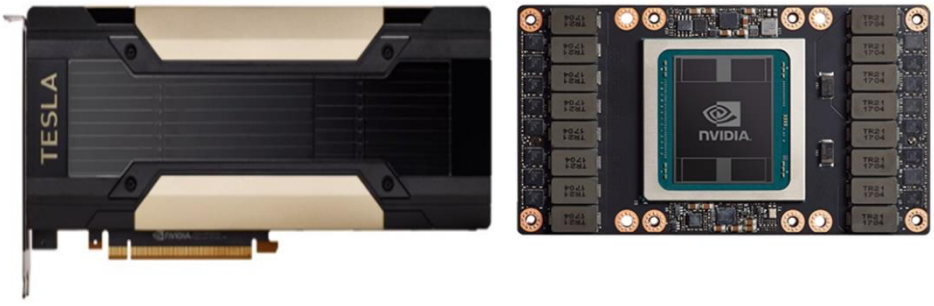

Fig. 2.2. Graphics processing unit (NVIDIA V100). (Source: [102])

GPUs are high-throughput devices that were originally developed for gaming and image processing applications that need identical computations to be performed on large data sets. The idea is to employ a large number of processors, each of which, although slower than traditional CPU cores, can lead to increased throughput. The ability of GPUs to process large blocks of data in parallel makes them more efficient than general-purpose central processing units (CPUs) in performing large parallelizable tasks [101]. The applicability of GPUs to scientific computations that involved a large number of parallel tasks was soon realized.

The inherent computational parallelizability of the magnetic system makes GPUs highly suitable for accelerating micromagnetic simulations, especially in investigations that involve a large system-size to cell-size ratio and/or simulation-time to timestep ratio. The GPUs have a large number of compute-cores compared to CPUs, as shown in Fig. 2.3; even though each compute-core of the GPU may be slower than that of the CPUs, the sheer number of GPU cores can provide unprecedented speed-up for data-intensive parallel applications. It is to be noted that if the amount of data to be processed (or the number of parallel tasks) falls below a certain threshold, the use of GPUs can be highly inefficient.

In our micromagnetics solver, a GPU is employed alongside the host CPU, forming a heterogeneous computing environment. It is the CPU, also referred to as the host, that performs the tasks in succession, assigning the parallel tasks to the GPU (also referred to as the device). Such a paradigm aims to make the best possible use of the two computational devices. As indicated earlier, microwave-magnon interaction effects (e.g.,

ferromagnetic resonance) can be qualitatively and quantitatively well studied using such a computational paradigm. It is also suitable for magnetic recording [103] and other magnetic-storage device simulations [104].

C. Computational Process Flow

We use RK4 numerical integration for our LLG computations. (Previous studies have shown the predictor-corrector methods to be inaccurate in the presence of thermal

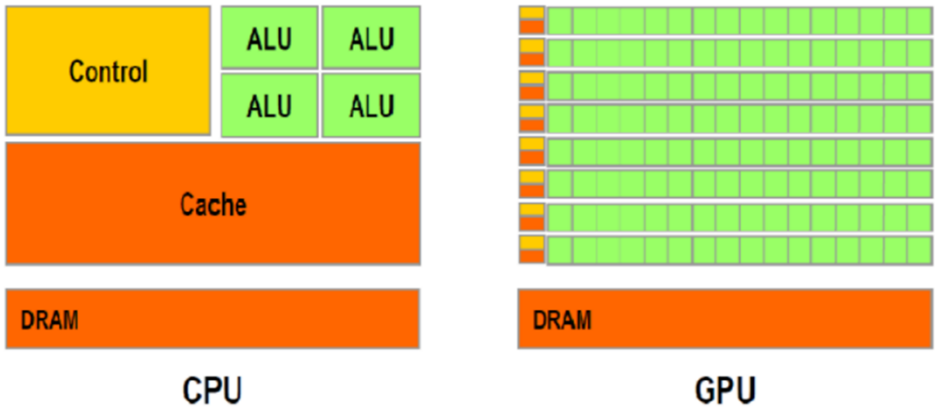

Fig. 2.3. CPU vs GPU; GPU has more ALU compared with CPU with relatively low cache memory. GPU is as such optimized for high throughput calculations. (Source: [101])

fields [105, 106].) $N_Z, N_Y,$ and N_X represent the number of cells along the z-, y- and x-Cartesian directions, respectively, such that $N = N_Z N_Y N_X$, with N representing the total number of cells. For performing the simulations, first the boundary and initial conditions are established. In this work, I have used periodic boundary conditions. The initial magnetizations are usually assumed to be random. (Provisions are also made to start the simulation from uniform or random magnetization or from a configuration that can be loaded externally from a file. Other boundary conditions can also be easily included.)

A brief description of the computational process is shown in Fig.2.4. At first, all the necessary constants, initial conditions, and the demagnetization kernel (in the case of dipolar fields) are loaded into the device (GPU) memory. The host primarily controls the process flow and, therefore, maintains the iteration count and initiates the tasks that are to be performed by the GPU. After a task that is assigned to the GPU is accomplished, the control is returned to the CPU, which then initiates the next task. Various magnetic field intensities (discussed in Section 2.3) are computed by the GPU for the given timestep. The

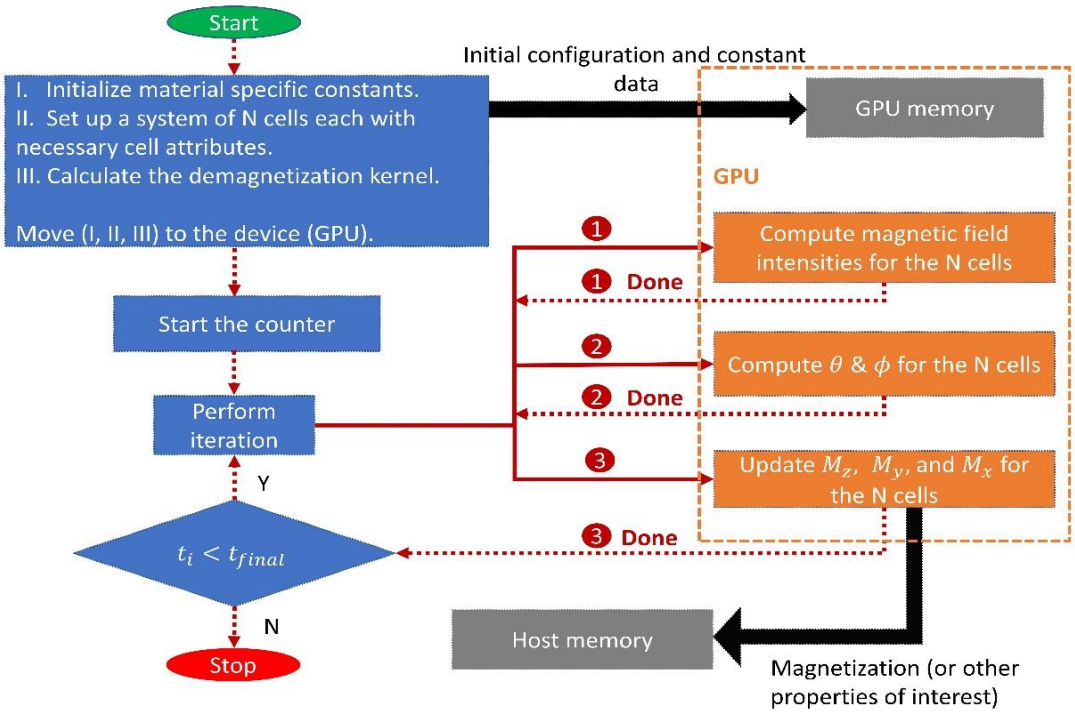

Fig. 2.4. CPU-GPU-based process flow in a heterogeneous environment for micromagnetic calculations described in the thesis. The dashed box represents the GPU wherein the various computations are performed in parallel for increased throughput. Outside of the box represents the host (CPU) environment. Source: [107]

angles θ and ϕ are then determined and used to calculate the magnetizations at each of the cells. The magnetization and/or other useful data at the given timestep can then be transferred back asynchronously to the host memory if needed. The host then proceeds to

initiate the next iteration, and this process is continued till an end condition is met (e.g., a preset simulation time). In the following sections, we describe in detail the calculations of the various field intensities.

D. Data Arrangement in the GPU global memory

For efficient data access to/from the GPU global memory [Dynamic Random Access Memory (DRAM)], *coalesced access* is ensured through the proper arrangement of data. This is crucial as improper data arrangement can reduce the speed of execution. When the GPU accesses data from its DRAM, it does so in such a way that the data placed in nearby locations are accessed together and returned on the data-bus. This process is called the *bursting* of the data [101]. In bursting, it would be to our advantage if all (or most of) the data returned is relevant.

Irrespective of the dimensionality of the system being simulated (3D, 2D or 1D), as far as any attribute is concerned (e.g., M_X), its data arrangement in memory is sequential. While implementing parallel code, the cells of, say, a 3D system are accessed as per user-defined serial indices. In case the data is not arranged correctly, nearby cells may have their data scattered far apart in the memory. If so, the GPU would have to reach into the DRAM multiple times to retrieve the data it needs to complete a step, i.e., multiple burstings. By ensuring the proper arrangement of data, we can ensure coalesced data access and maximize the speed of execution. In my implementation, separate channels (or arrays) are used for each attribute. The arrangement of various dynamic attributes in properly laid out

separate channels helps to make efficient use of the data-bursts in the GPU memory.

Shared- and *private memories* that have faster access (compared to DRAM) are also employed appropriately to reduce the access times. However, these memories have significantly smaller capacities, thereby limiting their use.

2.3 Magnetic Field Intensity Determination

In this section, I describe the determination of the magnetic field intensities that are fundamental to the LLG equation. The computations were carried out on NVIDIA GTX-980 GPU card and Intel Xeon (R) ES-2630 CPU in a Linux environment. For each field, I briefly describe the physics and its significance before moving on to the mathematical and implementation details. Essential code optimization techniques are then provided.

A. Thermal Field

At first, I discuss the computation of the effective magnetic field arising from thermal fluctuations in the magnetic system. This field arises due to the non-zero temperature of the magnetic sample (usually the ambient room temperature). The effective magnetic noise is responsible for the instabilities in the recording media used in magnetic storage. Thermal field leads to random switching of grains that ultimately results in bit corruption given sufficient time. The field also plays an important role in microwave-magnon interactions. Thermally generated magnons can increase the noise in a magnonic system. Furthermore, they help to create the initial magnons, which can then be pumped by the microwave to very large numbers. They can also scatter with the parametrically

excited magnons (from microwave pumping) to give rise to interesting phenomena.

Since the random thermal field contribution to the field intensity multiples the magnetization, it makes LLG a Fokker-Planck equation of the multiplicative kind. The computational realization relies on the use of a random number generator. Following

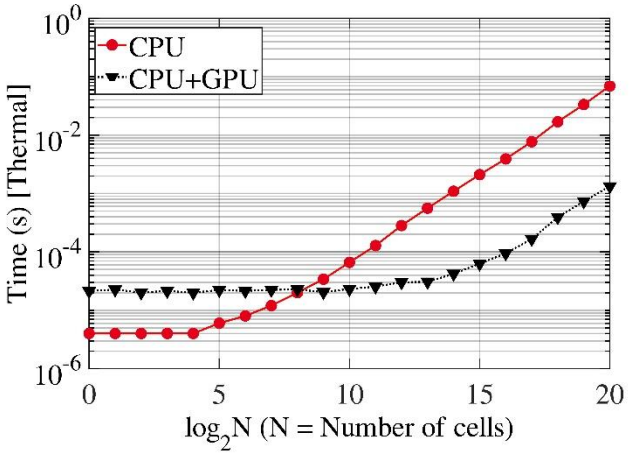

Fig. 2.5. Comparison of iteration time for thermal field computation using sequential (CPU) and heterogeneous (CPU+GPU) approach. An average of 5000 iterations is taken to compute the time. (Source: [107])

Brown [108], the noise is assumed to have zero mean $< h_t >= 0$; also, at two different cells located at r and r' for distinct times t and t', $< h_t(r,t) >$ and $< h_t(r',t') >$, a correlation exists only for time intervals much shorter than the time required for an appreciable change in *M*. (Angular brackets denote statistical average.) Accordingly, we have δ-correlations in space and time:

$$< h_t(r,t)h_t(r',t') > = \frac{2K_B T\alpha}{M_S\gamma'\tau\vartheta}\delta(t'-t)\delta(r'-r) \tag{2.2}$$

Where Boltzmann constant $K_B = 1.38 \times 10^{-16}\frac{erg}{K}$, T is the temperature, $\gamma' = \frac{\gamma}{1+\alpha^2}$. τ is

the timestep used in the simulation and ϑ is the unit-cell volume.

The δ-correlations have special significance in a parallel computational environment as they allow for maximum parallelizations by eliminating dependency from other cells. Fig. 2.5 compares the time taken in a sequential CPU paradigm (no GPU is used) to that in a heterogeneous (CPU+GPU) paradigm for a single iteration of thermal field computation as the number of cells in the system is varied. It can be noted that for small cell numbers (in our studies for $N < 2^8$), the CPU performs faster. This is due to the insufficient amount of parallel tasks available. Even though all tasks are parallel, there are

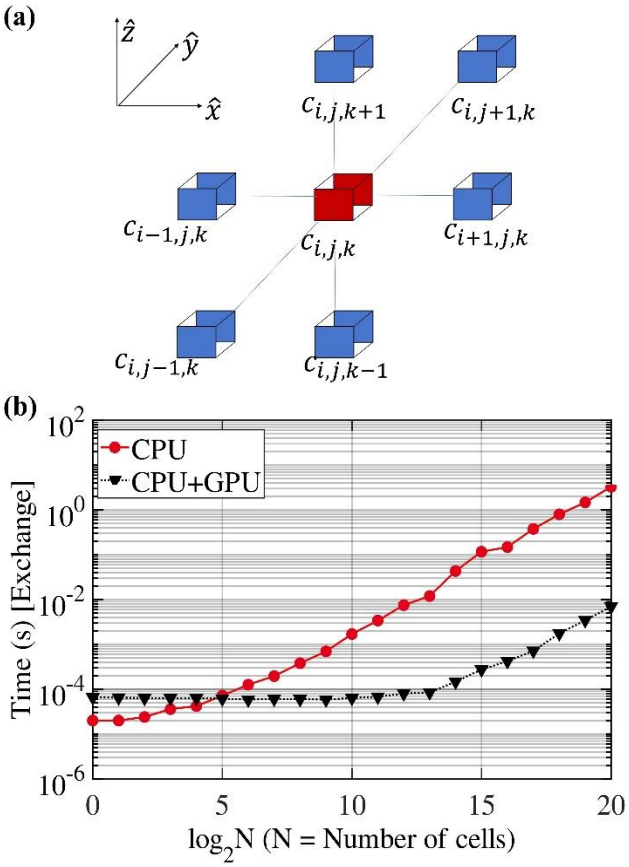

Fig. 2.6. (a) 7-point stencil showing the nearest neighbors used in the exchange field intensity computations for a cell $c_{i,j,k}$, in 3D identified by the Cartesian indices i, j, k. (b) Comparison of iteration time for exchange field computation using sequential (CPU) and heterogeneous (CPU+GPU) approach. An average of 5000 iterations is taken to compute the time. (Source: [107])

not enough tasks to keep all the GPU-cores busy at a given time, leading to some of the GPU-cores remaining idle. There is always an overhead associated with using GPUs (e.g., the overhead of launching various GPU kernels, CPU-GPU communication, etc.) [101]. For data-intensive simulations (i.e., a large number of parallel tasks), this is offset by the high throughput, so we get an overall speed-up, but for low amounts of data, the overhead exceeds any gain in speed-up.

As the number of cells increases, however, a GPU-based system can be orders of magnitude faster than a CPU-only system as demonstrated in $N > 2^8$ in Fig. 2.5.

B. Exchange Field

The exchange interaction arises due to the quantum-mechanical nature of electrons, requiring the electron wave functions to be anti-symmetric. Since the electrons at the adjacent site have the maximum probability of exchange, this field is strongest between the nearest neighbors. Exchange is a quantum phenomenon and attributes the semiclassical nature to LLG. In general, it is the dominant field at short ranges. In this context, materials are characterized by their exchange constant, A_{ex}. Due to the short-ranged influence, the exchange field results in exchange-magnons that have smaller wavelengths (or large wave-vectors). These are important from the perspective of miniaturization of the magnonic devices. In simple terms, the exchange energy is such that $E_{ex} = Dk^2$, where ($D = \frac{2\gamma A_{ex}}{M_s}$) is an exchange parameter, and *k* is the wave-vector of the spin-wave. This is important as it is the exchange interactions that lead to the parabolic energy dependence of spin-waves

w.r.t. their wave-vectors. A more detailed description of the exchange phenomenon can be found in [109, 110]. The exchange field can be written as [109]:

$$h_{ex} = \frac{2A_{ex}}{M_S^2}\left[\nabla^2 M_z \hat{z} + \nabla^2 M_y \hat{y} + \nabla^2 M_x \hat{x}\right] \tag{2.3}$$

and is obtained by taking the derivative w.r.t the magnetization, of the exchange energy density:

$$E_{ex} = \frac{A_{ex}}{M_S^2}\left[|\nabla M_z|^2 + \left|\nabla M_y\right|^2 + |\nabla M_x|^2\right] \tag{2.4}$$

where, ∇ is the gradient operator.

In this implementation, I consider only the nearest-neighbor interactions. Eq. (2.3) amounts to a 7-point stencil computation for each cell (Fig. 2.6(a)) in a 3D system. Due to the dependence on other cells, the parallelization is reduced when compared with, say, the thermal field. However, data reuse using shared, and private memory reduces the number of data fetches needed from GPU DRAM, resulting in an overall speed improvement. Fig. 2.6(b) shows the time taken as we vary the cell numbers. As in the case of thermal field computation, we can observe that the CPU gets significantly slower as the number of cells increases. The use of private variables has been observed to increase speed-up, although it must be pointed out the number of private variables allowed is determined by the number of cells and the GPU.

C. Dipolar field

Dipolar and demagnetization fields arise on account of the magnetic dipole-dipole interactions in the material. Due to their long-range nature, dipolar interactions are the most

difficult to compute, as computation for a given cell must take into account all the other cells present in the system. The significance of demagnetization fields in resonance experiments was first explained by Kittel [111]. He pointed out that the resonance frequencies can be affected by the sample shape and geometry. Uniform precession of the magnetic-moments in a material (the so-called uniform mode in terms of magnons) is a natural mode only to the first order in the presence of dipolar fields. The addition of the dipolar field couples various magnon modes. Demagnetization interactions lead to magnons of larger wavelengths. These interactions play an important role in many applications, e.g., RF devices [112], cavity experiments [9], [113], etc. In my implementation, I make use of the magnetostatic assumption. Due to the small size of the magnetic sample, propagation effects can be ignored. The effects of dipolar fields are felt across the sample instantly. In contrast, the exchange field effects propagate at a finite speed.

Mathematically, the demagnetization field intensity computation for a cell amounts to the evaluation of the convolution between the Green's function and the magnetization configuration of the material, e.g., for a general unit cell at the location, $r(z, y, x)$, the demagnetization field intensity experienced can be written as:

$$h_d(z, x, y) = \iiint \overleftrightarrow{G}(z - z', y - y', x - x')\, M(z, y, x) dz' dy' dx' \tag{2.5}$$

where, $\overleftrightarrow{G}$ is the Green's function of the system in real-space.

$$\overleftrightarrow{G} = \begin{bmatrix} G_{xx} & G_{xy} & G_{xz} \\ G_{yx} & G_{yy} & G_{yz} \\ G_{zx} & G_{zy} & G_{zz} \end{bmatrix} \tag{2.6}$$

Each entry determines how a field intensity along the direction indicated by the first subscript would affect magnetization along the second. Note that each entry has N components, one for each of the cells, leading to the requirement of 9N units of storage for $\overleftrightarrow{G}$. Since the determination of $\overleftrightarrow{G}$ depends on the geometry of the system, it can be computed deterministically at the start of the simulations, allowing it to be stored in a faster memory for repeated access later, e.g., the constant memory of GPUs (depending on the number of cells and the storage capacity of the GPU).

Direct determination of $\overleftrightarrow{G}$ in real-space coordinates leads to accuracy issues [106]. Hence, we use Fast Fourier Transform (FFT) techniques to determine $\overleftrightarrow{G}$ for simulations. This also helps in avoiding the complicated magnetostatic integrals involved in a direct computational scheme.

$$h_d(k_z, k_y, k_x) = \overleftrightarrow{G}(k_z, k_y, k_x).\, M(k_z, k_y, k_x) \tag{2.7}$$

Computation of the demagnetization effects for the case of a generalized cuboid cell has been considered by Newell *et al.* [114]. We use the demagnetization Green's functions developed therein for our numerical calculations. The implementation is highly efficient because the $\overleftrightarrow{G}$ needs to be computed just once, to be reused in all the following time-iterations.

Many of the investigations require periodic boundary conditions, especially those involving studies of the fundamental magnonic phenomena under the influence of microwave excitation(s). To enable periodic conditions, we repeat the magnetization configuration in all the Cartesian directions. This increases the number of cells used in demagnetization calculations to $N_d = 2N_Z.\, 2N_Y.\, 2N_X = 8N$ in 3D.

To summarize, there are 4 steps involved in the computation of demagnetization field intensity:

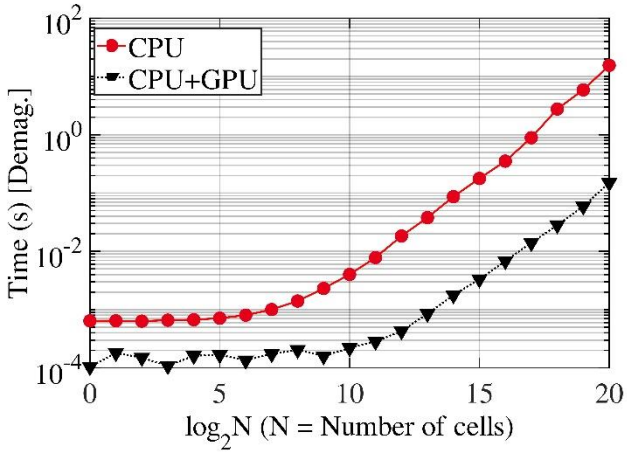

Fig. 2.7 Comparison of iteration time for demagnetization field intensity computation using sequential (CPU) and heterogeneous (CPU+GPU) approach. Data is averaged over 5000 iterations. (Source: [107])

(1) Compute $\vec{\vec{G}}(z, y, x)$ from which $\vec{\vec{G}}(k_z, k_y, k_x)$ is obtained.

(2) Compute FFT of the magnetization distribution.

(3) Evaluate $h_d(k) = \vec{\vec{G}}(\boldsymbol{k}).M(\boldsymbol{k})$

(4) Compute the inverse FFT to obtain $h_d(z, y, x)$.

Step 1 is performed in the host CPU system and moved to a suitable memory of the GPU device. While in the GPU, the CuFFT API (Application Programming Interface) is employed for the FFT computations involved in steps 2 and 4. Tiled matrix multiplications [101] are employed in step 3 to improve the computational speed. The computations may also be spread across multiple GPUs if need be. However, the ensuing GPU-to-GPU communication slows down the computations due to the associated communication overhead. Due to their long-ranged nature, the demagnetization field computations

consume the most computational resources and, consequently, are the least parallelizable of all fields. In Fig. 2.7, we can see the drastic reduction in speeds when compared with the thermal field intensity computations of Fig. 2.5. Interestingly, the overheads associated with the use of the respective FFT libraries (CuFFT for CUDA and FFTW for Fortran) and the matrix multiplication algorithms are such that heterogeneous computations are faster, even for small N.

D. Applied Microwave Field

A magnetic bias-field is often employed to saturate the magnetic material. Exciting the system with a microwave can then initiate spin waves in accordance with the resonance conditions. With respect to the microwave signal, I assume that the microwave field intensity is the same throughout the magnetic sample at any given instant. Often for state-of-the-art devices, where the goal is miniaturization, the assumption turns out to be reasonable. It is assumed that we have a perfectly linearly polarized microwave signal. It has been demonstrated in the past with experimental agreement that we can reasonably capture the nonlinear behavior brought about by the microwave signal in a magnetic sample, under the above-mentioned assumptions [112, 115].

In order to simulate the time-varying microwave field intensity, I use $h_{rf} = h_0 \cos(\omega_p t)$ along the appropriate direction (along z for parallel pumping and along y for perpendicular pumping in Fig. 2.1), with ω_p as the frequency of the microwave. This field needs to be added to each cell of the system at runtime due to the time-dependence of the

microwave signal. Nevertheless, the absence of dependency on other cells ensures high parallelization.

A comparison of the speed-ups obtained for various cell numbers under GPU acceleration is provided in Fig. 2.8. Overall, using a sequential code for small cell numbers gives higher throughput when compared with a parallel solver due to the overhead associated with the GPU usage. However, at large cell numbers, the use of GPU is more advantageous.

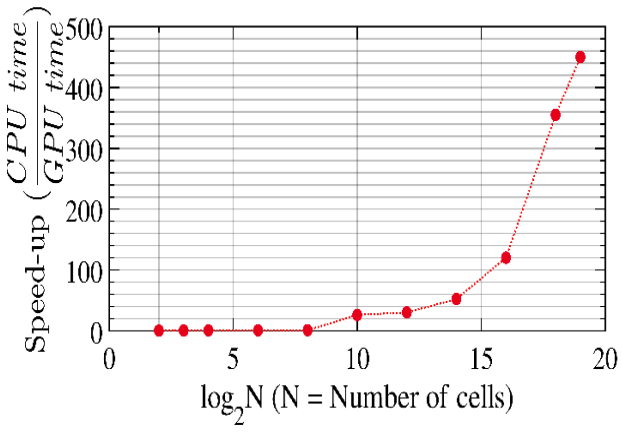

Fig. 2.8. Speed-up obtained by using a GPU accelerator for micromagnetics computations for varying cell numbers. (Source: [107])

As mentioned earlier, due to the large number of iterations involved, we use *double* (datatype) for our parallel solver. While this may preclude the use of the GPU functions optimized specially for the *float* (datatype) operations, it helps to improve the accuracy when a large number of iterations are involved (e.g., for simulations with long runtimes). For short simulations, the solver can, however, be easily converted to work with the float datatype in order to take advantage of the *float*-specific hardware/software optimizations in the GPU.

2.4 Data Analysis

The micromagnetic system can provide various dynamics attributes, e.g., the magnetization and magnetic fields at each cell location at each time-iteration. Important information from the perspective of fundamental physics and applications, e.g., dispersion relation, magnon dynamics, magnon phase, etc., can be obtained using this data. Below we describe the procedure for obtaining the dispersion relation and magnon dynamics using simulation data.

A. Dispersion relation

Dispersion relation can be understood to be a map of all the magnon modes that are allowed in the magnetic system. It is a plot of wave-vectors versus the energy of the magnons. Similar to the vital role played by the electronic bandstructure in the design and understanding of semiconductor-based devices, it is the magnon-dispersion relation that is crucial to understanding the magnetic response of the material in the realm of magnetics. However, unlike the electronic bandstructure of semiconductors, the magnon dispersion can be altered using parameters such as bias-field, sample-thickness, sample-geometry, etc.

In terms of applications, the magnon dispersion relation is indispensable in determining the external conditions that the magnetic sample should be subjected to in order to obtain the necessary functionalities [116]-[119]. For our study, we consider the thin film geometry as commonly desired in applications. By using micromagnetic

simulations, we are able to predict magnon processes and the radio-frequency (RF) response of YIG samples accurately due to our rigorous calculation of magnetostatic interactions and dispersion relations. Studies in the past [1], [120], [121] have typically relied on approximate calculations of dispersion and/or ignored the details of the magnetostatic interaction between magnons; such assumptions produce an inaccurate prediction of the vital magnon processes that control the behavior of the sample.

During simulations, the magnetization profile at regular time intervals (determined by the energy range of interest) is written out from the GPU to the host memory. In other words, a snapshot of the magnetization of the system is taken at specific time intervals, t_i, such that *i* represents a natural number. (Writing out data at specific time intervals instead

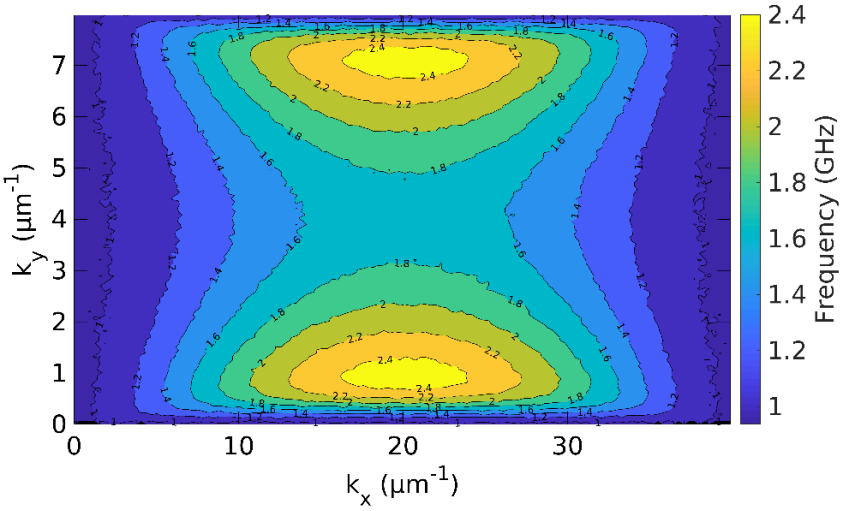

Fig. 2.9. Dispersion relations for a 5.1 μm thick YIG sample for a bias field of 100 Oe. (Source: [112])

of all reduces the data transfers between the host and the GPU, thereby helping to reduce the runtime; it also helps in lowering the storage- requirements.)

For calculating the dispersion relation, we begin with a randomized distribution of magnetization and allow the system to attain the steady-state under the applied magnetic

bias field. (No microwave excitation needs to be applied for the determination of dispersion relations.) The magnetization components M_y, and M_x are used to determine the dispersion relation. A 2D spatial Fourier transform of these components is taken at each t_i. Finally, a temporal Fourier transform (F.T) yields the dispersion relation. Mathematically, this can be represented as the following:

$$M(y,x;t) \xrightarrow{Spatial\ F.T} \mathcal{M}(k_y,k_x;t) \xrightarrow{Temporal\ F.T} \mathcal{D}(k_y,k_x;\omega_{\boldsymbol{k}}) \tag{2.7}$$

$\mathcal{D}(k_y,k_x;\omega_{\boldsymbol{k}})$ is the dispersion relation of the system, also referred to as the spin-wave manifold. k_y, and k_x are the wave-vectors along x and y, with $\boldsymbol{k} = (k_y, k_x)$.

Next, let us compute the dispersion relation of a magnetic film of YIG. The sample is 5.1 μm thick with lateral dimensions of 100 μm x 1250 μm. The sample is divided into 128 x 128 x 1 cells along the directions measuring 5.1 μm x 100 μm x 1250 μm respectively. Note the special geometry for simulation. (The simulations are carried out in a configuration that best captures the relevant physics for parallel pump configuration. A rigorous justification for using such a configuration will be provided in Chapter 4.) Other parameters used are: intrinsic magnetic damping constant α =0.0028, saturation

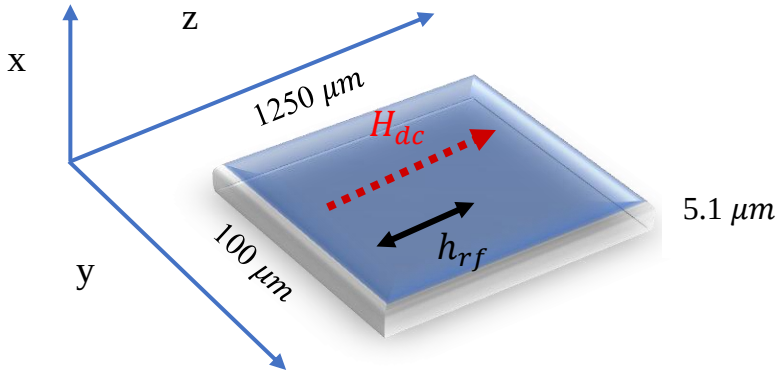

Fig. 2.10. The YIG sample with the field directions for parallel pump configuration.

magnetization, Ms = 1.3×10^5 A/m (=130 emu/cm^3 in electromagnetic units), and the gyromagnetic ratio of electron, $\gamma = 1.76 \times 10^{11}$ rad s^{-1}T^{-1} ($= 1.76 \times 10^7$ s^{-1}Oe^{-1}) are used. The temperature of the sample, T = 300 K. A bias field of 100 Oe is used. Periodic boundary conditions are assumed in the lateral directions. The dispersion relation calculated is shown below.

B. Magnon number calculations

In the process of determining the dispersion relations, we also obtain $\mathcal{M}(k_y, k_x; t)$ as an intermediary result (Eq. 2.7) which is a measure of the magnon amplitude with wave-vector (k_y, k_x) at the time instant, *t*. This can provide crucial information about magnon dynamics. It is possible to track magnons with specific wave-vector and/or energies. Below we show magnons resolved in frequency and wave-vector.

Next, I present some results obtained for the parallel pumping configuration wherein both the magnetic bias field as well as the microwave field (h_{rf}) are applied parallel to each other (along the z-direction) as depicted in Fig. 2.10. This usually leads to magnon modes in a plane perpendicular to the z-direction. (The same configuration as was used to obtain the dispersion relation shown in Fig. 2.9.) The simulations are performed in this plane for increased resolution of the significant magnon modes [112]. The discretization used is 128x128x1 along x-, y- and z-directions with dimensions 5.1 um x 100 um x 1250 um, respectively. I use $M_s = 145\ emu/cm^3$, $\alpha = 0.007$ and $A_{ex} = 3.77 \times 10^{-7}\ ergs/cm$. A 6 GHz microwave is turned on at 100 ns.

In Fig. 2.11 (a), I demonstrate that the $\omega_p/2$ modes are excited when a microwave frequency of ω_p is used for pumping. Modes with other frequencies hardly show an increase in their numbers. It is also demonstrated that $k \neq 0$ modes can be directly excited

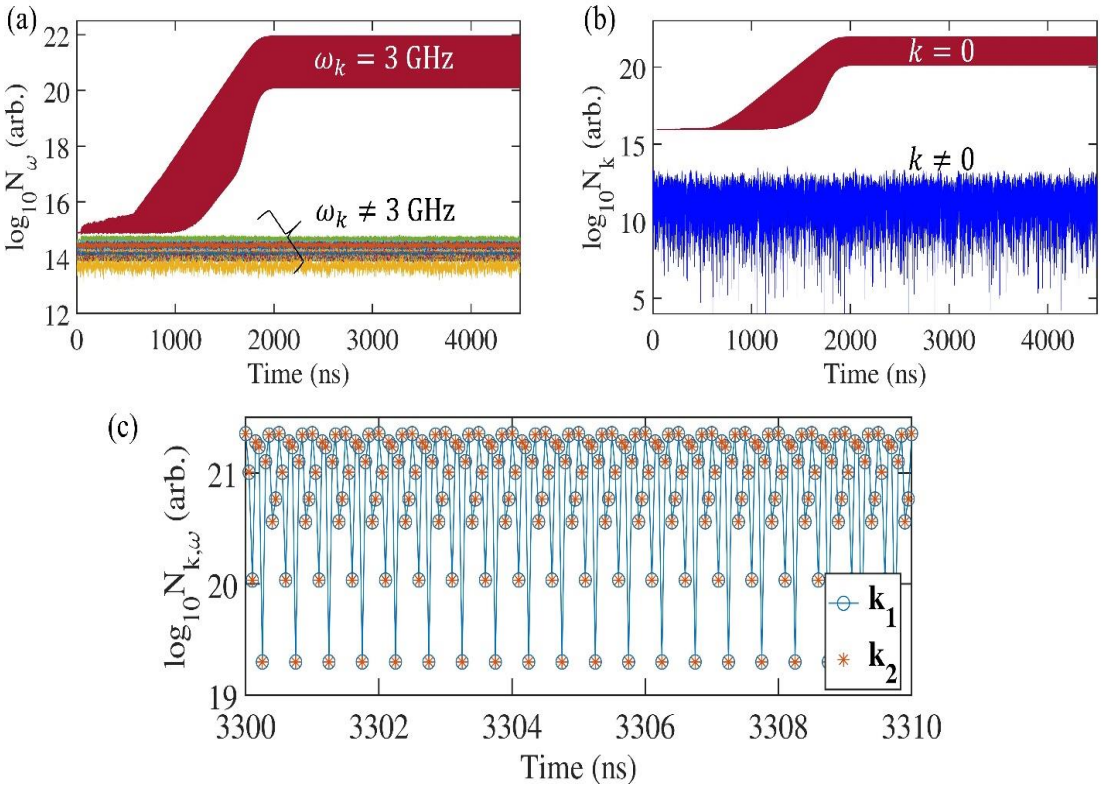

Fig. 2.11. Demonstration of the selectivity during the magnon growth process. (a) Magnon numbers resolved in frequency. Turning on a 6 GHz microwave frequency with an intensity of 24.4 Oe, leads to an exponential growth in the number of 3 GHz magnons. The rest of the magnons do not show this growth and remain close to the equilibrium values. (b) Magnon numbers resolved in wave-vectors. Wave-vector based analysis suggest that the magnons with their wavevectors $k \neq 0$ can be directly excited (i.e., without involving the $k = 0$ modes). (c) Magnon number growth of two of the most dominant magnon-modes resolved in both frequency and wave-vectors. Wave-vectors of the two modes are such that $\mathbf{k_1} = -\mathbf{k_2}$, with $|k_{1x}| = |k_{2x}| = 19.7 \times 10^4 \mathrm{rad/cm}$ and $|k_{1y}| = |k_{2y}| = 1.26 \times 10^4 \mathrm{rad/cm}$ and the frequency of the modes, $\omega_k = 3$ GHz. These two modes exhibit identical numbers through the entirety of the simulation time, indicating pair interaction of the magnons. Oscillations are due to the interplay between the pumping and the various relaxation processes. Source: [107]

by the microwave (Fig. 2.11 (b)) (More discussions can be found in [41], [110].) To the best of our knowledge, this was the first micromagnetics-based demonstration of the phenomenon at the time of publication [107]. Since the wave-vector-based resolution is

hard to obtain experimentally, this demonstration represents a micromagnetic proof supporting the direct excitation of non-uniform magnons by microwave photons.

In Fig. 2.11 (c), we plot the two most dominant magnon modes and find that these occur in pairs ($\pm\boldsymbol{k}$), which is not surprising given the wave-vector conserving nature of 3- and 4- magnon interactions. It is interesting to note, however, that the numbers remain identical for the two components ($\pm\boldsymbol{k}$) even under higher-order interactions (beyond 1000 ns) that arise naturally in the magnetic-material, e.g., the phase-mismatch mechanism (discussed in Chapter 7), to which the modes are eventually subjected. This indicates that the two modes act as though they are a single unit, similar to the notion of Cooper pairs in superconductors [57, 110], i.e., the interacting unit is a magnon-pair. Although we discussed only some of the phenomena here, other magnon-based processes can also be captured using our heterogenous micromagnetics tool.

2.5 Conclusions

In this chapter, I have described the implementation of the CUDA-GPU-based micromagnetics tool that would be used to investigate various aspects of magnons in the chapters to follow. The computation of various magnetic fields: thermal, exchange, dipolar or demagnetization, and applied -is discussed. The procedure for dispersion relation and magnon dynamics calculation from micromagnetic simulation data is also described. In terms of runtime, a 5000 ns long run with a timestep of 500 fs computing a 16384-celled system takes about 7.5 hours on a V100 GPU and about 14 hours on P100 GPU.

Chapter 3

Spin-Wave Theory and Frequency Selective Limiter Functionality

In this chapter, I develop and discuss spin-wave theory for parallel pump configuration that could enable a better understanding and design of magnetics-based microwave devices. For this, I make use of the mathematical mechanics of second quantization that interprets spin waves as particles. Similar use has been made of the Holstein-Primakoff (HP) transformation [122], as was done, for example, in prior works of Suhl [54] and Schlomann [123]. One of the key differences is that my theory is for thin films while the prior theories considered spherical samples. In addition, I discuss aspects of HP parameters that were not explicitly considered in the original works; physical interpretation of the mathematical equations is also provided. The theory developed herein would form the basis for further chapters of this thesis.

I will then demonstrate the functionality of frequency selective limiters (FSLs) in light of the developed spin-wave theory using micromagnetic simulations. Important nonlinear device characteristics with respect to absorption, bandwidth, etc., are discussed. Three- and four-particle scattering processes are shown to be the cause of such nonlinearities. The nonlinear properties have a strong dependence on the magnetic bias field, microwave frequency, and applied power, etc. Predictions are calculated using a large-scale micromagnetic simulation executed on GPUs [107], [112].

3.1 Spin-Wave Equation of Motion

Let us define the following frequencies: $\omega_H \equiv \gamma H_{dc}$; $\omega_M \equiv \gamma 4\pi M_S$; $\omega_d \equiv \gamma h_d$; $\omega_{ex} \equiv \gamma h_{ex}$; and $\omega_s \equiv \gamma h_{rf}$, where h_d represents the dipolar field. The fields- H_{dc},

h_{rf} and $4\pi M_S$ (magnetic saturation induction, an effective field component) can be assumed to have a linear polarization. Also, I have ignored the effective thermal field in the analytical theory.

Let us make the following definitions: $\frac{\boldsymbol{M}}{M_s} \equiv \boldsymbol{m}$, with components (m_x, m_y, m_z) and $m^+ \equiv m_x + im_y$, and $m^- = (m^+)^* \equiv m_x - im_y$, where *i* is imaginary. From which, we can write: $m_z = \sqrt{1 - m^+m^-} \approx 1 - \frac{1}{2}m^+m^-$ $(\because |\boldsymbol{m}| = 1 \Longrightarrow m_x^2 + m_y^2 + m_z^2)$. Further, we have in the transform space: $a_k = m_{kx} + im_{ky};\ a_{-k}^* = m_{kx} - im_{ky}.\ a_k, a_{-k}^*$ can also be considered as the magnon creation and destruction operators with wave-vector +*k* and -*k*, respectively.

Consider the Landau-Lifshitz equation normalized w.r.t the saturation magnetization, M_S:

$$\frac{d\boldsymbol{m}}{dt} = -\gamma(\boldsymbol{m} \times H_{eff}) \tag{3.1}$$

where, H_{eff} represents the effective field experienced by $\boldsymbol{m}$; separating into Cartesian components, we get:

$$\frac{dm_x}{dt} = -\gamma\big(m_y H_Z - m_z H_y\big);\ \frac{dm_y}{dt} = -\gamma(m_z H_X - m_x H_z)$$

where, H_Z, H_Y, H_X represent the effective field components along the Cartesian directions.

$$\frac{dm_x}{dt} + i\frac{dm_y}{dt} = \dot{m}^+ = i\gamma m^+(H_z) - i\gamma m_z\big(H_x + iH_y\big) \tag{3.2}$$

Therefore,

$$\dot{m}^+ = im^+[\omega_z + \omega_{dz} + \omega_{ex}l^2\nabla^2 m_z] - im_z[\omega_s \cos\big(\omega_p t\big) + \omega_{ex}l^2\nabla^2 m^+ + \omega_{dx} + i\omega_{dy}] \tag{3.3}$$

Taking the spatial Fourier transform, we obtain:

$$-i\dot{a}_k = A_k a_k + B_k a^*_{-k} + \omega_s \cos(\omega_p t)\, a_k \tag{3.4}$$

where, $A_k = \omega_H + \omega_{ex} l^2 k^2 + \omega_M \left(T_k^{xx} + T_k^{yy}\right);\ B_k = \omega_M (T_k^{xx} - T_k^{yy})$

with, $T_k^{xx} \equiv -4\pi[1 - G(kD)];\ T_k^{ij} \equiv -4\pi G(kD) \frac{k_i k_j}{k^2};\ G(x) = 1 - \frac{1-e^{-x}}{x}$

The demagnetization factors T_k's are explained in [115]. The physical significance of the above Eq. (3.3) is that it leads to the "first-order" spin-wave instability effect, which is an important physical phenomenon that will be discussed at length in this chapter and used widely in this thesis.

A. HP Transformation and dispersion relations

One of the classical mathematical tools developed in the study of magnetics is the Holstein and Primakoff (HP) transformation [122]. This transformation allows us to diagonalize the matrix equations corresponding to Eq. (3.4):

$$\frac{d}{dt}\begin{pmatrix} a_k \\ a^*_{-k} \end{pmatrix} = i \begin{bmatrix} A_k & B_k \\ -B_k^* & -A_k \end{bmatrix} \begin{pmatrix} a_k \\ a^*_{-k} \end{pmatrix} \tag{3.5}$$

Eq. (3.5) represents two coupled oscillators a_k and a^*_{-k}: the normal modes and the corresponding frequencies can be obtained using a suitable linear transformation.

Let us first define $\begin{pmatrix} b_k \\ b^*_{-k} \end{pmatrix}$ to be the basis which diagonalizes Eq. (3.5) such that:

$$\begin{pmatrix} b_k \\ b^*_{-k} \end{pmatrix} \equiv \begin{bmatrix} \lambda_k & \mu_k \\ \mu_k^* & \lambda_k \end{bmatrix} \begin{pmatrix} a_k \\ a^*_{-k} \end{pmatrix} \tag{3.6}$$

The above is called the Holstein-Primakoff transformation. The idea is to get a linear transformation that will decouple the coupled (a_k, a^*_{-k}) modes. λ_k, μ_k are the HP parameters.

As was pointed out during the discussion of dipolar fields in Chapter 1 (Section 2.3(C)), the uniform mode is an eigenmode only to the first order in the presence of dipolar fields. In general, we must consider the nonuniform modes. Physically, the HP transformations allow the conversion from a circular basis to an elliptical basis, which diagonalizes the above matrix equations. Bogoliubov transformations, encountered in the study of superconductors, mathematically perform the same function [124]. The goal of this section is to study the various parameters involved that are important for spin-wave investigations but have not been detailed in the original work [122].

The equation (3.6) implies:

$$\begin{pmatrix} a_k \\ a^*_{-k} \end{pmatrix} = \frac{1}{{\lambda_k}^2 - |\mu_k|^2} \begin{bmatrix} \lambda_k & -\mu_k \\ -\mu^*_k & \lambda_k \end{bmatrix} \begin{pmatrix} b_k \\ b^*_{-k} \end{pmatrix} \tag{3.7}$$

Using (3.7) in (3.5) gives:

$$\frac{1}{{\lambda_k}^2 - |\mu_k|^2} \begin{bmatrix} \lambda_k & -\mu_k \\ -\mu^*_k & \lambda_k \end{bmatrix} \frac{d}{dt} \begin{pmatrix} b_k \\ b^*_{-k} \end{pmatrix} = i \begin{bmatrix} A_k & B_k \\ -B^*_k & -A_k \end{bmatrix} \begin{bmatrix} \lambda_k & -\mu_k \\ -\mu^*_k & \lambda_k \end{bmatrix} \begin{pmatrix} b_k \\ b^*_{-k} \end{pmatrix} \tag{3.8}$$

$$\Rightarrow \frac{d}{dt} \begin{pmatrix} b_k \\ b^*_{-k} \end{pmatrix} = \begin{bmatrix} \lambda_k & \mu_k \\ \mu^*_k & \lambda_k \end{bmatrix} \begin{bmatrix} A_k & B_k \\ -B^*_k & -A_k \end{bmatrix} \begin{bmatrix} \lambda_k & -\mu_k \\ -\mu^*_k & \lambda_k \end{bmatrix} \begin{pmatrix} b_k \\ b^*_{-k} \end{pmatrix} \tag{3.9}$$

$$= \begin{bmatrix} {\lambda_k}^2 A_k - \mu_k \lambda_k B_k - \mu^*_k \lambda_k B_k + |\mu_k|^2 A_k & -\mu_k \lambda_k A_k + {\mu_k}^2 B_k + {\lambda_k}^2 B_k - \mu_k \lambda_k A_k \\ 2\mu^*_k \lambda_k A_k - {\lambda_k}^2 B_k - \mu^{*2}_k B_k & -|\mu_k|^2 A_k + \mu_k \lambda_k B_k + \mu^*_k \lambda_k B_k - {\lambda_k}^2 A_k \end{bmatrix} \begin{pmatrix} b_k \\ b^*_{-k} \end{pmatrix} \tag{3.10}$$

By definition $\begin{pmatrix} b_k \\ b^*_{-k} \end{pmatrix}$ diagonalizes Eq. (3.5). One can, therefore, find the eigenvalue ω_k as:

$$\begin{vmatrix} A_k - \omega_k & B_k \\ -B^*_k & -A_k - \omega_k \end{vmatrix} = 0 \tag{3.11}$$

$$\Rightarrow \omega_k = \sqrt{A_k^2 - |B_k|^2} \tag{3.12}$$

Physically, ω_k is the frequency of the spin-wave with the wave-vector, *k*. (Since the corresponding energy is $\hbar\omega_k$, ω_k can also be considered as the normalized energy. We keep only the positive solution in Eq. (3.12)) In fact, Eq. (3.12) represents the dispersion relation of magnons (discussed in Chapter 2, Section 2.4 (A)) and represents a key result from the spin-wave theory.

Also,
$$\frac{d}{dt}\begin{pmatrix} b_k \\ b_{-k}^* \end{pmatrix} = i\begin{bmatrix} \omega_k & 0 \\ 0 & \omega_k \end{bmatrix}\begin{pmatrix} b_k \\ b_{-k}^* \end{pmatrix} \tag{3.13}$$

Eq. (3.13) has simple uncoupled solutions of the form:

$$b_k(t) = b_{k0}e^{i\omega_k t} \text{ (and } b_{-k}^*(t) = b_{-k0}^* e^{-i\omega_k t}) \tag{3.14}$$

Using Eq. (3.10) and Eq. (3.13), gives:

$$-\mu_k\lambda_k A_k + {\mu_k}^2 B_k + {\lambda_k}^2 B_k - \mu_k\lambda_k A_k = 0$$

$$2\mu_k^*\lambda_k A_k - {\lambda_k}^2 B_k^* - \mu_k^{*2} B_k = 0$$

$$\Rightarrow {\mu_k}^2 B_k^* + {\lambda_k}^2 B_k = 2\mu_k\lambda_k A_k \tag{3.15(a))}$$

$$\lambda_k^{\,2} B_k^* + \mu_k^{*2} B_k = 2\mu_k^*\lambda_k A_k \tag{3.15(b))}$$

Solving for μ_k^* in Eq. (3.15) gives:

$$\mu_k^* = \lambda_k\left(\frac{A_k \pm \sqrt{A_k^2 - |B_k|^2}}{B_k}\right) \tag{3.16}$$

In addition, the H.P transformation also requires:

$${\lambda_k}^2 - |\mu_k|^2 = 1 \tag{3.17}$$

Using Eq. (3.16) and Eq. (3.17):

$$\left(\left|\frac{\lambda_k}{\mu_k^*}\right|\right) = \frac{|B_k|}{|A_k - \omega_k|} \Rightarrow \frac{|{\lambda_k}^2|}{|\mu_k^{*2}|} - 1 = \frac{|B_k|^2 - A_k^2 - \omega_k^2 + 2A_k\omega_k}{|A_k - \omega_k|^2} \Rightarrow \frac{1}{|\mu_k^{*2}|} = \frac{2\omega_k}{A_k - \omega_k} \tag{3.18}$$

which gives,

$$\mu_k = \sqrt{\frac{A_k-\omega_k}{2\omega_k}}\frac{B_k}{|B_k|}\ (= \sqrt{\frac{A_k-\omega_k}{2\omega_k}} \text{ for } B_k \text{ real})$$

$$\Rightarrow \lambda_k = \sqrt{\frac{A_k+\omega_k}{2\omega_k}}$$

Therefore, for real B_k:

$$\mu_k = \sqrt{\frac{A_k-\omega_k}{2\omega_k}}\ \&\ \lambda_k = \sqrt{\frac{A_k+\omega_k}{2\omega_k}} \tag{3.19}$$

However, the above form is not unique; one can, e.g., by choosing $\frac{A_k}{\omega_k} = \cos(\psi_k)$ and $\frac{B_k}{\omega_k} = \sin(\psi_k)$ satisfy Eq. (3.17), giving:

$$\mu_k = \sinh\left(\frac{\psi_k}{2}\right)\ \&\ \lambda_k = \cosh\left(\frac{\psi_k}{2}\right) \tag{3.20(a)}$$

Using Eq. (3.15) and Eq. (3.19):

$$|\lambda_k\mu_k^*| = \frac{{\lambda_k}^2 B_k^* + \mu_k^{*2} B_k}{2A_k} = \frac{\frac{A_k+\omega_k}{2\omega_k}B_k + \frac{A_k-\omega_k}{2\omega_k}B_k}{2A_k} = \frac{B_k}{2\omega_k} \tag{3.20(b)}$$

Equation (3.20) gives an important relationship between the HP parameters and physical parameters of the magnetic system.

B. Equation of motion Parallel pump configuration

Next, let us revisit the equation of motion with the aim of framing it in the language of spin waves, specifically suited for parallel pump configuration. This is different from Suhl's analysis which considered the perpendicular pumping case. Spin-wave instability processes, which are central to the research described in the thesis, would also be discussed mathematically.

Solving for a_k and a_{-k}^* in terms of b_k and b_{-k}^*, we get: μ_k^*

$$a_{-k}^* = \lambda_k b_{-k}^* - \mu_k^* b_k$$

$$a_k = \lambda_k b_k - \mu_k b_{-k}^* \tag{3.21}$$

Using Eq. (3.21) in Eq. (3.4) gives

$$\lambda_k \dot{b_k} - \mu_k \dot{b}_{-k}^* = i[A_k\lambda_k b_k - A_k\mu_k b_{-k}^* + B_k\lambda_k b_{-k}^* - B_k\mu_k^* b_k + \gamma h_{rf}\lambda_k b_k \cos(\omega_p t) -$$

$$\gamma h_{rf}\mu_k b_{-k}^* \cos(\omega_p t)] \tag{3.22(a))}$$

$$\lambda_k \dot{b}_{-k}^* - \mu_k^* \dot{b_k} = -i[A_k\lambda_k b_{-k}^* - A_k\mu_k^* b_k + B_k^*\lambda_k b_k - B_k^*\mu_k b_{-k}^* + h_{rf}\lambda_k b_{-k}^* \cos(\omega_p t) -$$

$$\gamma h_{rf}\mu_k^* b_k \cos(\omega_p t)] \tag{3.22(b))}$$

Or in other words,

$$\begin{bmatrix} \lambda_k & -\mu_k \\ -\mu_k^* & \lambda_k \end{bmatrix} \begin{pmatrix} \dot{b}_k \\ \dot{b}_{-k}^* \end{pmatrix} =$$

$$i \begin{bmatrix} A_k\lambda_k - B_k\mu_k^* + \gamma h_{rf}\lambda_k \cos(\omega_p t) & -A_k\mu_k + B_k\lambda_k - \gamma h_{rf}\mu_k \cos(\omega_p t) \\ A_k\mu_k^* - B_k\lambda_k + \gamma h_{rf}\mu_k^* \cos(\omega_p t) & -A_k\lambda_k + B_k\mu_k^* - \gamma h_{rf}\lambda_k \cos(\omega_p t) \end{bmatrix} \begin{pmatrix} b_k \\ b_{-k}^* \end{pmatrix} \tag{3.23}$$

$$\begin{pmatrix} \dot{b}_k \\ \dot{b}_{-k}^* \end{pmatrix}$$

$$= i \begin{bmatrix} A_k\lambda_k^2 - B_k\mu_k\lambda_k - B_k\mu_k^*\lambda_k + A_k|\mu_k|^2 & -A_k\mu_k\lambda_k + B_k\mu_k^2 + B_k\lambda_k^2 - A_k\lambda_k\mu_k \\ A_k\mu_k^*\lambda_k - B_k\lambda_k^2 - B_k\mu_k^2 + A_k\mu_k^*\lambda_k & -A_k|\mu_k|^2 + B_k\mu_k\lambda_k + B_k\mu_k^*\lambda_k - A_k\lambda_k^2 \end{bmatrix}$$

$$+ \begin{bmatrix} (|\mu_k|^2 + \lambda_k^2)\gamma h_{rf}\cos(\omega_p t) & -2\mu_k\lambda_k\gamma h_{rf}\cos(\omega_p t) \\ 2\mu_k^*\lambda_k\gamma h_{rf}\cos(\omega_p t) & (|\mu_k|^2 + \lambda_k^2)\gamma h_{rf}\cos(\omega_p t) \end{bmatrix} \begin{pmatrix} b_k \\ b_{-k}^* \end{pmatrix} \tag{3.24}$$

Along with Eq. (3.10), the above equation implies:

$$\dot{b}_k = i\omega_k b_k - i2\mu_k\lambda_k\gamma h_{rf}\cos(\omega_p t) b_{-k}^*$$

$$\dot{b}_k = i[\omega_k b_k - \rho_k \cos(\omega_p t)] b_{-k}^* \tag{3.25}$$

Where using Eq. (3.20), we have: $\rho_k \equiv 2\mu_k\lambda_k\gamma h_{rf} = \frac{B_k}{\omega_k}\gamma h_{rf}$ (3.26)

Eq. (3.25) is the equation of motion for parallel pump excitation of magnons (ignoring 4- (and higher) particle processes). Apart from its significance in helping us understand the physics of magnon dynamics, it is also of immense significance from the perspective of applications, as will be seen in the subsequent discussions.

Spin-wave instabilities can show up due to terms that are first order in b_k's and contain h_{rf}, e.g., the second term of Eq. (3.25). Note that in the absence of the second term, the equation is that of a simple harmonic oscillator. The additional term can hence be seen as an external force applied to the oscillator. It is this term that can lead to the parametric coupling and growth of spin waves. However, there remains to be considered one final part of the puzzle- the dissipation.

To study the first-order instability effects, it is necessary to introduce dissipation into the magnetic system. This will be done phenomenologically, as was done by Suhl [125], [126], Schlomann [127], and others [41, 121, 128]. From a material perspective, real magnetic systems like ferrimagnets (or ferromagnets) are complex materials with a plethora of physics at play, involving multiple dissipation channels. Phenomenologically, the dissipation of the spin-wave with wave-vector, *k*, is represented by an effective loss term, η_k such that $D_k = \omega_k + i\eta_k$. Eq. (3.25) now becomes:

$$\dot{b}_k = iD_k b_k - i2\mu_k\lambda_k h_{rf}\cos(\omega_p \mathrm{t})b^*_{-k} \quad (3.27)$$

To identify the frequency of importance, without loss of generality, we can assume b_k to vary as: $b_k \sim \exp(i\,\varpi_k t - \xi_k t)$. By definition of D_k, when $h_{rf} = 0$, $b_k \sim \exp$

($i\,\omega_k t - \eta_k t$). The forcing term on the right-hand side (RHS) of Eq. (3.27) can initiate resonance if the net frequency on the right ($-\varpi_k \pm \omega_p$) equals that on the left, ϖ_k, implying (ω_p being the pump frequency):

$$|\varpi_k| = \omega_p/2 \tag{3.28}$$

This result, although relatively simple, is due to one of the most important scattering processes: the 3-particle scattering process. Herein, the onset of instability is brought about by magnons with energy: $\hbar\omega_p/2$, i.e., half the energy of the RF (or microwave) photon. Such processes will be explained in Section 3.3.

3.2 Microwave Threshold for Instability

Now that we have determined the relationship between the frequencies of the pump and the unstable mode, let us look into the conditions that would lead to the growth of the unstable mode. Using $b_k \sim \exp(i\,\varpi_k t - \xi_k t)$ in Eq. (3.27) gives:

$$[(\omega_k - \varpi_k) - i(\xi_k - \eta_k)]b_k = \rho_k b^*_{-k}\cos(\omega_p \mathrm{t}) \tag{3.29}$$

Now, to find the threshold field set $\varpi_k = \frac{\omega_p}{2}$. Keeping only the resonant term, gives:

$$\xi_k = -\eta_k + [\tfrac{1}{4}|\rho_k|^2 - (\omega_\mathrm{k} - \omega_p/2)^2]^{\frac{1}{2}} \tag{3.30}$$

At the threshold of instability $\xi_k = 0$ (physically this implies no dissipation of the corresponding mode allowing it to grow exponentially), giving $|\rho_k|^2 = 4[\eta_k^2 + (\omega_\mathrm{k} - \omega_p/2)^2]$. Consequently, the relation between threshold microwave field for an arbitrary spin wave frequency, ω_k, and other material parameters is:

$$h_{thg} = \frac{2\omega_k[\eta_k^2+(\omega_k-\omega_p/2)^2]^{\frac{1}{2}}}{\gamma\omega_M(T_k^{xx}-T_k^{yy})} \tag{3.31}$$

The threshold field required to initiate the most unstable mode can be obtained by minimizing the above expression with respect to wave-vector, k for $\omega_k = \frac{\omega_p}{2}$:

$$h_{th} = \frac{\omega_p\eta_k}{\gamma\omega_M(T_k^{xx}-T_k^{yy})_{max.}} \tag{3.32}$$

where *k* in the denominator is chosen to minimize h_{th}.

The threshold field at a given microwave frequency represents the minimum field required to overcome the magnon dissipation and trigger the instability processes. In a large number of cases, the instability process of interest is the 3-particle scattering. However, in cases where 3-particle scattering processes are not allowed in the system, e.g., due to the unavailability of the relevant half energy states in the dispersion, the dominant scattering processes are the 4-particle scattering.

3.3 Nonlinear Processes

A. Three Particle Scattering

Three-particle scattering (or three-wave scattering) is one of the most important parametric nonlinear processes to occur in magnon-microwave interactions [54, 110]. This interaction involves the creation of two magnons at the expense of a microwave photon (characterized by energy $\hbar\omega_p$).

In such processes, a photon is absorbed to produce two quanta of magnetic excitation (magnons) such that:

$$\omega_p(k_p) = \omega_{m1}(k_{m1}) + \omega_{m2}(k_{m2}) \text{ with } \omega_{m1} = \omega_{m2} = \frac{\omega_p}{2} \tag{3.33}$$

$$k_p = k_{m1} + k_{m2} = 0 \implies k_{m1} = -k_{m2} \tag{3.34}$$

where the subscripts p, m1, m2 stand for the photon and the two magnons, respectively. Thus, it was no coincidence that in Eq. (3.28), the energy of the magnons turned out to be $\omega_p/2$. There are two conditions that must be met in order to initiate the 3-particle scattering:

(i) As can be inferred from Eq. (3.31), half energy states (w.r.t the microwave pump frequency) must be present in the magnon dispersion relation so that the magnons can scatter to this mode upon excitation. Mathematically, this requires the relevant ω_k [Eq. (3.12)] to be real, if not, the three-wave processes are forbidden.

(ii) As mentioned earlier (Section 3.2), the strength (magnetic field intensity) of the microwave signal must exceed a certain threshold intensity (h_{th}) for such processes to occur.

A typical 3-magnon process is illustrated in Fig. 3.1(a), where a ω_p microwave photon (with $h > h_{th0}$) can be seen to excite two $\omega_p/2$ magnons.

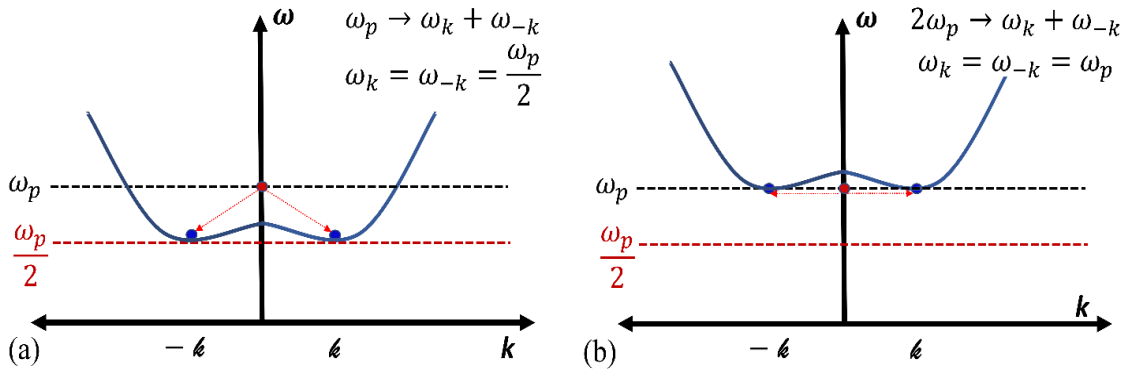

Fig. 3.1. Schematic showing the 3- and 4-magnon processes. (a) Three particle scattering process involves 3 particles: a photon and two magnons. Absorption of a photon at ω_p results in the creation of two magnons with half the energy, $\omega_p/2$. (b) Four particle scattering process involves the absorption of two microwave photons at ω_p to create two magnons with the same energy ω_p. (Source: [129])

B. Four-particle scattering

Three magnon processes, however, are not allowed to occur when the magnetic system does not possess states corresponding to half the energy of the pump microwave. The simplest scattering processes in such cases are the 4- particle scattering processes [110, 121, 130]. Herein, as shown in (Fig. 3.1 (b)), two photons with energy ω_p, are absorbed by the magnetic material to produce two magnons with the same energy (ω_p) while conserving the net momentum during the interaction. The conservation conditions in such cases are:

$$2\omega_p(k_p) = \omega_{m1}(k_{m1}) + \omega_{m2}(k_{m2}) \tag{3.35}$$

$$2k_p = k_{m1} + k_{m2} = 0 \implies k_{m1} = -k_{m2} \tag{3.36}$$

Due to the involvement of four particles, this process is called four-particle scattering. Again, we see that the dispersion relation plays a decisive role in determining and governing the decay process.

In general, processes higher than four-particle processes are possible, e.g., they

occur in physical systems like plasma. However, as a certain scattering process is triggered, most of the incident microwave energy goes into this scattering process, thereby preventing still higher-order processes from occurring. For example, once three-particle processes are initiated, they dominate the scattering mechanism, and only a weak 4-magnon scattering may be produced with a further increase in microwave power [107]. In general, as the order increases, the threshold field requirement increases. This can be seen as a consequence of the increasing difficulty of bringing together the said number of particles for the scattering to occur.

The three and four-particle scattering processes are crucial for the design of the various applications mentioned in Chapter 1. In this chapter, we specifically consider the case of frequency selective limiters.

At this point, we have established some key qualitative results by means of which we can understand the high-power experiments performed by Bloembergen-Wang, and Damon *et al.* mentioned earlier (Chapter 1 Section 1.6). There are some differences from the current discussion, as the experiments were performed in perpendicular pump configuration. Apart from the change in the directions in which various quantities change, the qualitative description developed above can be applied to understand these experiments.

In the case of ferri(ferro)magnets, for small microwave excitation, the modes are independent of each other, but nonlinearities may lead to coupling between the modes. For example, in Eq. (3.25) (or even Eq. (3.27)), the second term of the right-hand side indicates coupling between b_{-k}^{*} and h_{rf}. It is this coupling that led to the three-particle scattering.

In the case of perpendicular pumping instead of h_{rf}, it is the directly excited uniform mode, b_0, that is coupled with the $k \neq 0$ magnons, resulting in nonlinear effects like three-magnon scattering (all the three particles involved are magnons). The microwave photon excites the uniform mode, which then leads to the nonuniform modes. (In perpendicular pumping, therefore, all the 3 particles are magnons, i.e., a $k=0$ magnon with energy, ω_p, gives rise to 2 magnons of energy $\omega_p/2$ and wave-vectors +k and -k.)

In the case of paramagnets, the m_z and μ''were found to decrease together. The energy from the microwave was absorbed in the magnetic material, and this reduced the saturation, bringing down m_z. This is because the spins, or more appropriately, the magnetic moments of a paramagnetic material, are not tightly bound as in the case of ferri(ferro)magnets. In the case of the ferrimagnets, however, while the energy is absorbed, it largely goes to create nonuniform modes (i.e., modes with $k \neq 0$ are created) instead of reducing the magnitude of m_z. This explains why the permeability curve shows a decrease while the m_z curve does not, in Fig. 1.7(b). The saturation of the main peak observed in the experiments was attributed to 4-magnon scattering, while the subsidiary peaks at lower bias fields were attributed to 3-magnon scattering at these fields.

3.4 Frequency Selective Limiter Design Considerations

The nonlinear magnetic response of ferrites (e.g., YIG) makes them a good candidate for frequency-sensitive microwave (RF) devices like FSLs, wherein the magnetic response is used to effect changes in the strength of the incoming RF signal [17], [19]. Furthermore,

in RF applications, the low intrinsic magnetic damping of ferrites like YIG improves the efficiency with which the microwave signals interact with the material [131], making magnetics useful even for low RF power scenarios. State-of-the-art devices often employ doped YIG to further tune device properties like bandwidth and threshold for FSL based applications [1].

In this section, we look at some of the design considerations from the perspective of spin-waves using the micromagnetics solver developed in Chapter 2.

A. Simulation Details

A magnetic bias field (H_{dc}) is applied in the plane of the film along the z-direction. A linearly polarized RF signal with angular frequency ω_p and amplitude h_0 Oe [$h_{rf} = h_0 \cos(\omega_p t)$] is applied parallel to the bias field. Fig. 2.10 shows the designation of directions used in the parallel pump configuration as well as a typical sample used in this work. Constants used are: intrinsic magnetic damping constant, α =0.0028; saturation magnetization, Ms = 1.3×10^5 A/m (=130 emu/cm^3 in electromagnetic units); the gyromagnetic ratio of electron, $\gamma = 1.76 \times 10^{11}$ rad s^{-1}T^{-1} ($= 1.76 \times 10^7$ s^{-1}Oe^{-1}). The system is allowed to relax for 300 ns under the application of thermal field h_t [132] (temperature T=300 K) and applied bias field H_{dc}, before the linearly-polarized RF field is turned on. The demagnetization fields are computed using Newell's algorithm, as explained in Chapter 2. The dominant spin-wave wavelengths observed are ~0.1 μm to 10 μm in length. This helps justify the rather large cell sizes used in our simulations compared to the exchange length (~20 nm) [133]. The ferrimagnet YIG is modelled as a

ferromagnet [110]. We work under the magnetostatic approximation: $\nabla \times \boldsymbol{H} = 0$, where $\boldsymbol{H}$ is the internal magnetic field of the material.

C. Power Dependence

I begin my study of the role of spin waves in FSLs by determining the threshold field at different microwave frequencies. I also look at magnetic susceptibility (imaginary part, χ'', a measure of the absorption of the RF signal by the material) of RF signals at various frequencies. Fig. 3.2 and Fig. 3.3 show the corresponding results.

The curves of Fig. 3.2 can be seen to exhibit the transfer characteristics needed for FSLs as discussed in Fig 1.2 (Chapter 1). Let us specifically look at the 5 GHz curve in Fig. 3.2. At low microwave power, the susceptibility (χ'') and hence the absorption of the microwave by the magnetic material is low. This allows almost all of the input microwave power to reach the output of the FSL. The curve displays a knee at about $\sim 1.0 \times 10^{-2}$ Oe, which represents the threshold field for the 5 GHz signal. Beyond this field strength, there occurs an abrupt increase in absorption. This is the much sought-after nonlinear behavior required for the FSL functionality, responsible for the dips or notches in the transfer function. Similar nonlinear behavior is seen at other frequencies as well. Hence, we have demonstrated that we can indeed capture and study the crucial nonlinear properties that are essential for FSLs, using micromagnetic simulations. At the time of the study [112], this was the first micromagnetic study on FSLs.

The Kittel equation [41, 134, 135] gives the resonance frequency of the system, f_0, to be: $f_0 = (\gamma/2\pi)\sqrt{H_{dc}(H_{dc} + 4\pi M_s)}$. Neglecting the crystalline anisotropy of YIG

[110], for an applied field of 100 Oe, $f_0 = 1.2$ GHz for the thin film. It was discussed in Chapter 1 (Section 1.5) that in the case of parallel pumping, the component of magnetization parallel to the bias field (m_z) oscillates at a frequency twice that of the in-plane components (m_x and m_y). Consequently, the system is most sensitive when a pump frequency (f_p) of 2.4 GHz is applied, which gives an in-plane precession frequency

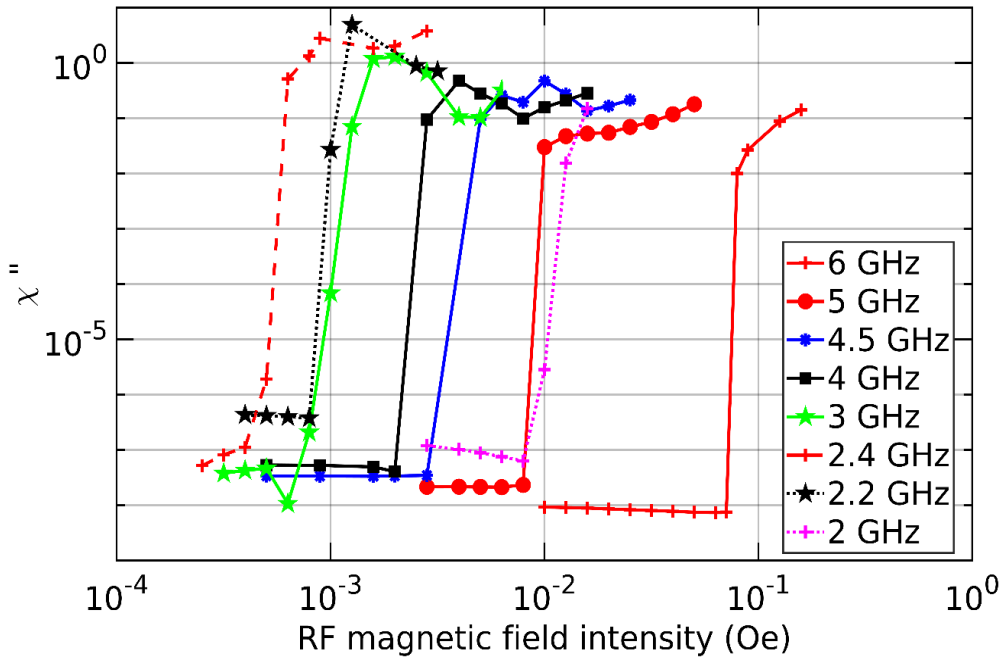

Fig. 3.2. Susceptibility (χ'') vs. RF magnetic field intensity plots for various frequencies, all calculated at 100 Oe. (Source: [112])

of $\frac{f_p}{2} = f_0 = 1.2$ GHz.

The power dependence, as shown in Fig. 3.2, has some interesting characteristics as the system moves from the linear to nonlinear regime. Particularly notable are:

(i) Dependence of threshold for nonlinearity (caused by magnon scattering) on the RF frequency.

(ii) Asymmetry in response w.r.t sign of frequency detuning relative to $2f_0$ (2.4 GHz).

It can be observed that the system is most sensitive at 2.4 GHz as shown by h_{th} (given by the corresponding knee values in the curves of Fig. 3.2), and that the h_{th} increases as we move away from $f_p = 2f_0$(= 2.4 GHz at 100 Oe). The frequencies further away from $2f_0$ need a higher power before the nonlinear processes could be triggered, e.g., an RF field of $\sim 5.0 \times 10^{-3}$ Oe is sufficient to give rise to nonlinear response at 3 GHz, while relatively higher power is needed for 5 GHz. It is only around $\sim 1.0 \times 10^{-2}$ Oe that the latter signal invokes a nonlinear response in the material. These observations can be understood in the light of Eq. (3.31) developed earlier. In other words, mathematically, the observed behavior is a consequence of the threshold being a function of the dispersion relation, illustrating the importance of magnon dispersion for device design.

There exists an asymmetry displayed by the 2 GHz curve w.r.t the other curves in Fig. 3.2. As we move away from the central frequency (2.4 GHz) the threshold is found to increase (as indicated by Eq. (3.31)). The curve of 3 GHz and 2 GHz were expected to have relatively similar h_{th} as they are nearly equidistant in frequency from 2.4 GHz. However, this is not found to be the case, and 2 GHz shows a much higher h_{th}.The asymmetry is due to the dominant four-particle processes [136] at 2 GHz, unlike the 3-particle processes generating most of the rest of Fig. 3.2. As mentioned earlier in Section 3.2**,** three-wave processes are not always allowed. It will be shown later that the lowest frequency on the dispersion relation is a little less than 1.0 GHz for a 10 μm thick sample at 100 Oe, and

hence signals with frequency ≤ 2.0 GHz are disallowed from decaying via three-particle processes. Therefore, when the pump frequency is 2.0 GHz, the simplest scattering mechanism is 4-wave and not the 3-wave process. The 4-wave processes, as explained earlier, have a higher threshold, and this explains the observed asymmetry in Fig.3.2.

B. Frequency Response

Often vital for engineering applications is the frequency response of the device. In order to study this, we sweep the RF pump power applied to the sample under a bias field of 100 Oe at various pump frequencies and obtain h_{th}.

From our simulation (results in Fig. 3.3), we see that the susceptibility shows a peak around 2.4 GHz, thereafter, unlike the case of perpendicular pumping, the response remains

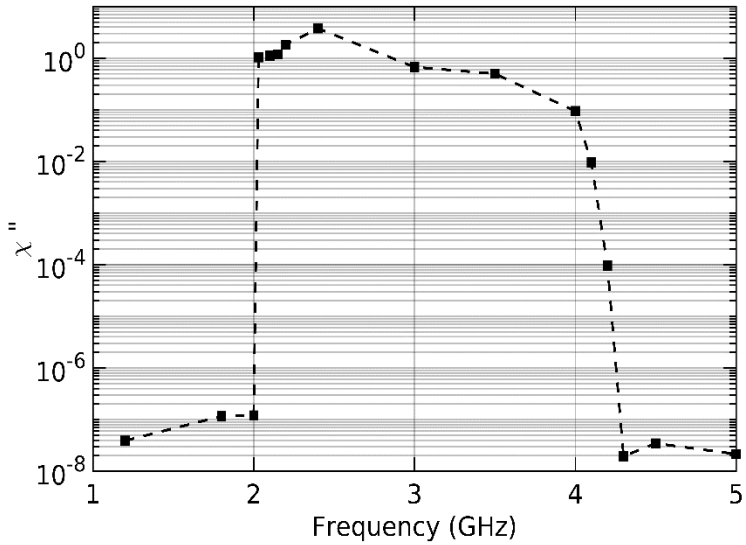

Fig. 3.3. The bandwidth of FSL. Imaginary part of susceptibility (χ'') - a measure of absorption vs. RF (microwave) frequency for a bias field of 100 Oe at RF power of -15 dBm ($h_0 = 0.0028$ Oe). (Source: [112])

finite up to about 4.2 GHz giving a rather large bandwidth of ~ 2.0 GHz. This is in qualitative agreement with the results of Adam *et al.* [137], where similar frequency

characteristics have been observed for strip-line FSL devices with 100 μm thick YIG sample. The higher attenuation seen in [137] is potentially due to the larger volume of YIG seen by the RF field. It would be of importance at this point to realize that the large bandwidth, as can be seen from the data above, is a consequence of magnon scattering.

C. Bias Field Dependence and Butterfly Curve

An important aspect of frequency-sensitive nonlinear devices is what is now known as the "butterfly curve" [22], [26] as shown in Fig. 3.4. It is a plot of the threshold field at various bias fields for a fixed microwave frequency. The data is shown for a frequency of 4 GHz as a function of the bias field for the same geometry as before.

Note that there is a kink in the diagram at about 268 Oe, beyond which the threshold field increases and below which it remains fairly constant. The position of the kink corresponds to that bias-field which gives $\frac{f_p}{2}$ (= 2 GHz) as the natural frequency, i.e., 268

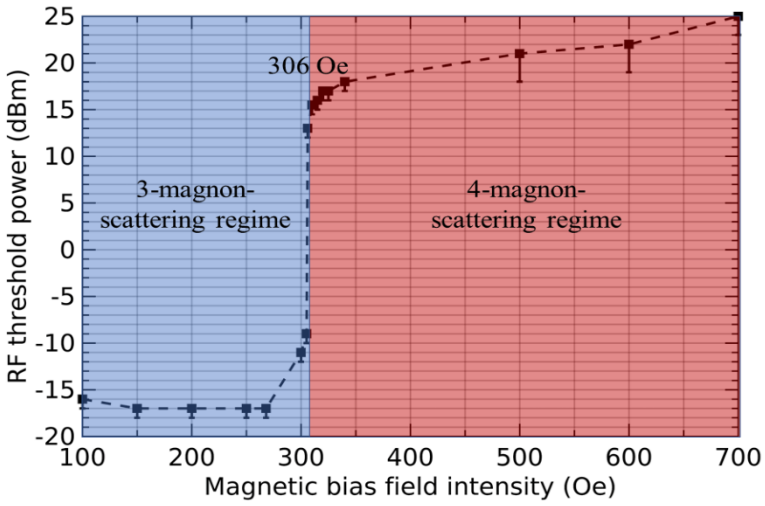

Fig. 3.4. Butterfly curve for an applied pump frequency of 4.0 GHz, showing the two scattering regimes. Source: [112]

Oe, as evaluated using Kittel resonance equation. I would like to point out that the butterfly curve can be understood to be comprised of two different regimes, separated by a *threshold bias-field*, each dominated by a different scattering mechanism. For $H_{bias} < 306 \pm 2$ Oe, simulations show that the dispersion relation is such that it allows three magnon processes (lowest frequency mode allowed is ~ 2 GHz) and consequently, the dominant frequency mode is found to be 2 GHz. However, beyond such a field, the lowest point in the dispersion relation is greater than 2 GHz preventing any scattering into 2 GHz modes, i.e., three-magnon processes, in this case, are disallowed by the dispersion relation. The nonlinearity that occurs now can be attributed to four-particle scattering, wherein the dominant mode has the same frequency as the pump frequency (= 4 GHz in this case).

3.5 Conclusions

A mathematical framework for understanding magnon dynamics under the parallel pumping configuration for thin films has been developed. The method used in the analytical development uses ideas from second-quantization wherein a wave (in this case spin-wave) is treated as a particle (in this case magnons). This technique, alongside the H.P formalism, is a powerful and elegant mathematical tool for understanding magnon-based nonlinear processes, especially when the degree of nonlinearity is low. In this study, I consider low nonlinearity to be the case when the sample remains largely magnetized in the direction of the bias field ($M_z \geq 0.8M_s$). At higher nonlinearities, *chaos* [121] ensues and the resulting processes are beyond the scope of this work.

A mathematical expression for the dispersion relation has also been obtained. Dispersion relations play a crucial role in determining the behavior of the magnetic material under microwave excitation. The dispersion relation, as will be shown in the subsequent chapters, can be tailored using film thickness and bias field.

The behavior of magnetic insulators, such as YIG, under high microwave power, such as that found in FSLs, has long been poorly understood. In particular, quantitatively accurate predictions for susceptibility as a function of material properties and microwave characteristics have been lacking. In this chapter, the ability to make quantitative predictions about the nonlinear response of magnet-based FSLs has been demonstrated. It is found that microwave absorption can be due to 3-particle or 4-particle scattering depending on the dispersion relation of the system.

Chapter 4 Two-dimensional Simulation Paradigm

In Chapter 2, I described the development of a high-speed simulation tool to perform microwave-magnon studies. However, the large number of cells of the magnetic system remains a significant computational challenge even after employing GPU-based acceleration. It was also demonstrated in Chapter 2 that as the number of cells increases, the computational time taken increases exponentially. While the successive new generations of GPUs offer significant speed-ups, much more can be done by employing physics-based optimization to reduce the computational load. In this chapter, I investigate such an optimization that involves reduced dimensional simulations for real magnetic systems, specifically for the parallel pump configuration.

A two-dimensional simulation paradigm is proposed for reducing the computational resource requirements while capturing the qualitative and quantitative behavior of the significant microwave-ferromagnet interactions. Under microwave excitation, the system behavior is largely controlled by a few dominant modes. The idea is to be able to capture the dominant spin-wave modes as these are the modes that govern the nonlinear behavior of the magnetic system. The resolution of these modes is increased at the expense of modes that do not play any major role in the scattering process.

I will first establish the physics behind the 2D simulation technique and then demonstrate the crucial processes of three and four magnon scattering processes using 2D simulations. The dependence of the dispersion relation on film thickness will also be demonstrated using simulations. Finally, I compare the threshold predicted from simulations with experimental values. The simulated predictions for high power

(nonlinear) microwave excitation are in close agreement with the experiment even though the material parameters are only taken from low power (linear) data [112].

4.1 2D Simulations

Due to microwave pumping, spin waves are created that dissipate the RF energy in the magnetic sample. These spin-wave modes can be characterized by their energy ($\hbar\omega_k$) and propagation vector $\vec{\boldsymbol{k}}$, and in general can be surface or bulk waves [138], [139]. The nature of nonlinearity is such that at h_{th} there exists a mode that dominates over all the other modes, governing the scattering process and the resulting nonlinearity. This mode grows exponentially until it gets limited by further decay into other modes. To look at the mode which goes unstable first, I present Table. 4.1, which shows dominant $\vec{\boldsymbol{k}}$ for different pump frequencies at the threshold of nonlinearity.

Pump frequency (f_p, GHz)	Threshold power (dBm)	$\vec{\boldsymbol{k}}(k_x, k_y, k_z)$[a]	Dominant spin-wave frequency (GHz)
2	-2	(3,6,0)	2.0
2.2	-24	(1,2,1)	1.1
2.4	-28	(6,1,0)	1.2
3	-18	(6,1,0)	1.5
4	-12	(5,11,0)	2.0
4.5	-10	(3,10,0)	2.25
5	-2	(2,15,0)	2.5
6	13	(4,13,0)	3.0

Table 4.1: Dominant Mode Details for Input Pump Frequencies. (Source: [112]). [a]The amplitudes of k_x, k_y and, k_z need to be scaled with $S_i = \frac{2\pi}{L_i}$ $(i = x, y, z)$ for conversion to cm^{-1}. L_i is the cell-size in the respective direction. $S_z = 50.26;\ S_y = 628.32;\ S_x = 6.8 \times 10^3$ (for all the units are in cm^{-1}).

An important aspect of such waves is that they have small wave-vectors along z-direction i.e., k_z is much smaller than k_x and k_y. Hence, for most of the dominant modes, resulting from the RF pumping, propagation takes place in the plane perpendicular to the

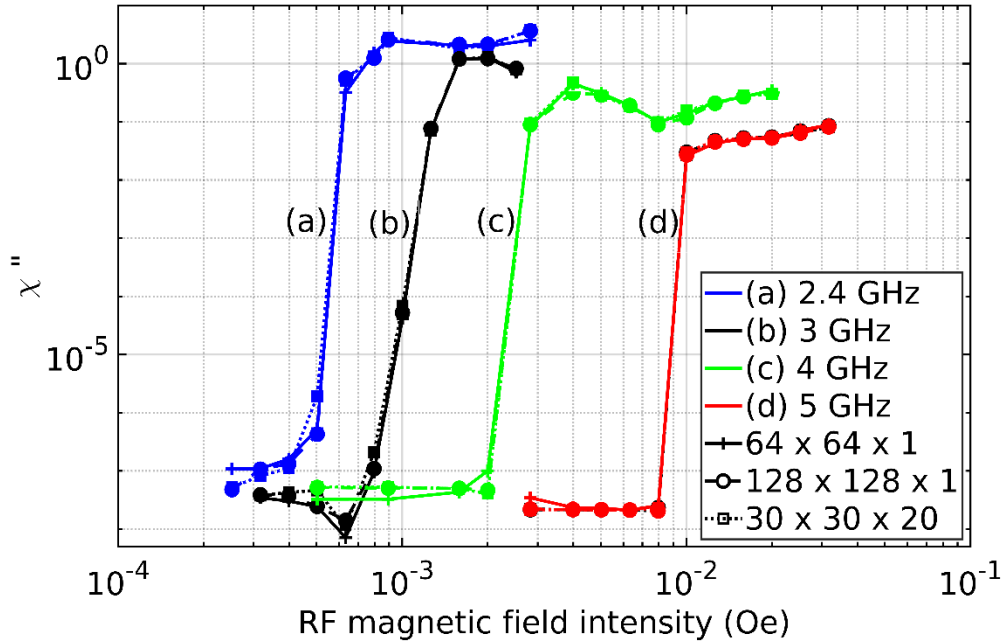

Fig. 4.1. Comparison of 3D and 2D models. 2D uses 64x64x1 and 128x128x1 grids, while the 3D model use 30x30x20 grids. Imaginary part of susceptibility (χ'') is plotted against the microwave magnetic field intensity. (Source: [112])

applied DC bias field ($\theta_k = 90°$, where θ_k is the angle between the direction of the bias field and $\vec{\boldsymbol{k}}$). This is in accordance with observations made experimentally [41], [140], [141]. Based on the data, we can employ a two-dimensional (2D) model to capture the essential physics that governs the behavior of such magnetic devices once the system enters the nonlinear regime under an applied RF field. The two directions of importance are the in-plane perpendicular to H_{dc} direction ($\hat{y}$) and the thickness direction ($\hat{x}$).

In Fig. 4.1, at low power levels, the spin-wave amplitude remains at a thermal level due to relaxation losses. At high power levels, the spin-wave amplitude increases exponentially, leading to increased absorption. More importantly, it can be seen that we can capture the device behavior using a system comprising of just 64x64x1 cells (2D system with 4096 cells) instead of a full-fledged 30x30x20 system (3D system with 18000 cells), i.e., leading to a reduction in the number of cells by a factor ~4.4. In this case, a system comprising 128x128x1 cells can be used to perform high-resolution studies specifically on the dominant modes. For a given gridding, this helps to discern more information about the modes that play a crucial role in nonlinear magnon scattering. Such a 2D model could hence help conserve hardware resources and simulation run-time.

A. Comparison to 3D Simulations

The susceptibilities calculated using 2D grids of 128 x 128 x 1 as well as 64 x 64 x 1 agree well with the 3D calculations for the same configurations (Fig. 4.1). Notice that we not only are able to obtain the same h_{th} within an acceptable degree of error but also a similar discontinuity at the onset of nonlinearity. A 128 x 128 x 1 takes approximately the same time (~9 hours on P100 GPU) as 30 x 30 x 20 grids, for a 300-ns run, due to similarity in the number of cells, while the 64 x 64 x 1 takes just ~3 hours on the same GPU for the same run. Furthermore, the reduced simulation also eases the stress on the number of cores and clock-speed available on the system, making such computations feasible even on sequential CPU-only systems, especially with regards to code run-times.

Both the 3D as well as 2D simulation schemes are independent of the specific nature of the device and, in principle, can be used to study any parallel-pumped

ferromagnet-based system. With respect to simulations, the cell sizes are chosen to be of the order of several micrometers for investigating the demagnetization dominated regime which best captures the susceptibility behavior of interest for such parallel pumped configurations (especially suitable for FSL design [137]). As far as the practicalities of simulation are concerned, the hardware used for computation often determines the choice of grids, in the sense that while a highly refined grid is desired for more accurate computations, it could substantially increase the simulation run-times. In many cases, there are strict limits specified by the available hardware systems w.r.t threads, arithmetic and control units (ALU), memory available, etc., preventing the use of denser gridding. A system employing 18000 cells takes 9 hours on an NVIDIA P100 GPU while 36000 increases the run time to a day, both for a 300-ns run. Code performance in conventional sequential computers (CPU-only systems) is even more drastically affected. 2D simulations developed here can be highly advantageous for both GPU-based and CPU-only machines in aiding the design of devices that need accuracy beyond that offered by simple analytic models.

4. 2 Thickness Dependence of Dispersion Relation

All computational results described in Chapter 2 were based on 3D simulations. Going forward, I make use of 2D simulations exclusively. At first, the thickness dependence of magnon dispersion relations is simulated.

One of the physical parameters that determine the spin-wave manifold or simply the dispersion relation is the thickness of the sample, *D*. The thickness, in addition to the

magnitude of absorption, also determines the bandwidth of operation. For an applied bias field of 100 Oe, we vary the thickness: 5 μm, 15 μm, 20 μm, and 50 μm. In Fig. 4. 2, we show the dependence of 2D dispersion relation on sample thickness for the cases above using micromagnetic simulations.

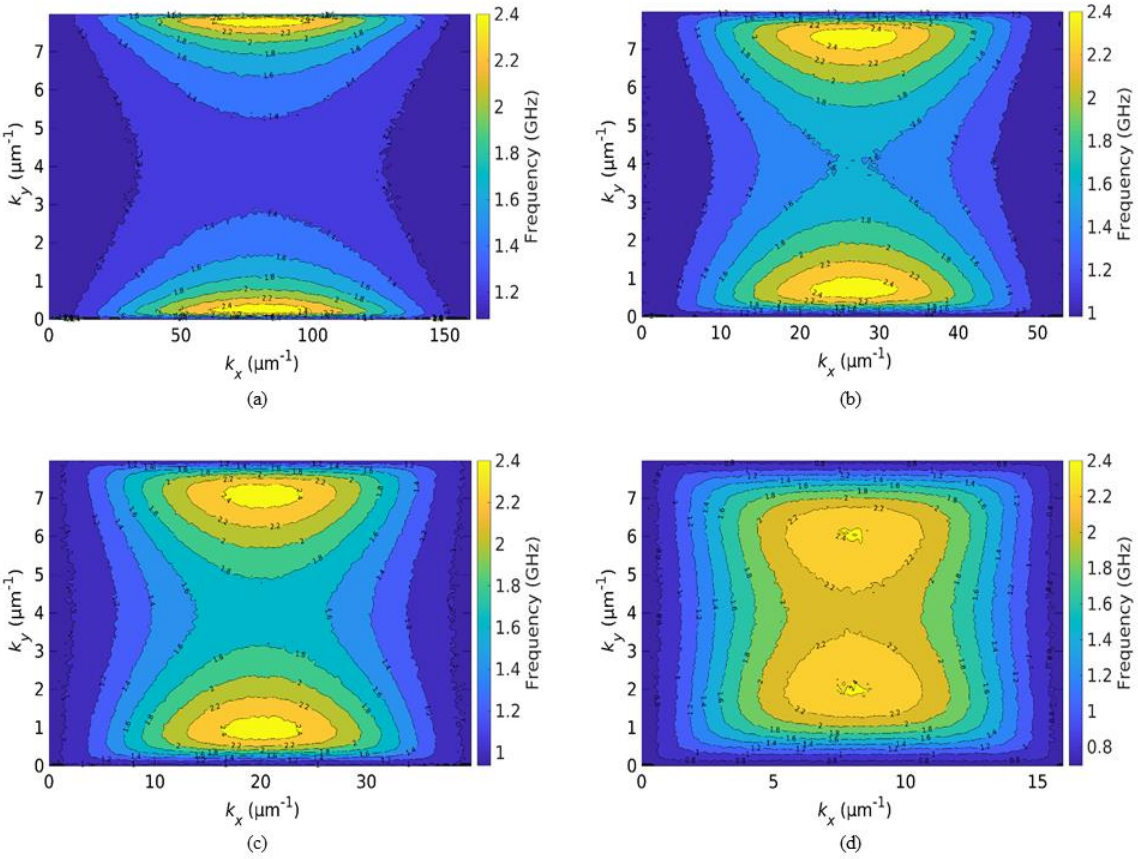

Fig. 4.2. 2D magnon dispersion relation for a bias field of 100 Oe for a sample of thickness (a) 5 μm (b) 15 μm (c) 20 μm and (d) 50 μm. (Source: [112])

4.3 Three and Four Magnon Scattering Processes

The response of the YIG material can be explained based on magnon dynamics taking place within the sample. As mentioned earlier, unless disallowed by the dispersion relation,

the most dominant scattering mechanism is the three-magnon process. In the case of a parallel pump, the energy associated with a microwave photon gets distributed between two magnons so as to conserve energy and wave-vector. It is this coupling mechanism that dissipates the RF energy in the magnetic material. In this section, we try to understand such processes from the perspective of the dispersion relation. The microwave field is turned on after relaxing the system (for ~300 ns). When the strength of the RF is above the threshold, it leads to a nonlinear response in the material. Fig. 4.3(a) shows the 2D

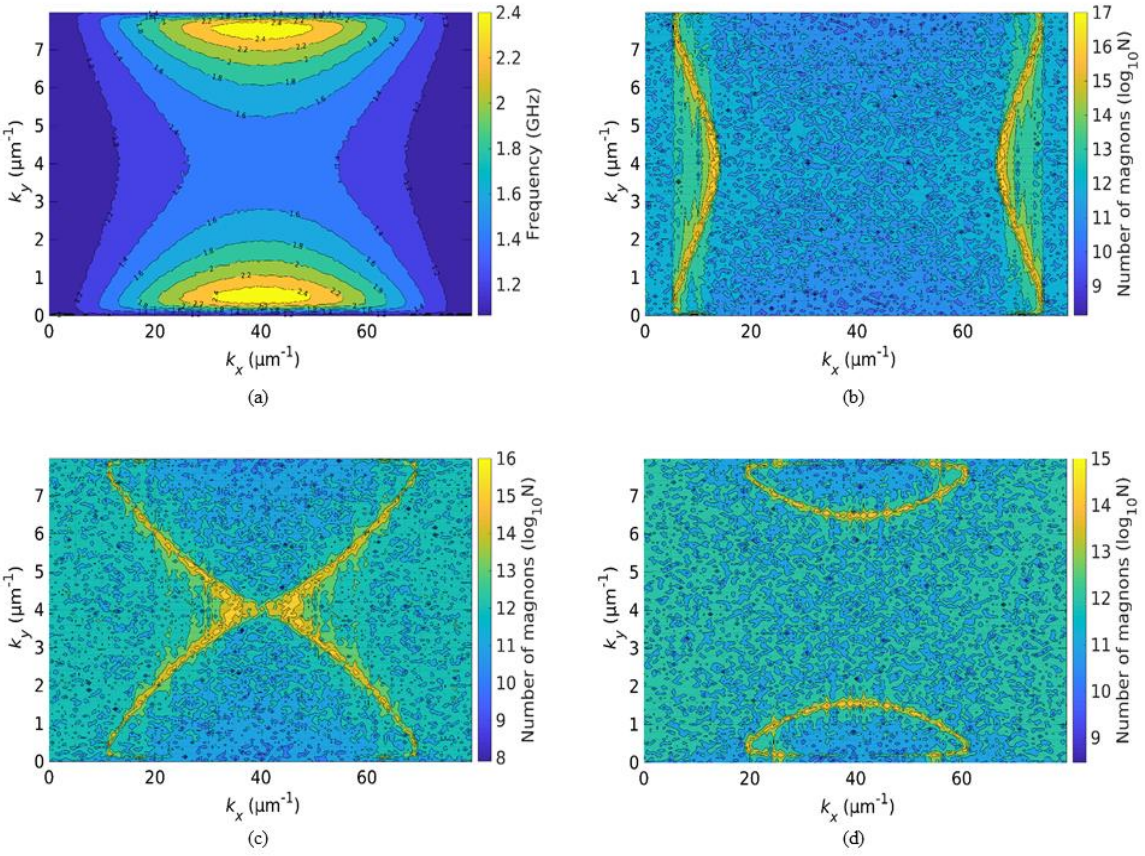

Fig. 4.3. (a) Dispersion relation of 128 x 128 x 1 cells for the system size 10 μm x 100 μm x 1250 μm. (b) Number (N) of magnons during the transient, when pumped with an RF signal of: (b) 2.4 GHz at -25 dBm with magnon number determined at 56 ns after RF field is turned on; (c) 3 GHz at -18 dBm with magnon number determined similarly at 71.5 ns; (d) 4 GHz at -8 dBm with magnon number evaluated at 61 ns. Note that modes showing large populations are close to the corresponding half frequencies. (Source: 112)

dispersion relation of the 10 μm sample obtained using a 128 x 128 x 1 grid for 10 μm $\times$ 100 μm $\times$ 1250 μm.

At first, we apply a pump frequency of 2.4 GHz at -25 dBm to the YIG sample. Note that this leads to the appearance of 1.2 GHz modes at the onset of nonlinearity: the magnon numbers (*N*) are plotted in Fig. 4.3(b). Similarly, 1.5 GHz modes (Fig. 4.3(c)) and 2.0 GHz modes (Fig. 4.3(d)) appear in the magnon number plot when the sample is pumped with 3.0 GHz (at -18 dBm) and 4.0 GHz (at -8 dBm) microwave frequencies, respectively.

Three magnon processes, however, are not always allowed. The lowest frequency on the dispersion relation is slightly above 1.0 GHz for a 10 μm sample at 100 Oe, and hence signals with frequency less than 2.0 GHz are disallowed from decaying via a three-particle process. When pumping at a frequency of 2 GHz, there is no nonlinearity till about $\sim 1 \times 10^{-2}$ Oe and the nonlinearity thereafter led to magnons with the same frequency as the pump signal, giving magnon distribution nearly identical to that in Fig. 4. 3(d) where 2 GHz modes appear. Note that this is a 4-particle scattering process where two photons at 2 GHz gave rise to two magnons at 2 GHz. This explains the behavior at 2 GHz in Fig. 3.2 (Chapter 3) and the resulting asymmetry w.r.t frequency detuning. The physics of both the three and four-particle processes was discussed in Chapter 3 (Section 3.2).

4.4 Experimental Comparison

In order to validate my findings in the previous sections, I determine the butterfly curve (plot of the microwave threshold-field vs. bias-field) and compare it with the parallel

pump results in [140]. A 0.5 mm wide 50 Ohm microstrip transmission line is used for the studies, with an applied pump frequency of 8.2 GHz. The YIG sample used is 5.1 μm thick.

For the simulations, we use a sample of size 5.1 μm x 100 μm x 1250 μm. A total of 16384 (128 x 128 x 1) cells, corresponding to the 2D simulation model, were used for the simulations.

Simulations were performed for 1500 ns with a time step of 50 fs on NVIDIA P5000 and P100 GPUs. Intrinsic damping (α) of 3×10^{-5} [142] along with an exchange constant of 3.77×10^{-7} $\frac{\text{ergs}}{\text{cm}}$ is used (the exchange field is implemented similar to [143]). The experimental data, along with the simulated data points are shown in Fig. 4.4.

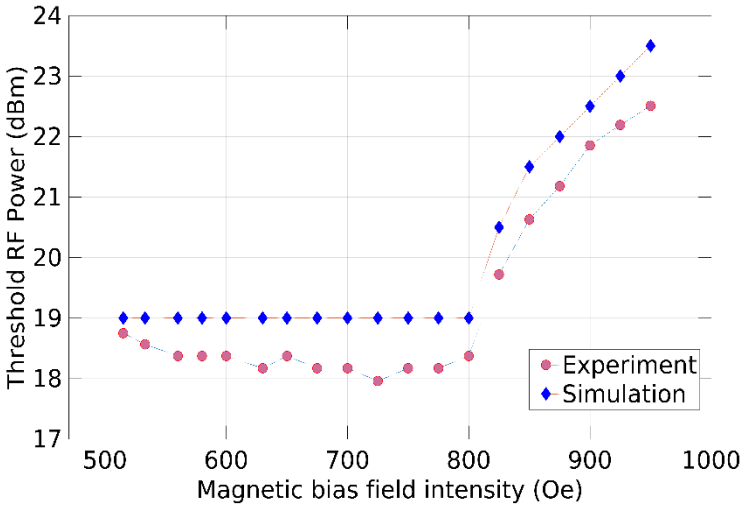

Fig. 4.4. Comparison of simulated threshold RF power with experimental data [140] for the butterfly curve for 5.1 um thick YIG sample in parallel configuration. Source: [112].

As can be seen from the figure, the simulated predictions for the microwave threshold field agree with the experiment within ~1 dBm. The discrepancies can be

attributed to non-intrinsic scattering mechanisms like 2-magnon scattering and the presence of inhomogeneities in the experimental sample [144], [145]. As noted earlier, the kink occurring around 800 Oe corresponds to the Kittel equation for 4.1 GHz (= $\frac{\omega_p}{2}$). The frequency of the dominant magnons is found to be 4.1 GHz in accordance with the 3-magnon scattering process. The agreement between the experiment and simulation results is remarkable, given that low power results are used to predict high power behavior without additional parameters. Furthermore, this agreement also demonstrates that 2D simulations could indeed capture the essential physics needed to explain the FSL functionality.

4.5 Conclusions

The physical processes described by the second quantization mathematical formalism discussed previously (Chapter 3) are now demonstrated using high-speed 2D simulation results. I have demonstrated that a 2D simulation (in the plane perpendicular to the magnetization) yields good agreement with a 3D simulation while being computationally more efficient than the 3D calculations. Good agreement between high power experimental and simulation results has been obtained for 3-magnon scattering using low power parameters over a wide range of bias fields without the use of additional fitting parameters. The computational ease of 2D simulations make the otherwise computationally unreasonable microwave-magnet simulations feasible on CPU-only machines as well. However, the 2D simulation technique developed in this chapter is specific for parallel pump studies. (2D simulations can also be used for studying perpendicular pumping [115])

I have demonstrated using micromagnetic simulations the two main *intrinsic* scattering mechanisms: three- and four-particle processes. If three magnon processes are allowed by the dispersion relation, the magnons that dominate are of half the pump frequency, else they have the same frequency as the pump signal, all provided the RF signal strength exceeds the necessary threshold.

Most importantly, the results demonstrate that micromagnetic simulations can play an important role in the understanding and, hence, in the design of magnetics-based nonlinear microwave devices. This is of special significance since, currently, the design of such devices is not based on physics-based deterministic rules but rather on phenomenological [1] and circuit-based analysis [146], which fail to account for accurate magnon physics. The simulation paradigm developed herein can, therefore, serve as an immensely useful modeling tool for magnet-based devices.

Chapter 5 Modulation-based Nonlinearity Suppression

In the previous chapters, parametric phenomena that govern the behavior of the magnetic material under microwave excitation were introduced and demonstrated. I also discussed the role of the threshold field in parametric processes. The threshold microwave field represents the strength of the microwave needed to initiate nonlinear processes. In linear applications, the knowledge of this field is essential to avoid the nonlinear regime by design. In contrast, nonlinear devices such as magnetics-based signal processing devices rely on nonlinearity to realize their functionalities, e.g., noise absorption. The dynamic controllability of the threshold field is, hence, of immense interest to a large number of applications. Traditionally, in order to change the threshold field, one would have to replace the magnetic sample with another that has a different thickness/geometry/material [147]. This is clearly inconvenient and represents a major disadvantage of magnetics-based nonlinear devices. Apart from device applications, fundamental physics explorations also need the ability to vary the threshold dynamically. For example, cavity-based studies in the past have often used multiple samples in order to achieve different nonlinear configurations for their investigations [9].

In this chapter, I discuss the dynamic control of threshold using a secondary microwave frequency. This technique allows in-situ control of nonlinearity and hence is of fundamental interest to a wide range of applications. The governing principle of the technique is explained analytically and demonstrated using simulations. The modified threshold field in the presence of the secondary microwave frequency is quantitatively

predicted. Fine structures, appearing in the threshold field upon variation in the frequency of the secondary frequency, have been demonstrated using simulations. Further, both the position and magnitude of such fine structures are also accurately explained. The impact of the magnon-phase is quantitatively determined. Finally, the dependence of the threshold field intensity on intrinsic damping and secondary microwave signal is discussed to aid practical device design considerations [116]. The results discovered in this chapter make strong contributions towards improving the parameters and expanding the functionality of magnetics-based electronic systems.

5.1Additional Excitation-based Modification of Parametric Instability

Parametric magnon-scattering processes have contributed immensely towards the understanding and exploration of the nonlinear processes involved in magnetic materials. A question of importance for fundamental and practical interests concerns the modification of the parametric resonance under pumping that is subjected to additional excitation(s). Parametric instability studies in the presence of noise have been considered in liquid crystals [34], electronic oscillators [32], [148] and in hydrodynamics [149]; the central theme underlying the variety of physics considered in these studies is the modification of some deterministic property by controlling the degrees of freedom present in the system using additional excitation(s). Magnetic systems have degrees of freedom by way of the numerous available magnon modes and hence present an interesting case for the study of parametric instability (magnon scattering) under the influence of additional excitations

and/or noise. Modulation-based suppression of nonlinearity in magnetics was first theoretically proposed by Suhl [150] and experimentally demonstrated by Hartwick, Peressini, and Weiss [151]. This theory was later improved by Morgenthaler [152]. Similar efforts were also undertaken by Zautkin [153] and reported in [110]. However, for sinusoidal modulation input, the theories mentioned above did not thoroughly address the frequency dependence. The aim of this chapter is to present a theory applicable to all values of the secondary frequency.

As mentioned earlier, depending on the application, the nonlinear scattering could be undesirable, e.g., cause of noise in spin-wave based computing [154] that makes use of specific spatial-temporal magnon modes, or it might be useful, e.g., microwave devices like FSLs, signal-to-noise ratio enhancers, etc., [1], [155] that depend on such nonlinearities for microwave absorption in order to achieve their functionalities. Proper understanding of the consequences of modification of the nonlinearity by additional excitations, hence, would be beneficial to improve the design and/or performance of a multitude of magnetic devices, in addition to revealing interesting physical phenomena.

5.2 Micromagnetic Simulation

A thin film of YIG is saturated using a bias field, $H_{dc} = 200\ Oe$, applied in the plane of the magnetic sample (along the z-axis). The sample thickness of 5.1 μm is measured along the x-direction. The microwave field is applied along the z-direction, parallel to H_{dc} (the parallel scheme of pumping). The sample schematic is shown in Fig. 5.1(a). We assume periodic boundary conditions for the sample. The sample dimensions

of $5.1\,\mu m \times 100\,\mu m \times 1250\,\mu m$ are discretized into 128 x 128 x 1 cells along the respective directions as done in the previous chapters. We employ the 2D simulation paradigm as described in Chapter 4 for this study.

Saturation magnetization, $M_S = 145\,emu/cm^3$, uniform exchange constant, $A_{ex} = 3.77 \times 10^{-7} ergs/cm$, gyromagnetic ratio, $\gamma = 1.76 \times 10^7 rad/(s\,Oe)$ and

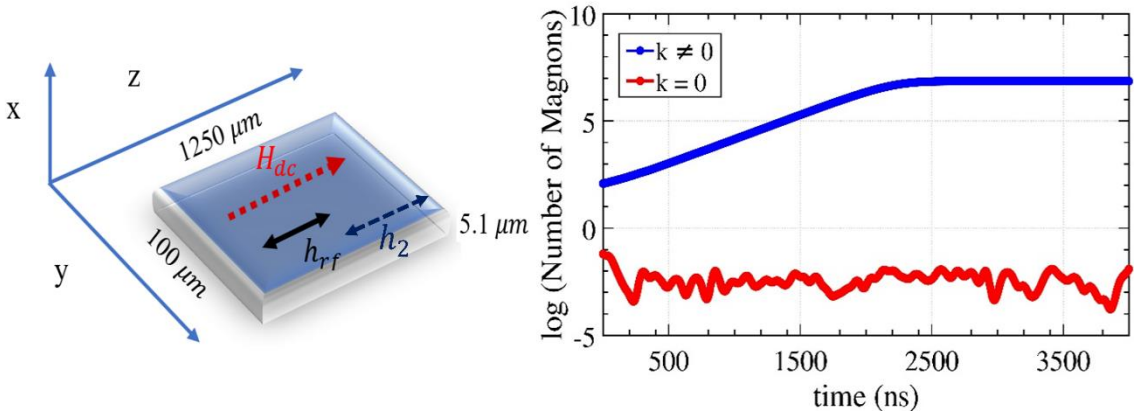

Fig. 5.1. (a) Parallel pump configuration with the secondary field (h_{rf2}). (b) Magnon growth (average) upon excitation close to the threshold illustrating the direct excitation of the k ≠ 0 modes. The pump frequency is 6 GHz and the excited magnons have a frequency of 3 GHz with k ≠ 0. (Source: [116])

realistic damping constant of 0.0007 (unless mentioned otherwise) are used for the sample. Demagnetization fields are computed using Newell's algorithm as before, and thermal fields are also taken into consideration in order to account for the thermal magnons at T = 300 K. The micromagnetic simulations were carried out using graphics processing units (GPUs) [93] at various supercomputing institutes -Minnesota Supercomputing Institute (MSI), San Diego Supercomputer Center (SDSC)'s *Comet* and Pittsburgh Supercomputing Center (PSC)'s *Bridges*.

5.3 Threshold Modification

The micromagnetic system relaxed under a bias-field of $H_{dc} = 200\,Oe$ is subjected to a microwave field of 6 GHz ($h_{rf} = h\cos(\omega_p t)$, with $\omega_p = 6\,GHz$). The Kittel frequency corresponding to 200 Oe being ~1.78 GHz, the microwave pump chosen amounts to an off-resonance parallel-pumping scheme with regards to the H_{dc}. Fig. 5.1(b) shows the magnon number growth at a microwave field-intensity, *h*, of 2.8 Oe, slightly above the threshold-field, h_{th}, 2.7 Oe. The dispersion relation and the pumping conditions are such that the absorption of microwave-photons creates parametric-magnons with half the energy of the pump-photon (3-particle process). Above the threshold field, there occurs

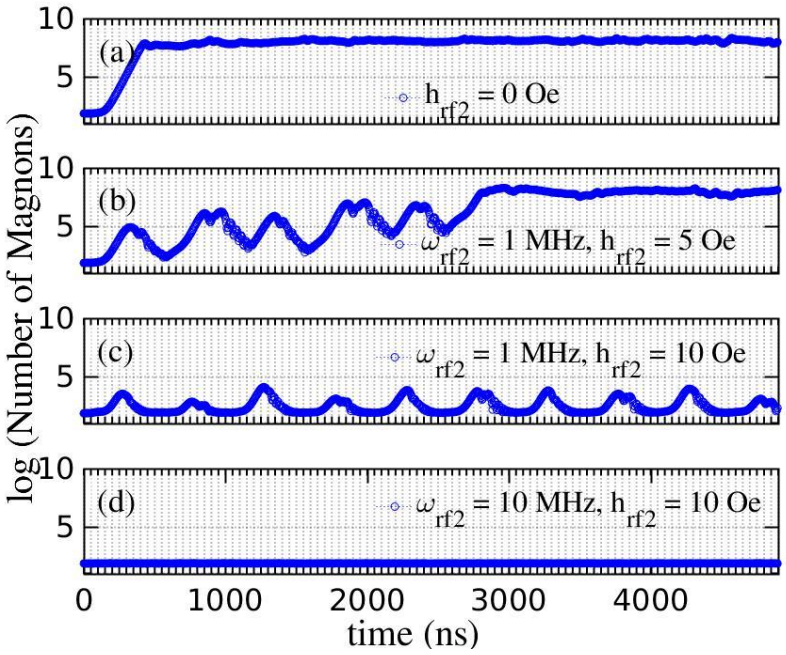

Fig. 5.2. Effect of secondary microwave signal on magnon number growth for a YIG sample with α =0.0007 and $H_{dc} = 200\,Oe$. The sample is subject to a microwave field of 6 GHz at a field-intensity of 6.1 Oe with (a) no secondary frequency (b) secondary frequency of 1 MHz at 5 Oe (c) secondary frequency of 1 MHz at 10 Oe (d) secondary frequency of 10 MHz at 10 Oe. (Source: [116])

an exponential increase mainly in the number of 3 GHz magnons; furthermore, momentum-resolved calculation of magnons demonstrates that direct excitation of the $k \neq 0$ magnons occurs while only a negligible excitation occurs for the magnons with $k = 0$. These observations are in accordance with previous discussions (Chapter 1 (Section 2.4)), [49], [41]. The dominant spin-wave mode has a wave-vector, $k \approx 1.975 \times 10^5\ rad/cm$. In this work, we use primary frequency field strengths close to the corresponding threshold values.

Next, I turn on an additional secondary signal which is linearly polarized parallel to the H_{dc}. It can be observed that in the presence of this signal, there is an overall reduction in the number of magnons, as shown in Fig. 5.2(b-d). A reduction in the number of magnons indicates a decrease in the nonlinear behavior. Secondary frequency and field-intensity-dependent modulation of the number of magnons could also be observed in Fig. 5.2. By increasing the strength of the secondary frequency, we can even completely quench the nonlinearity (Fig. 5.2(d)). These observations are in line with experiments in [151]. Next, we present a theory to explain the threshold field dependence over an arbitrary range of frequencies.

The threshold field, h_{th}, for a spin-wave of frequency ω_k can be expressed as [using 3.31, for simplicity h_{thg} is represented now as h_{th}]:

$$h_{th}^2 = \frac{\eta_k^2 + (\omega_k - \omega_p/2)^2}{V_k^2} \tag{5.1}$$

where ω_p is the angular frequency of the primary pump excitation, η_k is the relaxation rate of the magnons and V_k is the coupling factor between the photons from the primary-pump and the magnons. For $\omega_k = \omega_p/2$, the threshold-field would be simply η_k/V_k. Using this

along with the Eqn. (5.1), we can estimate the effective microwave intensity seen by the ω_k magnons (when excited with rf field of intensity h Oe) to be:

$$h_{eff} = h\left[\frac{\eta_k^2}{\eta_k^2+\left(\omega_k-\frac{\omega p}{2}\right)^2}\right]^{\frac{1}{2}} \tag{5.2}$$

The influence of the secondary excitation (of angular-frequency, ω_2 rad/s and field-intensity, h_2 Oe): $h_2\cos(\omega_2 t)$, can be interpreted as a change in the energy of the magnons:

$$\omega_k' = \omega_k + h_2\frac{\partial\omega}{\partial H}\cos(\omega_2 t) \tag{5.3}$$

The original magnon operator $b_k = b_0\exp(i\omega_k t)$ now becomes: $b_k' = b_k\exp\{i(\omega_k t + \frac{h_2\partial\omega}{\omega_2\partial H}\sin(\omega_2 t))\}$. Resonances would now be such that $\omega_p/2 = \omega_k'$. In other words, we can re-write the effective primary-field as seen by the magnons as: $h\,cos\{(2\omega_k t + 2\frac{h_2}{\omega_2}\frac{\partial\omega}{\partial H}\sin(\omega_2 t))\}$. In order to understand the spectral nature, we can express this periodic modulated wave using the complex representation of Fourier series that on further simplification, yields Bessel functions as the coefficients of expansion as shown in Eq. (5.4). Defining $\delta \triangleq |\omega_k - \omega_p/2|$, $\xi \triangleq 2\frac{h_2}{\omega_2}\frac{\partial\omega}{\partial H}$, and h_{th0} as the threshold-field intensity in the absence of the secondary signal, we can express the new threshold-field (h_{thn}) in terms of Bessel function coefficients as:

$$\left(\frac{h_{thn}}{h_{th0}}\right)^2 = [\sum_{n=-\infty}^{\infty} J_n^2(\xi).\frac{\eta_k^2}{\eta_k^2+\left(\delta-\frac{n\omega_2}{2}\right)^2}]^{-1} \tag{5.4}$$

This series with Bessel function coefficients can be physically interpreted to be exciting a multitude of magnon modes with different frequencies.

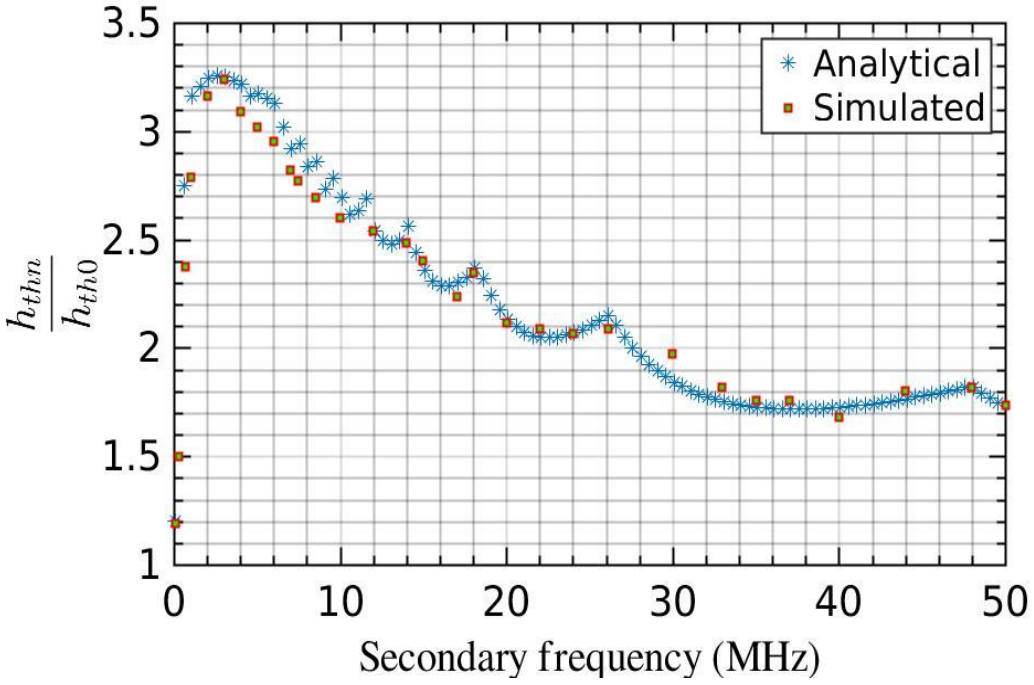

Fig. 5.3. Normalized threshold field for a 6 GHz microwave signal (h_{thn}, h_{th0} are threshold-field intensities in the presence and absence of the secondary, respectively) in the presence of 10 Oe of secondary frequency. It can be seen that the threshold field is maximum around 2.1 MHz. Magnon relaxation rate, η_k, of $1.0 \times 10^{-6}\ s$ and $\frac{\partial \omega}{\partial H} = 1.23\gamma$ are used for the analytical calculation. α =0.0007 is used in the simulations. (Source: [116])

Fig. 5.3 shows a normalized plot of the new threshold-field (h_{thn}) obtained under the influence of the secondary frequency. The analytical curve is obtained by minimizing the right-hand side of Eq. (5.3) using properly chosen δ. There exists an optimum frequency that lowers nonlinearity the most and consequently corresponds to the highest threshold-field intensity. This optimum frequency coincides with the longitudinal relaxation frequency $\eta_z (= 2\eta_k)$ of the magnetization. The decrease on either side can be considered to be due to the relatively slower overall decay of the magnons as the secondary

frequency moves away from the relaxation rate, η_z. At very high secondary frequencies, the ratio h_{thn}/h_{th0} tends to 1, indicating a relatively lower degree of mixing between the two frequencies. We estimated the relaxation rate of the longitudinal component of magnetization using [156]:

$$\tau = \frac{1}{\eta_z} = \frac{\hbar\omega_p \Delta M_z}{\gamma \hbar P} \tag{5.5}$$

where P is the power absorbed in the magnetic material, and ΔM_z the change in the longitudinal magnetization. Relaxation rate of the magnons, $\eta_k = 1.0 \times 10^6\ Hz$, is used to obtain the theoretical curve in Fig. 5.3 which predicts the relaxation rate of the longitudinal magnetization, $\eta_z (= 2\eta_k)$ to be $2.0 \times 10^6\ Hz$, that agrees well with the peak of the simulated data. A direct computation using the simulated data of Eq. (5.5) also yields $\eta_z = 2.1 \times 10^6\ Hz$, not unlike the expectations.

In Fig. 5.4, I have plotted the ratio of threshold field intensities as a function of the secondary frequency using Eq. (5.4). At a given secondary frequency, the threshold is determined in the case of simulated data by sweeping the primary field intensity. The secondary field intensity used is 10 Oe, and the system $\alpha = 0.00035$. It can be shown that the cusps correspond to change in the index of the dominant Bessel coefficient in Eq. (5.4); index n in Fig. 5.4 is such that the following holds:

$$\left(\frac{h_{thn}}{h_{th0}}\right)^2 = \min\left(\frac{1}{J_n^2(\xi)}\right) \tag{5.6}$$

where the function min() picks the minimum of the argument with respect to varying n. The index n at each secondary frequency that minimizes the function is plotted in Fig. 5.4. This demonstrates the role of higher-order Bessel functions in the stabilization process,

especially at smaller secondary frequencies; the coefficient of J_n^2 in (2) then determines the magnitude of the ratio.

It is, therefore, possible by controlling the frequency and strength of the secondary signal to completely extinguish the nonlinearity. This phenomenon, hence, allows the controllability of the nonlinear processes, which can be helpful for nonlinear applications. For example, it can be used to increase the power handling capability in RF devices, wherein it is desirable to reduce the nonlinear effects.

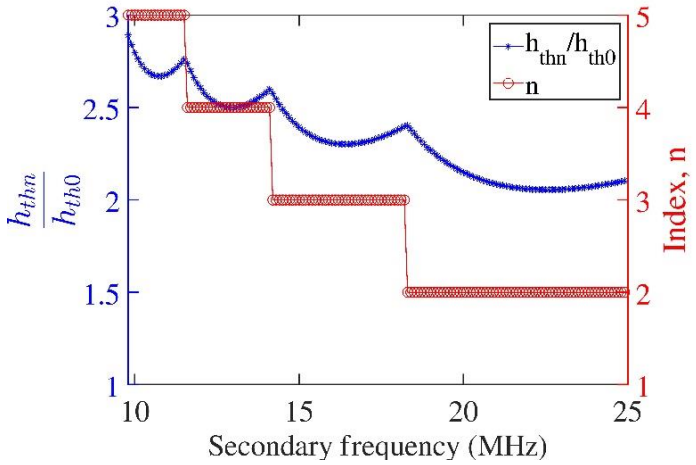

Fig. 5.4. Plot of the ratio of threshold field intensities in the presence (h_{thn}) and absence (h_{th0}) of the secondary signal with respect to secondary signal frequency. The theoretical (blue starred curve) is a plot Eq. (5.4) for 10 Oe of secondary signal for a magnetic sample with an intrinsic damping, $\alpha = 0.00035$. Red curve with circles shows the changes in the index n of the dominant Bessel coefficient, computed using Eq.(5.6). It can be seen that the change in n corresponds with the occurrence of cusps in the threshold ratio. (Source: [129])

5.4 Magnonic Loss Channels and Significance of Magnon Phase

The magnon-modes excited in the presence of the secondary differ from the original 3-GHz magnon-modes by multiples of half the secondary frequency, $f_2/2$, where $f_2 = \omega_2/2\pi$ (or in terms of m_z they differ from the 6 GHz spectral components by multiples of

the secondary frequency). This can be seen from Fig. 5.5, which is a frequency-spectrum plot of the average value of the longitudinal magnetization, m_z. The frequency-resolved magnon growth in the presence of the secondary excitation explicitly shows one such additional mode alongside the 3 GHz modes in Fig. 5.6(a). It can be seen that the dominant mode is 2.952 GHz as opposed to the original 3 GHz.

Further, as ξ decreases (or f_2 increases) fewer harmonics of the secondary frequency are relevant, consequently reducing the number of dominant magnon-modes. This can be seen in Fig. 5.5(c)-(d). Mathematically, this can be seen as a consequence of the decay of the Bessel functions with increasing ξ. Physically, this reflects the requirement of a higher number of modes as an increasingly smaller fraction of energy gets assigned to each of these modes with increasing ξ. This is required to ensure energy conservation during magnon excitation by the photons. At lower ξ, a few high amplitude modes carry most of the energy, while at higher ξ the energy is distributed across a larger number of components. By choosing ξ to correspond with zeros of $J_0(\xi)$ we can set the magnetic system such that no 3 GHz magnons are present and the microwave energy is carried instead entirely by the components: $3\ \mathrm{GHz} \pm n\omega_2/2$. It was observed, for example, at 12 MHz secondary frequency that the 3 GHz magnons remained close to the equilibrium values while 2.994 GHz modes are observed to be much higher in numbers.

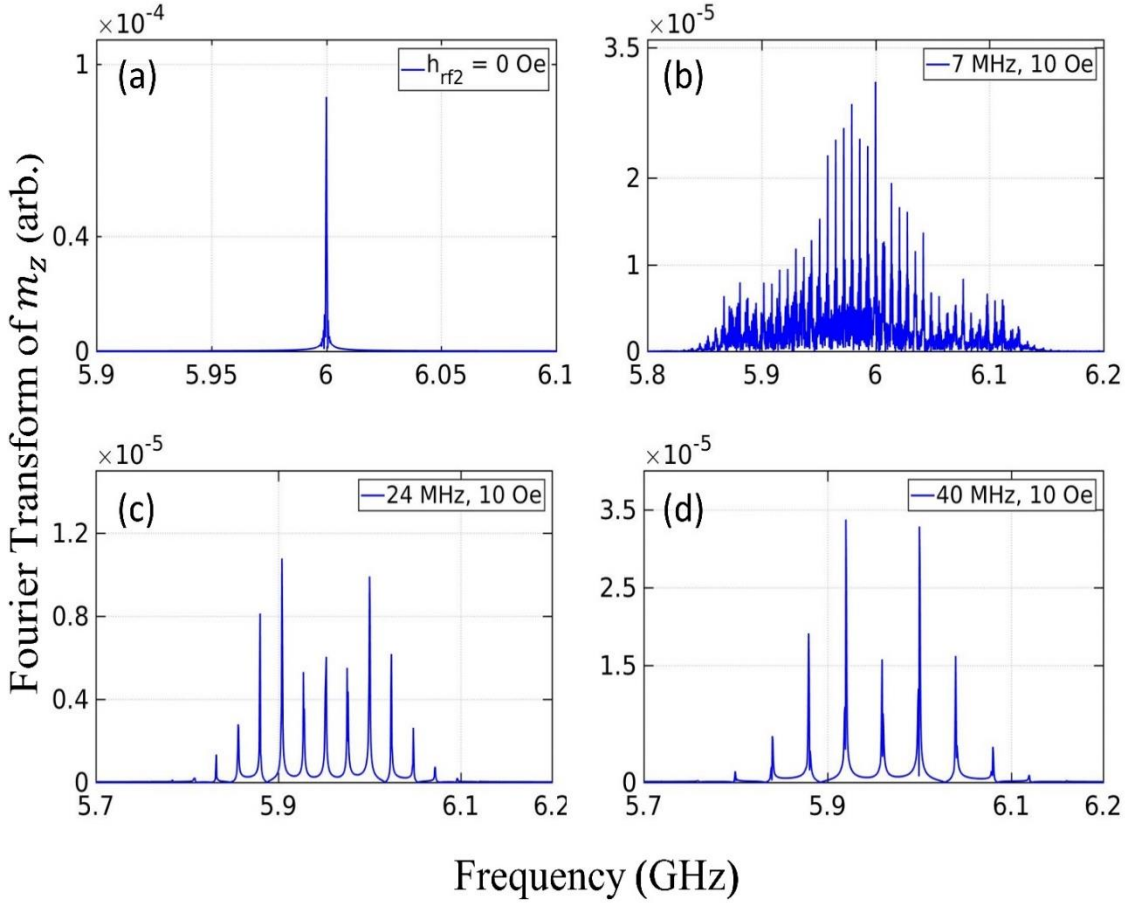

Fig. 5.5. Frequency spectrum of the z-component of magnetization under a primary excitation of 6 GHz with (a) no secondary frequency. 10 Oe secondary excitation of (b) 7 MHz (c) 24 MHz (d) 40 MHz; successive peaks differ by integer multiples of secondary frequency. Power leakage into other spin modes can be clearly seen. Also, the number of dominant peaks decreases as the secondary excitation frequency increases. α =0.0007 is used in the simulations. Source: [116].

It follows from Eq. (5.3), that the phase ψ_m of the magnons is $\xi \sin(\omega_2 t)$. The nature of threshold-field ratio in each cusp is governed by $sin(\psi_p - \psi_m)$ where ψ_p and ψ_m are the phase of the pump and the net magnon phase, respectively. For a constant pump-phase ψ_p, the quantity of interest becomes $\sin(\xi \sin(\omega_2 t))$, from which we can recover the Bessel-function pre-factors encountered earlier. Using, $\cos\{\omega_p t + \xi \sin(\omega_2 t)\} =$

$Re[e^{i\omega_p t}.e^{i\xi\sin(\omega_2 t)}]$, the Fourier series expansion ($\mathcal{F}$) of $e^{i\xi\sin(\omega_2 t)}$ can be written as: $\mathcal{F} = \sum_{n=-\infty}^{\infty} c_n\, e^{in\omega_2 t}$, with $c_n = \frac{1}{2\pi}\int e^{i(\xi\sin(x)-nx)}dx = J_n(\xi)$, where $x = \omega_2 t$.

This allows us to interpret the cusps seen earlier as consequences of the relative phase change between the primary RF and the dominant magnon modes. Within each cusp, the peaks in h_{thn}/h_{th0} occur for those frequencies that have the least favorable phase-match condition for coupling to magnons. This is demonstrated using simulations by the plot of

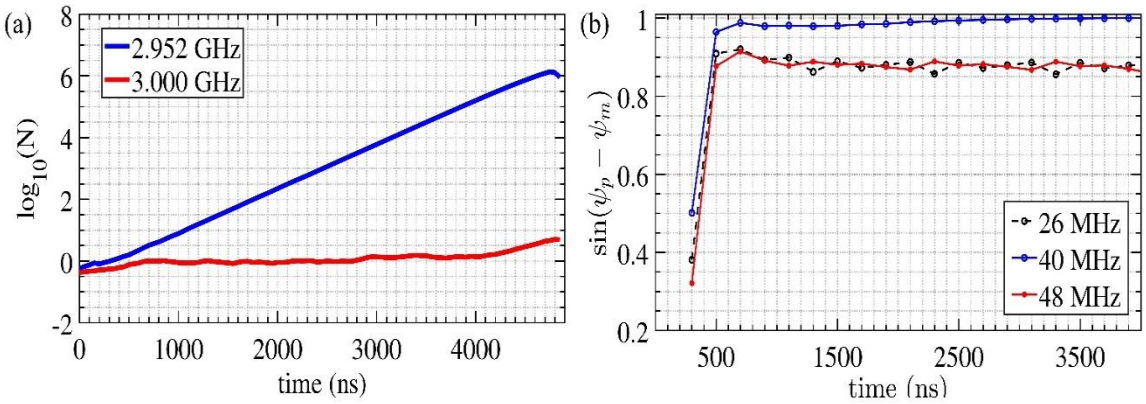

Fig. 5.6. (a) Magnon numbers resolved in frequency when a 6 GHz pump frequency is used at $H_{dc} = 200\ Oe$ for a YIG sample with α =0.0007. For a secondary signal at 24 MHz, one of the dominant modes is 2.952 GHz. In the absence of the secondary, the dominant mode is 3 GHz. (b) Magnon phase with respect to that of the pump is such that coupling is maximized at 40 MHz and minimized at 26 MHz and 48 MHz. The frequencies- 26 MHz and 48MHz correspond to the presence of cusps Fig. 5.3. (Source: [116])

sine values for different frequencies (Fig. 5.6(b)). The secondary frequency, hence, modulates the phase relationship between the dominant magnon modes and the microwave. In the absence of the secondary frequency, it is found that the sine of this phase difference is maximum for the dominant modes, which in our case are the 3 GHz modes (as observed in Fig. 5.1).

Megahertz modulation may develop in the magnetic system under parametric pumping without explicit secondary pumping. Auto-oscillation [110] and chaotic

phenomena [157] that can produce such MHz oscillations in the system make the low-frequency modulation effects worthy of consideration for magnonic applications. In addition, the cuspid features (of Fig. 5.3) might also need consideration during the robust design of magnonic devices, as they represent singularities in otherwise monotonous functional dependence between the threshold ratio and the secondary frequency.

Another interesting observation is that the slope of the growth rate of magnons with the primary field intensity remains nearly the same as the strength of the secondary excitation is varied (Fig. 5.7(a)), secondary frequency remaining the same. This indicates that the photon-magnon coupling efficiency $V_k sin(\psi_p - \psi_m)$ remains the same. Also

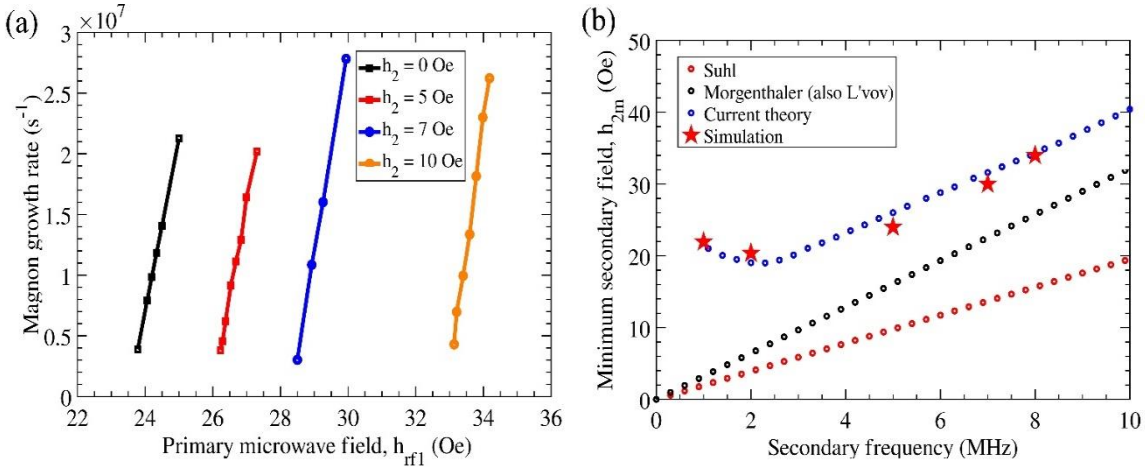

Fig. 5.7. (a) Growth rate of parametric magnons in the vicinity of the corresponding threshold under various secondary excitation field intensities when excited with 6 GHz microwave at 200 Oe. YIG sample with α =0.007 is used in this case. (b) Comparison of the minimum secondary-field intensity (h_{2m}) needed to suppress non-linear effects as predicted by: Suhl [150], Morgenthaler [152] (also, L'vov [110]), and current theory, for an $\frac{h_{thn}}{h_{th0}}$ ratio of 4 as per Eqs. (5.7), (5.8), and (5.4), respectively. (Source: [116])

noticeable is the increase in the threshold-field intensity. (The results of Fig. 5.7(a) are obtained using simulations that use intrinsic damping constant, $\alpha = 0.007$.)

5.5 Comparison with Previous Theories

Suppression of absorption by employing frequency modulation of microwave-field was initially suggested by Suhl [150] to follow:

$$\left(\frac{h_{thn}}{h_{th0}}\right)^2 = \frac{1}{J_0^2(\xi)} \tag{5.7}$$

This treatment was later enhanced by Morgenthaler [152] and in the work of L'vov [110]:

$$\left(\frac{h_{thn}}{h_{th0}}\right)^2 = \min\left(\frac{1}{J_n^2(\xi)}\right) \tag{5.8}$$

It can be shown that for a constant $\frac{h_{thn}}{h_{th0}}$ ratio, the above theories predict straight-line behavior for the minimum secondary field intensity (h_{2m}) needed to suppress nonlinear effects, down to zero Hz. In the current theory, however, below the relaxation rate, an increased h_{2m} is observed. The minimum value of h_2 that restricts the nonlinearity h_{2m}, for an $\frac{h_{thn}}{h_{th0}} = 4$, is compared in Fig. 5.7(b). This nonlinearity is in accordance with the experimental observations in [151].

5.6 Modulation Dependence on Intrinsic Damping and Secondary Signal Strength

While the previous sections gave advanced insights from a physics perspective, the physical parameters involved in the secondary frequency-based nonlinear suppression have not yet been investigated. Such investigations are vital from the perspective of engineering design. In this section, we discuss the dependence of the nonlinear behavior on parameters such as intrinsic damping and secondary signal strength. The intrinsic damping of magnetic

materials can vary from sample to sample, depending on the growth techniques and conditions. It, hence, constitutes an important parameter whose impacts need to be studied for any phenomena. The strength of the secondary signal is an external parameter that can be easily altered to control the nonlinearity.

A. Intrinsic Damping

The requirement of threshold field intensity arises due to the loss mechanisms that must be overcome before the 3-magnon interaction can lead to the growth of the magnons. Even in a defect-free and ordered magnetic system, there can be mechanisms that lead to the energy introduced into the magnetic system (say by microwave pumping) to ultimately dissipate into the lattice. An important parameter in this context is the phenomenologically introduced damping constant (α), which determines the rate of energy loss from the magnetic system. As the name suggests, α plays the important role of dampening out the spin-wave modes and, thus, has an essential role in the magnon-based nonlinear properties.

From a practical viewpoint, different samples of the magnetic materials may have different α depending on the growth techniques and conditions. In order to understand its effect on h_{th0}, we provide Table. 5.1, from which it can be seen that it varies directly with the damping constant, i.e., $h_{th0} \propto \eta_k$, where η_k is the relaxation rate of the magnetic system [112]. Under similar pumping conditions with just the damping constant varying, we have $\eta_k \propto \alpha$.

Intrinsic damping, α	h_{th0} (Oe)	h_{th0} $/(h_{th0}$ @ 0.0007)	$\alpha/0.0007$
0.00035	1.4	0.52	0.5
0.00070	2.7	1.0	1.0
0.00175	6.3	2.3	2.5
0.007	25	9.3	10

Table. 5.1. Dependence of threshold field intensity, h_{th0} on the intrinsic damping constant, α. Source [129].

The role of α, however, extends beyond the simple threshold-field control when the additional signal is applied. The α, controls the secondary frequency, f_m, at which the maxima of the threshold-field ratio occurs. This is demonstrated using simulations in Fig 5.8. Firstly, for α = 0.0007 the $f_m = 2.1$ MHz, and when it is changed to 0.00035 ($= \alpha/2$) and 0.00175 ($= 2.5\alpha$), we observe the corresponding f_m to be ~1.0 MHz and ~5.0 MHz, respectively. Thus, in all the cases f_m scales linearly with α, and $f_m = \eta_z$. Secondly, a lower α is seen to result in a larger fractional increase in the threshold. The increase in the threshold, in general, is attributed to the creation of additional magnons. The energy that entered the magnon mode ω_k, in the presence of the secondary signal gets distributed to neighboring frequencies $\omega_k \pm n\omega_s/2$, where n is an integer. The reduction in damping makes easier the creation of additional magnons (i.e., $\omega_k \pm n\omega_s/2$ magnons with $n \neq 0$). These additional magnons can hence be seen as loss channels that divert the energy away from the ω_k-mode. As observable in Fig. 5.8, the reduction in damping leads to an increase in the threshold ratio. Mathematically, this is a consequence of the growing importance of the higher-order Bessel functions (i.e., those with higher n) as ξ approaches 0 (i.e., as the secondary frequency decreases).

In short, microwave energy now gets channeled into multiple neighboring magnon modes much more likely due to the increased lifetime (or higher stability) of these modes. For the same reason, it is also observed that the number of cusps has also increased with decreasing α. It can also be observed that with the change in α, it is the behavior at the lower secondary frequencies that is most affected, while the threshold at higher frequencies is relatively unchanged. It is important to note that while intentional changes in damping can be used to effect changes in the threshold field intensity, the inadvertent modification of other magnetic properties, e.g., M_S, stochiometry, etc., may lead to unexpected effects.

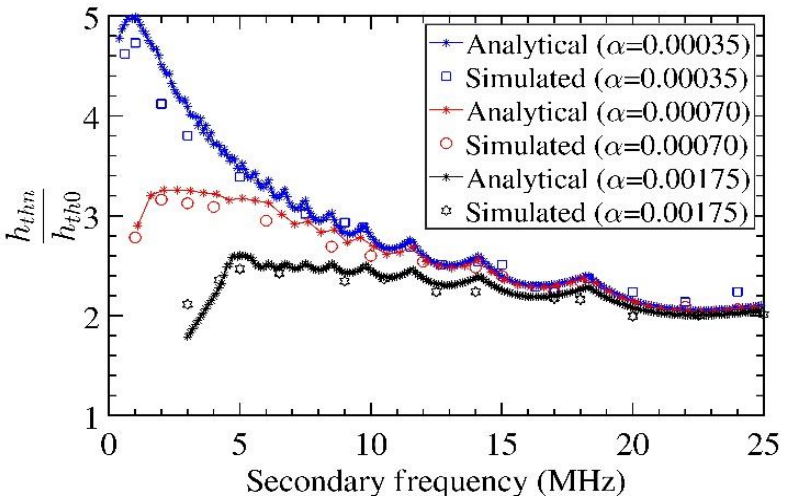

Fig. 5.8. Dependence of the normalized threshold-field intensity on intrinsic damping constant, α, as a function of the frequency of the secondary signal. The symbols represent micromagnetically simulated data and the lines are from Eq. (5.4). For all the plots $h_s = 10\ Oe$. (Source: [129])

B. Secondary Signal field intensity

The secondary signal plays a crucial role in altering the nonlinear phenomena as well; dynamic control of the nonlinear properties that can be important from an application perspective can be effected through the secondary microwave signal.

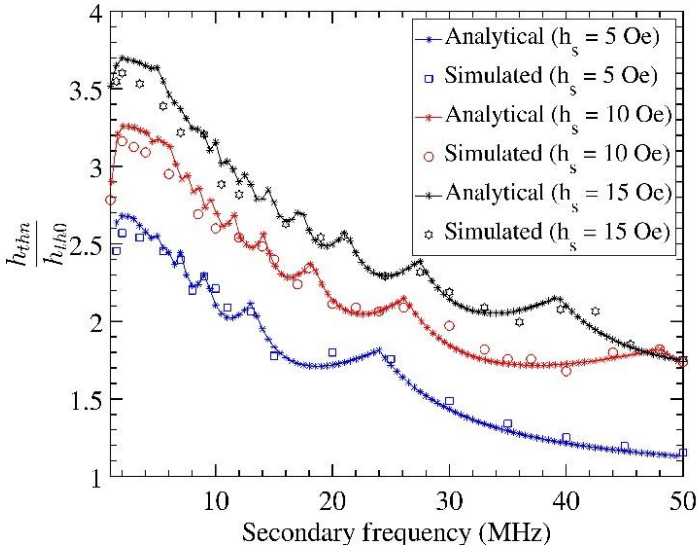

Fig. 5.9. Variation of the threshold-field intensity with different secondary microwave strength as a function of the frequency of the secondary signal. The symbols represent micromagnetically simulated data and the lines represent Eq. (5.4). For all the plots $\alpha = 0.0007$. (Source: [129])

In this context, we first discuss the role of the secondary signal intensity, h_2. In Fig. 5.9, we plot the suppression curves for various h_2 (h_2 is represented by h_s in Fig.5.9); it can be observed that the threshold field increases with an increase in secondary field intensity. No significant changes in f_m are observed. Also, it can be seen that the curves display a larger number of oscillations for higher h_2. The impact of the secondary signal is to modulate the dispersion relation of the magnons, which can be seen from the argument of the Bessel function: $\xi = \frac{2}{\omega_2}\left(h_2 \frac{\partial \omega_k}{\partial H}\right)$, as discussed earlier. Higher h_2, therefore, makes it increasingly difficult for the magnons to respond to the primary microwave signal by sweeping their instantaneous frequencies (as per $h\cos\{\omega_p t + \xi \sin(\omega_2 t)\}$). No magnons would satisfy the necessary frequency condition for long enough to allow non-trivial increase in its numbers, and this results in increased threshold field values with an increase

in h_2. This can, hence, also be interpreted to be due to an increased phase-mismatch between the pumping microwave signal and the dominant spin-wave mode.

The qualitative and quantitative agreement in Fig. 5.8 and Fig. 5.9 over both the field intensity and the frequency of the secondary signal indicates the robustness and suitability of the analytical theory and micromagnetics-based simulation techniques towards device design. (The lower density of datapoints is due to the computationally expensive nature of the simulations.)

5.7 Conclusions

The key consideration in many of the magnon-based applications is often controllable nonlinearity, compared to the situation, for example, in magnetic storage applications where the complete switching of the magnetization – a highly nonlinear process - is desired. Magnon-based applications require lower degrees of nonlinearities, which can be controlled to bring about deterministic changes in the input signal without inducing switching of the magnetic material [34, 71, 110, 152, 153, 154]. An important consideration in such cases is the feasibility of *dynamic* control of the nonlinear behavior. In this chapter, I illustrated a technique to achieve the dynamic control of the nonlinear behavior of ferri(ferro)magnets under microwave excitation using an additional microwave signal.

Secondary signal-based nonlinear control: Specifically, I have shown that a secondary excitation with a frequency close to the longitudinal relaxation rate (η_z) causes the most significant increase of the nonlinearity threshold. It is shown that the phase

decorrelation of the magnons at frequencies above η_z, gives rise to oscillatory features in the threshold-field intensity as the secondary frequency is varied. Magnon modes differing in frequency from that of the usually excited dominant mode by multiples of half of secondary frequency ($\omega_2/2$) are found to dominate in the presence of the secondary signal (with frequency, ω_2). Further, it is observed that with variation in the field intensity of the secondary excitation (h_2), the rate of change of magnon growth rate remains the same. However, with an increase in h_2, the threshold-field increases.

Significance of damping constant: The role of damping, in general, in nonlinear modulation was discussed. It is shown that the threshold field is proportional to the intrinsic damping, α. The α also plays an important role in threshold modification in the presence of a secondary microwave signal through the longitudinal relaxation rate, η_z. Ferrites, e.g., YIG, are often employed in RF applications due to their low damping, which allows higher magnon lifetimes, thereby leading to an increased likelihood of microwave-magnon interaction.

Significance of magnon-phase: Magnon-phase has long been a less understood and studied parameter. The crucial role of magnon-phase in nonlinear interactions, as demonstrated in this chapter, illustrates its significance in physical processes and hence also in potential applications. From this study, we can surmise that the magnon-phase-based phenomena are important considerations for a myriad of potential applications that propose to make use of the nonlinearity for information processing, encoding, or transmission [6].

The intensity and frequency of the secondary microwave provide external methods of dynamic threshold control. While additional circuitry may be needed to handle the secondary signal, its frequency as required for nonlinear control is orders of magnitude lower than the frequency of the primary signal. The potential of using a low-frequency secondary signal (~MHz) to modify magnon dynamics produced by a microwave field (~GHz) can be appealing to many engineering applications that require a dynamic control of nonlinearity. In the study, I have additionally demonstrated that general higher-order magnonic processes can indeed be captured and studied using micromagnetics.

Compared to a system with low degrees of freedom, e.g., electronic oscillator, the higher number of magnon modes (degrees of freedom) allowed in the magnetic material can lead to increased possibilities by which noise signals can interact with the material. In the current study, I considered a single deterministic additional signal that resulted in interesting interactions amongst various magnon modes. More elaborate noise sources could therefore present a wide variety of magnonic phenomena in these materials. In the next chapter, I will demonstrate the impact of magnon-phase-noise on nonlinear processes.

Chapter 6: Effective Phase Noise Considerations

In the last chapter, I demonstrated the significance of magnon-phase in parametric processes. Despite the crucial role of magnon-phase, the general qualitative and quantitative consequences of phase-noise on nonlinear properties remain far from understood. In this chapter, using analytical techniques usually employed in hydrodynamics, I explore the direct impact of phase-noise on nonlinearity. The analytical theory is then compared with simulated data from micromagnetics to understand the effects of phase-noise in nonlinear phenomena. Specifically, the behavior of the threshold field and growth rate of the magnons in the presence of Gaussian phase-noise is predicted [173].

6.1 Magnon-Phase: An Overview

Apart from the obvious interest from a fundamental physics perspective due to its direct involvement in nonlinear properties, the phase is also significant from a practical viewpoint, more so as the magnon-based devices become increasingly miniaturized. In fact, a myriad of applications that rely *directly* on the magnon phase have been proposed in the recent past. The magnon-based paradigm of applications -*magnonics*- has emerged as one of the promising candidates for information transfer and data-processing technology, with the magnon phase playing an important role in notable *novel applications* like spintronic applications, e.g., spin torque oscillators (STO) [72], spin-wave conduits for interconnects [7], spin-wave-based logic circuits [6], [68], [158], and spin-wave lens [70], etc. to name a few.

Devices used in *conventional applications* like telecommunication, radar, etc., for

example, magnetics-based FSLs, Signal to Noise ratio Enhancers (SNEs), phase shifters, etc. [2, 18] that rely on the nonlinear absorption of microwave signals are invariably affected by the magnon phase. Often working in noisy radio-frequency (RF) environments, these devices have to process/reject noisy signals impinging on them. However, magnon phase-noise is rarely given any consideration in the design of such applications, and noise studies are often at the circuit level and phenomenological in approach [146]. However, as the demand for miniaturization grows, magnon phase-based nonlinear aspects and thereby the phase-noise itself will have increasingly significant roles to play.

A. Phase-noise Sources

Phase noise has multiple sources; while the traditional magnet-based RF devices that operate in high-noise environments are likely to encounter temporal phase-noise, newer magnonics applications employing smaller volumes of magnetic materials are also likely to be affected by process variations that result in spatial phase-noise. Effective spatial phase-noise in parametric processes may be attributed collectively to the presence of inhomogeneities, local impurities [26], [159], domains [160]-[163], etc. In addition, the process of generation of the input microwave/spin-polarized current and the process of amplification of spin-waves can add temporal phase-noise into the magnetic system. Apart from the external sources, the distribution of $\boldsymbol{k}$-vectors, that is unavoidable owing to the nonlinear nature of microwave excitation. can lead to potential decoherence of spin waves intrinsically [164]. However, this is usually neglected in nonlinear studies [51], [54,] and often, assumptions of a single dominant mode are made.

Studies of noise in the past are largely based on thermal noise where phase noise is often considered only in terms of macro-spin models and as a by-product of thermal-noise in the context of specific applications, e.g., STO [165]-[171]. A direct study of the phase-noise is, hence, timely. In this work, we present a more general and fundamental treatment of the consequences of phase noise, which is applicable across multiple magnon-based nonlinear applications. We verify the analytic conclusions from our studies with GPU-based micromagnetic simulations that allow the phase to be directly accessed, manipulated, and analyzed.

6.2 Consequences of Phase-noise

A. Analytical theory

In this section, I develop a theory for understanding the consequences of phase-noise, specifically on the threshold field and the growth rate of magnons. While the former determines the beginning of nonlinearity, the latter controls the transient response and hence the response time of the magnetic sample to external microwave excitation.

A.1. Magnon growth

A parallel-pump based microwave-excitation configuration is used wherein both the DC magnetic field and the microwave pump signal, $hcos(\omega_p t)$ (microwave field intensity, $h_{rf} = h$ and ω_p is the angular pump frequency), are applied parallel to each other. The set-up schematic is shown in Fig. 5.1(a). As noted in Chapter 3, when the strength of the microwave field intensity exceeds a certain threshold ($h = h_{th}$), nonlinear

processes are initiated in the magnetic material wherein magnons are excited due to the absorption of photons. In our case, it is the three-particle scattering process that leads to the selective growth of the magnons. To understand the magnon growth process analytically, we start with the Landau-Lifshitz equation (Eqn. 3.1):

$$\frac{d\vec{M}}{dt} = -\gamma[M \times H] \tag{6.1}$$

Where, *H* is the effective magnetic field, and *M* is the magnetization vector. We can write, using Eq. 3.25 (Chapter 3), the equation of motion for magnetization in terms of magnon operators:

$$\frac{db_k}{dt} - i\omega_k b_k = -ihV_k b_{-k}^* \cos(\omega_p t) \tag{6.2}$$

V_k ($\equiv 2\mu_k\lambda_k\gamma$) is the coupling factor between the microwave and the dominant magnon mode. Note that Eq. (6.1) ignores the phenomenological damping that is usually added to the Landau-Lifshitz equation to account for the losses. We introduce to the microwave-phase a Gaussian temporal phase-noise, $\tilde{\phi}$ of zero-mean and standard deviation, σ:

$$\frac{db_k}{dt} = i\omega_k b_k - ihV_k b_{-k}^* \cos(\omega_p t + \tilde{\phi}) \tag{6.3}$$

A.2 Method of scales

Next, we use the method of scales [26] to gain insights into the equation of dynamics (Eq. (6.3)). We start by making the following definitions: $\delta \equiv |\omega_k - \frac{\omega_p}{2}|$ such that, $\delta \equiv \epsilon\Delta$ and $T \equiv \epsilon t$, where δ represents the detuning of the dominant spin-wave frequency from half the pump-frequency and *T* represents a smaller time-scale that would be useful in obtaining the amplitude equation of the magnon mode; ϵ represents a small parameter ($\epsilon \ll 1$). Also, under normal pumping conditions, $hV_k \ll \omega_k, \omega_p$ so that we can

define $hV_k \equiv \epsilon\, \omega_p F$, such that F is proportional to the input excitation.

In view of the above definitions, we have $\frac{d}{dt} = \frac{\partial}{\partial t} + \epsilon \frac{\partial}{\partial T}$. We make an ansatz that b_k has the following perturbation expansion:

$$b_k = u_0(t,T) + \epsilon u_1(t,T) + \cdots \tag{6.4}$$

wherein, u_1, can be interpreted as a higher harmonic correction to the principal term, u_0. We can write up to order ϵ^1:

$$\frac{db_k}{dt} = \frac{\partial u_0}{\partial t} + \epsilon \left(\frac{\partial u_0}{\partial T} + \frac{\partial u_1}{\partial t}\right) \tag{6.5}$$

The right-hand side of Eq. (6.2), evaluates to:

$$\frac{db_k}{dt} = i\frac{\omega_p}{2} u_0 + \epsilon \left(i\frac{\omega_p}{2} u_1 + i\Delta u_0 - i\omega_p F u_0^* \cos\left(\omega_p t + \tilde{\phi}\right)\right) + O(\epsilon^2) \tag{6.6}$$

Using Eqs. (6.5) and (6.6) above, the equation of u_0: $\frac{\partial u_0}{\partial t} - i\frac{\omega_p}{2} u_0 = 0$ or $\mathcal{L}.u_0 = 0$ where $\mathcal{L} \equiv \left(\frac{\partial}{\partial t} - i\frac{\omega_p}{2}\right)$, has a plane-wave solution:

$$u_0(t,T) = A(T) e^{i\frac{\omega_p}{2}t} \tag{6.7}$$

with *A(T)* being the complex amplitude of u_0. At the next order ϵ^1, we have

$$\mathcal{L}.u_1 = -\frac{\partial u_0}{\partial t} + i\Delta u_0 - i\omega_p\, F u_0^* \cos\left(\omega_p t + \tilde{\phi}\right) \tag{6.8}$$

Using Eq. (6.7) above, we have Eq. (6.8) as:

$$\mathcal{L}.u_1 = \left[-\frac{dA(T)}{dT} + i\Delta\mathrm{A(T)} - i\frac{\omega_p}{2} F A^*(T) < e^{\tilde{\phi}} >\right] e^{i\frac{\omega_p}{2}t} - \left[-i\frac{\omega_p}{2} F A^*(T) < e^{\tilde{\phi}} >\right] e^{-i\frac{3\omega_p}{2}t} \tag{6.9}$$

Note that $e^{i\frac{\omega_p}{2}t}$ is a solution of the homogeneous equation: $\mathcal{L}.u_1 = 0$. Therefore, if in (6.9),

$e^{i\frac{\omega_p}{2}t}$ has non-zero coefficients, it would lead to solutions of $u_1(t,T)$ that are secular in *t*, which would eventually diverge, leading to u_1 exceeding u_0. We avoid the secularity by suppressing the resonant term [172], i.e., by requiring that $A(T)$ satisfies the following:

$$-\frac{dA(T)}{dT} + i\Delta \mathrm{A(T)} - i\frac{\omega_p}{2}FA^*(T) < e^{\tilde{\phi}} >= 0 \tag{6.10}$$

Finally, using the property of Gaussian functions $< e^{\tilde{\phi}} > = e^{-\frac{\sigma^2}{2}}$, we have the amplitude equation:

$$\frac{dA(T)}{dT} = (\Gamma + i\Delta)\mathrm{A(T)} - i\frac{\omega_p}{2}FA^*(T)e^{-\frac{\sigma^2}{2}} \tag{6.11}$$

Since $h \propto F$, this implies $h_{thn} \propto h_{th0}e^{\frac{\sigma^2}{2}}$, where h_{th0} and h_{thn} represent the threshold field intensities in the absence and presence of phase-noise, respectively. In Eq. (6.11), Γ is a phenomenological loss parameter. Hence, as far as the nonlinear behavior is concerned, in the presence of a temporal Gaussian phase-noise, the threshold-field depends exponentially on the noise variance. Another important result is the dependence of the slope of the growth rate (g_r) w.r.t the microwave intensity (h). It is deducible using Eq. (6.11) that $\frac{dg_{rn}}{dh} = \frac{dg_{r0}}{dh}e^{-\frac{\sigma^2}{2}}$. While the threshold is an important parameter, especially for conventional applications, as discussed earlier, the growth rate plays a crucial role in the transient-state dynamics.

B. Simulation Results and Discussions

The simulations employed a parallel pump configuration, as discussed earlier; the geometry, discretization, and other conditions were the same as in Chapter 5, with bias

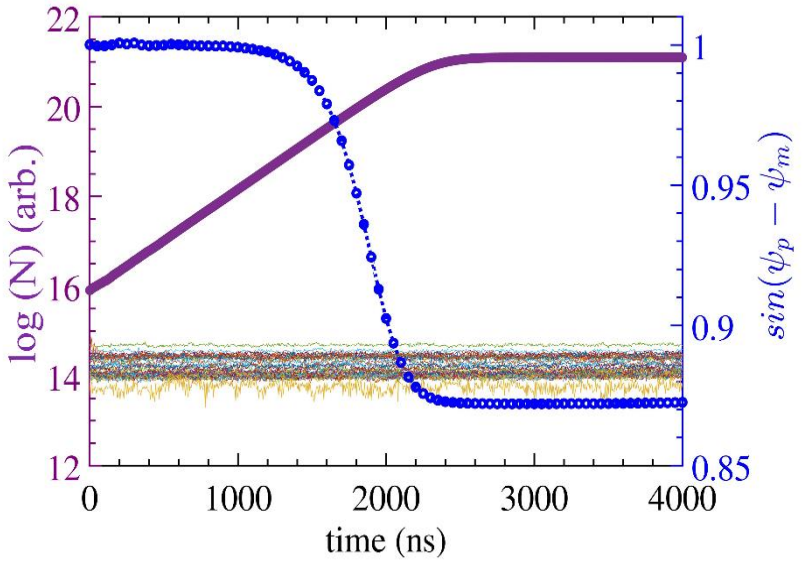

Fig. 6.1. Number of magnons, N, resolved in frequency for a pump-frequency of 6 *GHz* at 2.8 *Oe* and a bias-field of 200 *Oe*. ψ_p and ψ_m are the phases of the microwave pump and the dominant magnon mode, respectively. An exponential rise in numbers occurs only for magnons with frequency, $\frac{\omega_k}{2\pi} = 3GHz$, i.e., half the pump frequency while the other magnons with $\frac{\omega_k}{2\pi} \neq 3GHz$ remain close to their thermal equilibrium numbers. (Source: [173])

field of $H_{d.c} = 200\ Oe$, microwave pump frequency of $\frac{\omega_p}{2\pi} = 6$ GHz and damping constant $\alpha = 0.0007$. The simulation conditions are such that the 3-magnon scattering dominates. Fig. 6.1 illustrates the exponential growth of 3 GHz magnons for pumping slightly above the microwave threshold-field for a pump frequency of 6 GHz and a bias-field of 200 Oe. This growth eventually saturates due to the phase-mismatch between the photons and the magnons. The phase-match, $\sin(\psi_p - \psi_m)$, between the dominant magnon phase, ψ_m, and the pump microwave phase, ψ_p, controls the energy transferred from the microwave to the magnons. However, 4-magnon interactions amongst the exponentially growing 3 GHz magnons can cause $\sin(\psi_p - \psi_m)$ to differ from 1, reducing the coupling and eventually

resulting in magnon growth saturation [110]. (Some interesting results on such processes will be discussed in Chapter 7.) As the pump phase is deterministic and constant, it is the magnon-phase that plays a key role in this process. The phase-mismatch mechanism is intrinsic; nevertheless, it points to the important role of the magnon phase in governing the nonlinear behavior of the magnetic system. As mentioned earlier, the simulation results in Fig. 6.1 show the selective excitation of the $\omega_k/2\pi = 3\ GHz$ mode while the rest of the modes (thermally generated and shown as a colored band in Fig. 6.1 with $\omega_k/2\pi \neq 3\ GHz$ hardly shown any increase.

As discussed earlier, however, the phase mismatch can also be extrinsically induced by phase-noise, $\phi(t)$. In line with the theory developed in the previous section, we study the effects of Gaussian phase noise on the magnetic system. Compared to the mean, it is the standard deviation, σ, of the phase-noise, $\phi(t)$, that has a dominant impact on the nonlinear behavior of the system; this has been verified in the simulations as well.

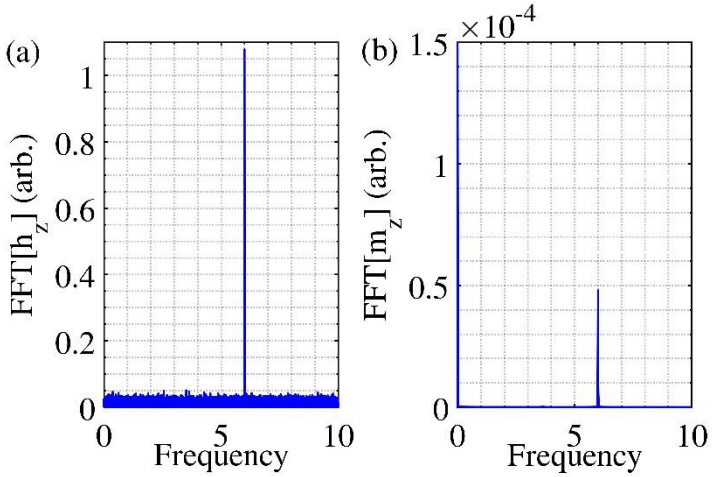

Fig. 6.2. Selective property of parametric pumping. When a 6 GHz microwave signal is employed in the presence of phase-noise with zero mean and standard deviation of 80˚, there occurs noise-rejection at frequencies other than 6 GHz in the absorption. (a), (b) represent the Fourier transform of the microwave input signal and the longitudinal component of magnetization (m_z) respectively. A microwave field of 7.5 Oe is used. (Source: [173])

Consequently, we set the mean of the phase-noise to zero and vary the σ. In Fig. 6.2, we plot the Fourier transform of the spatially averaged longitudinal component, m_z, and that of the noisy microwave signal with a mean of 0 and $\sigma = 80°$. It can be observed, as indicated earlier, that the selective nature of parametric resonance largely amplifies only the 6 GHz component of m_z. (Note that m_z oscillates at twice the frequency of m_y (or m_x) [Chapter 1, Section 1.5].) It is observed, however, that the threshold field increased from 2.7 *Oe* in the absence of phase-noise to 6.6 *Oe* in its presence

The modified threshold-fields can be obtained from the x-intercepts of the growth rate (of the magnons) versus the microwave-field plots, as shown in Fig. 6.3. The growth rate for the various simulation conditions can, in turn, be determined from the slope of the logarithmic plots of the magnon number against time, e.g., using data for t < 2500 ns in Fig. 6.1. (Beyond a standard deviation of ~100° for the phase noise, the threshold field becomes unreasonably high.) Physically, one can see this behavior to be a consequence of the direct relationship between the phases of the external excitation agency and the magnons. As mentioned earlier, threshold-field plays an important role in governing the nonlinear behavior of the magnetic material [11], [18], [115], [147].

The other important inference from Fig. 6.3 is the reduction in the slope of the growth rate ($\frac{dg_{rn}}{dh}$) of the magnons with an increase in σ, as was also deduced from the analytical equations earlier. This is proportional to the coupling factor, V_k (using Eq. (6.2)) and thereby determines the energy coupling from the microwave into the magnetic material. The threshold field increment and the decrement in the slope of the growth rate as obtained from the simulation and theory are shown in Fig. 6.4. The growth rate is a

crucial quantity involved in the determination of the response time of the magnetic system. It constitutes part of the transient state duration before the magnon growth is limited by higher-order processes (phase-mismatch mechanism), as shown in Fig. 6.1. The $\frac{dg_{rn}}{dh}$ and hence, V_k, plays an especially important role in the mechanics of ferromagnet-based microwave cavity experiments [9], [174], [175]. The impact of the phase noise on $\frac{dg_{rn}}{dh}$ is non-trivial, since, in our earlier parametric studies (Fig. 5.7(a)), performed in the presence of an additional secondary frequency, we did not observe such an effect, although we did predict and demonstrate an increase in the threshold field. These results are important for

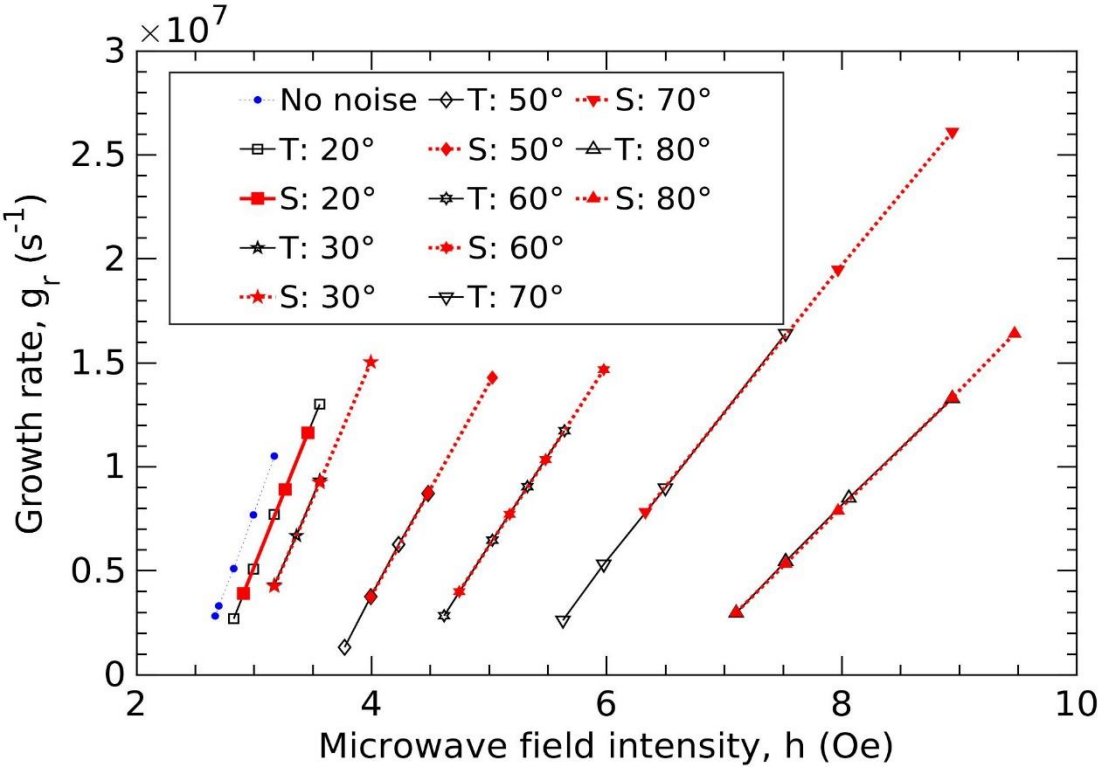

Fig. 6.3. Growth rate of magnons vs. the primary r.f field intensity for various phase-noise standard deviations. 'T' refers to temporal noise, 'S' to spatial noise. The black solid lines with hollow symbols correspond to temporal noise, while the red dotted lines with filled symbols correspond to spatial noise. The quantity in degrees indicates the standard deviation, σ, of the phase noise. Source: [173].

both the traditional and novel classes of applications discussed earlier since device performance characteristics often strongly depend on threshold-field as well as the transient-time. This is evident, e.g., in the ongoing efforts to miniaturize nonlinear magnetic RF device - FSL, especially for autonomous automobile applications [2].

We also computed, using our simulation system, the shift in the threshold field in the presence of Gaussian *spatial* phase noise $\phi(x)$, where x represents the spatial location x in the magnetic sample. Mathematically, we can consider the effective microwave-field at the location x: $h(x) = h\cos\left(\omega_p t + \phi(x)\right)$. The simulation results are nearly identical to the curves obtained using the temporal noise (Fig. 6.3). As before, the mean of spatial phase noise is kept zero in all the cases. Hence, it is interesting that the threshold-field

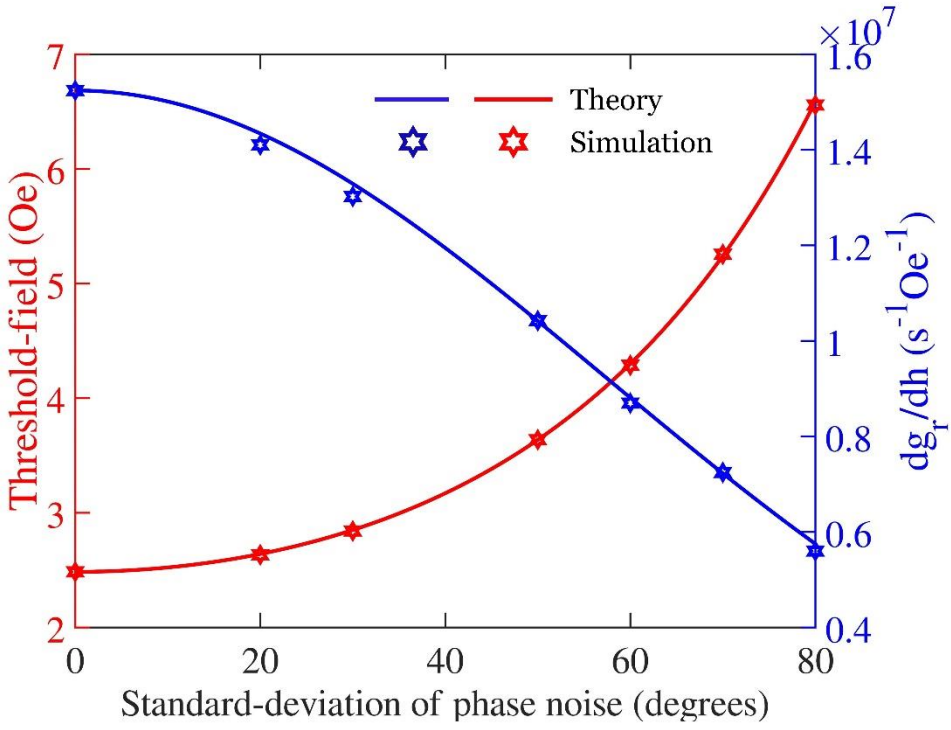

Fig. 6.4. Comparison of simulated data and theoretical prediction of threshold-fields and the slope of growth rate, $\frac{dg_r}{dh}$ w.r.t microwave field intensity. Source: [173].

shift and the slope-reduction effect caused by the spatial noise turn out to be nearly identical to that in the case of temporal noise. This points to the importance of process variations and microstructural quality in the production of magnetic samples.

6. 3 Conclusions

To summarize this work: a new way of understanding the consequences of phase noise is presented. The methodology described helps us to gain new insights into the behavior of magnons under phase-noise. The results are general and are independent of the mode of pumping (parallel or perpendicular) and the magnetic material (applies to insulators, e.g., YIG as well as metals, e.g., NiFe). In fact, the results could be used to understand the nonlinear properties of other parametric systems that involve three-particle processes.

It is observed that both the threshold-field intensity and the growth rate of magnons scale exponentially with the variance of the effective phase-noise in the system. Moreover, both the spatial and temporal variance can contribute to the changes in the nonlinear properties. It should be stated that noise need not necessarily be a nuisance, but it can make possible system behavior that does not exist in the absence of noise. For example, from the results, it can be noted that the threshold field can be deterministically increased by adding phase-noise into the magnetic system. Clearly, a proper understanding of the consequences of magnon phase-noise is not just interesting from a physical perspective for revealing new phenomena but also crucial from an application perspective in order to elicit desired functionalities in magnon-based devices.

Chapter 7 Higher-Order Scattering Processes

The research discussed in chapters until now focused mainly on the details of three-particle processes wherein two magnons are created at the expense of an absorbed photon. As the pumping continues, more and more magnons are created. Eventually, these magnons start to interact amongst each other via secondary four-magnon interactions. Since such processes represent interactions amongst the parametrically excited magnons, they can be considered to be due to higher-order terms in the perturbative expansion of the energy Hamiltonian that were ignored in the previous treatment. Such 4-magnon processes have been attributed to limiting the further growth of the magnons. In this chapter, I discuss the mathematical underpinnings of such processes and, using simulations, demonstrate some of the interesting higher-order phenomena, including microwave-induced hysteresis. Susceptibilities are also obtained using micromagnetic simulations and compared with the analytical model. The role of nonlinear damping in the amplitude limitation of magnons is highlighted. I have also demonstrated nonlinear negative damping in the magnetic system using simulations [176].

7.1 Theory of Higher-Order Nonlinearities

In order to understand higher-order nonlinear processes, I begin the study by considering the Hamiltonian of the magnetic system, which for the case of parallel-pumping of ferromagnets can be written as [110]:

$$\mathcal{H} = \sum_k \omega_k b_k b_k^* + \left\{\frac{1}{2}\sum_k hV_k b_k^* b_{-k}^* \cos(\omega_p t) + \text{c. c}\right\} + \mathfrak{H}_{int} \tag{7.1}$$

where the complex numbers b_k's are the classical analogs of Bose-operators introduced in Chapter 3, and c.c represents complex conjugate. Let the energy due to microwave pumping be represented by $\mathcal{H}_p \equiv \frac{1}{2}\sum_k hV_k b_k^* b_{-k}^* \cos(\omega_p t) + \text{c. c.}$ In Eq. 7.1, the first term gives the dispersion relation, while the second corresponds to the energy which gets coupled from the applied microwave or RF field into the magnetic system. In my earlier treatment, the higher-order interaction term of the Hamiltonian, $\mathfrak{H}_{int}$, was ignored. As long as the pump power from the microwave is close to the threshold, this approximation is largely accurate; however, at higher microwave powers, the higher-order correction cannot be ignored without incurring non-trivial inaccuracies.

To study the resulting higher-order nonlinear effects, one must consider the contributions from, $\mathfrak{H}_{int}$. It has been shown in the earlier chapters that the parallel RF pumping can directly excite magnons (or parametric spin-waves) such that both the energy and momentum are conserved: $\omega_p = \omega_k + \omega_{-k}$, where ω_p is the energy of the photon while ω_k and, ω_{-k} refer to that of the spin-waves (of wave-vector *k* and -*k* respectively), such that $\omega_k = \omega_{-k} = \frac{\omega_p}{2}$ (provided such half energy states are allowed by the dispersion-relation). Since all the excited magnons have energies close to $\frac{\omega_p}{2}$, we can as an approximation at the next-order, retain in the interaction Hamiltonian only the terms involving 4-magnon processes. These processes are governed by the following conservation considerations:

$$\omega_{k_1} + \omega_{k_2} = \omega_{k_3} + \omega_{k_4} \text{ with } k_1 + k_2 = k_3 + k_4 \tag{7.2}$$

It has been shown in the past [110] (also pointed out in Fig. 2.11) that the significant 4-magnon interactions are of form 2↔2 as above, i.e., 2-magnons interacting to produce 2-other magnons. Other 4-magnon processes of the form 1↔3 are usually such that they cannot satisfy the energy-momentum conservation for the available states. In accordance with the nonlinear pair-interactions theory of [110], [177], [178], the interaction Hamiltonian, $\mathfrak{H}_{int.}$ can be written as:

$$\mathfrak{H}_{int.} = \sum_{k_1,k_2,k_3,k_4} \mathbb{T}(k_1, k_2;\ k_3, k_4) b^*_{k1}\, b^*_{k2} b_{k3} b_{k4} \Delta(k_1 + k_2 - k_3 -\ k_4) \quad (7.3)$$

where $\mathbb{T}$ is the four-magnon interaction factor; $b_k = |b_k| e^{-i\phi_k}$ is the complex-amplitude of the spin-wave; $\Psi_k \equiv \phi_k + \phi_{-k}$ represents the total phase of the interacting pair of magnons.

By keeping only those parts that are diagonal w.r.t wave pairs, Eq. 7.2 can be written as [110]:

$$\mathfrak{H}_{int.} = \sum_{k,k'} (T_{kk'}\, b_k b^*_k b_{k'} b^*_{k'} + \frac{1}{2} S_{kk'} b_k b^*_{k'} b_{-k} b^*_{-k'}) \quad (7.4)$$

where $T_{kk'} \equiv (k, k'; k, k')$ and $S_{kk'} \equiv (k, -k; k', -k')$. In terms of slow variables, $c_k = b_k e^{-i\omega_p t/2}$, the equation of motion (Eqn. 7.1):

$$\frac{\partial c_k}{\partial t} + (\eta_k + i\widetilde{\omega}_k) c_k = -iP_k c^*_{-k} \quad (7.5)$$

where $\widetilde{\omega}_k = \omega_k - \omega_p/2 + 2\sum_{k'} T_{kk'} c_{k'} c^*_{k'}$ and $P_k = hV_k + \sum_{k'} S_{kk'} c_{k'} c^*_{k'}$. (In the absence of factors $T_{kk'}$ and $S_{kk'}$, we recover Eq. 3.27 with $\widetilde{\omega}_k = \omega_k$ and $P_k = hV_k$) The factor η_k represents the relaxation rate of the spin-wave mode with wave-vector, *k*.

Next, let us look at the energy that gets pumped into the magnon system from the RF signal:

$$W = \frac{\partial \mathcal{H}_p}{\partial t} = i\omega_p(hV_k c_k c_{-k}^* - c.c) = hV_k|c_k|^2 \sin(\Psi_p - \Psi_k) \tag{7.6}$$

For maximum energy transfer, this implies, $\sin(\Psi_p - \Psi_k) = 1$ or $\Psi_p - \Psi_k = \frac{\pi}{2}$. (We have already seen the implications of this in Fig 6.1, where the modification of $\sin(\Psi_p - \Psi_k)$ away from 1 lead to the saturation of the magnon numbers. While in Fig. 5.6(b), it was the secondary microwave frequency that caused $\sin(\Psi_p - \Psi_k)$ to be different from 1, making it harder for the nonlinearity to occur.)

Let us define correlation functions [110], $n_k \equiv < c_k c_k^* > = |c_k|^2$ and $\sigma_k \equiv < c_k c_{-k} >$ whereby $\sigma_k = n_k \exp(i\Psi_k)$. n_k can be interpreted as the number of magnons. As seen earlier, for a given bias field, when the RF field exceeds the threshold (h_{th}) parametric magnons are excited. On the resonance surface where such parametric excitation occurs, for not so high excesses in the RF power above the threshold [110]: $hV_k \sin(\Psi_k) = \eta_k$ and $hV_k \cos(\Psi_k) = -SN$ (N is the number of magnons) from which:

$$N = \frac{\sqrt{h^2 V_k^2 - \eta_k^2}}{|S|} \tag{7.7}$$

where, $N = \sum_k n_k$.

The 4-magnon interactions can cause the angular difference between the pump and magnon-pair phases to be different from $\pi/2$, leading to amplitude limitation. This is characterized by 4-magnon interaction parameter, *S*, which can be seen as a measure of phase-mismatch-dependent amplitude-limitation.

There exists yet another mechanism that can bring about the amplitude limitation of spin waves- *nonlinear damping* [45], [58], [179]. In general, the magnon number dependent damping can be approximated as:

$$\eta_k = \eta_k^0 + \int \mu_{kk'} n_{k'} dk' \tag{7.8}$$

where η_k^0 is the linear damping, and $\mu_{kk'}$ is the damping coefficient. The equation above suggests that an increase in the number of magnons can result in an increase in the effective relaxation rate of the magnetic system. Intrinsic sources of such damping can be the various scattering processes within the magnetic material, e.g., three-magnon processes such as confluence (two magnons combine to produce a different magnon) and splitting (a magnon splits into two different magnons) [180], [181]. As the number of magnons increase, the effective damping is altered. For small excesses above the RF field threshold (h_{th}), assuming narrow wave-packets, i.e., a dominant spin-wave mode, we can write (by suppressing wave-vector, *k*) $\eta = \eta^0 + \mu N$, so that:

$$N = \frac{\eta^0}{|S|} \frac{-\xi + \sqrt{p(\xi^2+1)-1}}{\xi^2+1} \tag{7.9}$$

where, $p = \left(\frac{h}{h_{th}}\right)^2$ [For $h > h_{th}$, p is a measure of the overdrive beyond threshold]; $\xi = \frac{\mu}{|S|}$, i.e., the ratio of the nonlinear factor: μ and the four-magnon correlation factor, *S*. The energy entering the magnetic system from the RF field (seen in Eq. 7.6) can also be written as: $W = \frac{\partial \mathcal{H}_p}{\partial t} = \frac{1}{2}\omega_p \chi'' h^2$, from which we can obtain $\chi''(\omega) = -\frac{2}{h}\sum_k \mathrm{Im}(V_k^* \sigma_k)$ giving:

$$\chi'' = \frac{2V^2}{|S|}\left[\frac{p\xi(\xi^2+1)+(1-\xi^2)\sqrt{p(\xi^2+1)-1}-2\xi}{p(\xi^2+1)^2}\right] \tag{7.10}$$

7.2. Number of Magnons and Magnetic Susceptibility

Simulations are performed for bias fields of 200 Oe and 540 Oe, with a microwave excitation of 6 GHz, using the 2D micromagnetic solver discussed in Chapter 4. The simulations employed the same parallel configuration as before with parameters: $M_s = 145\ \frac{emu}{cm^3}$, $A_{ex} = 3.77 \times 10^{-7}\ \frac{ergs}{cm}$ and the intrinsic damping factor, $\alpha = 7 \times 10^{-3}$. The higher damping is chosen to keep the simulation run times reasonable as these studies investigate the steady-state behavior of the system and lower the damping the longer it takes to attain the steady-state.

At first, I compute the number of magnons in the steady-state for a 6 GHz pump near the threshold for two cases of bias-fields: 200 Oe and 500 Oe. Fig. 7.1 shows the behavior of the magnon number, (N) and imaginary part of the susceptibility (χ'') w.r.t to the microwave field intensity. As can be seen, the characteristics of the simulated data

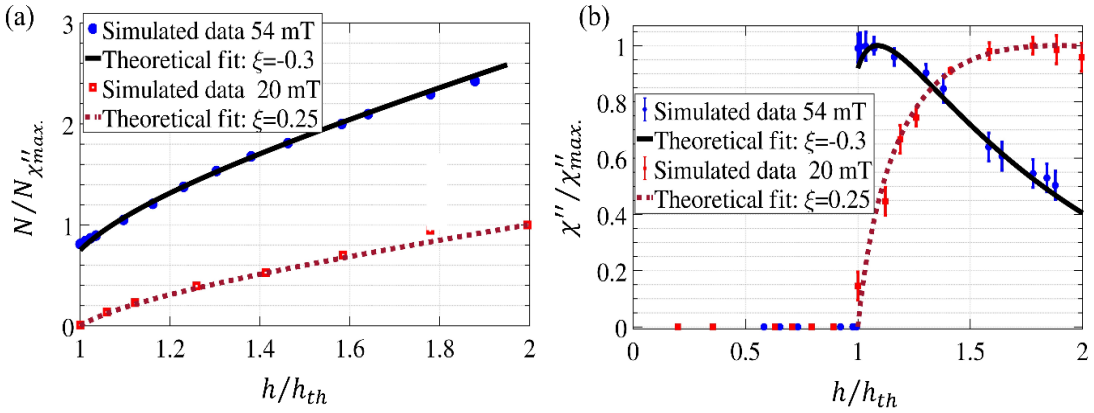

Fig. 7.1. (a) Total number of magnons evaluated during the steady state for a pump frequency of 6 GHz at 200 Oe and 540 Oe at various RF intensities above the threshold. Theoretical curves use Eq. (7.9) with $\xi = \mu/|S|$ =+0.25 and -0.3 for 200 Oe and 540 Oe respectively. Numbers have been normalized w.r.t corresponding values at $\chi'' = \chi''_{max}$. (b) Magnetic susceptibility, χ'' vs. h/h_{th} for an RF frequency of 6 GHz at 200 Oe and 540 Oe. Same ξ values as in (a) are used for the theoretical plots in (b), which uses Eq. (7.10). (Source:[176])

are well captured by the theoretical model with $\xi = \mu/|S|$ =+0.25 and -0.3 for 200 Oe and 540 Oe, respectively. More importantly, for a given bias field, the same numerical value of ξ captures the behavior of both N and χ''. Note that the developed theoretical model accurately predicts the abrupt initial jump in χ'' in the case of 540 Oe. It is observed that the abruptness of the jump could not be reduced by weakening the RF power. At 200 Oe, the increase in χ'' is relatively gradual. The position of the maximum in χ'' is also well predicted by the theory.

7.3 Hysteresis

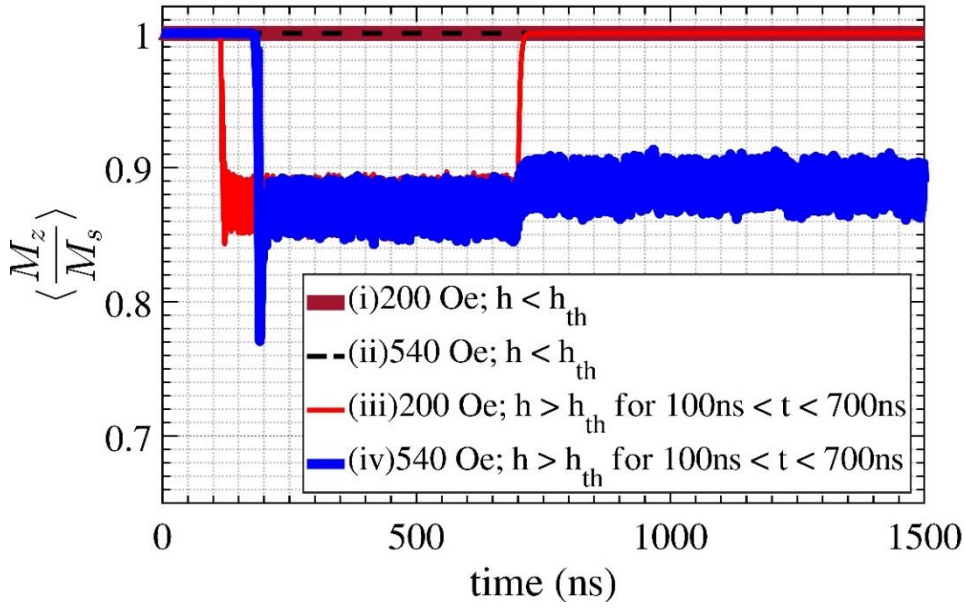

Fig. 7.2. Effect of switching the RF field from a super-critical (h > h_{th}) value to a value below the threshold for 200 Oe, and 540 Oe. The RF field is turned on at 100 ns in all cases. Pumping is below threshold (h/h_{th}<1) with bias-fields (i) 200 Oe and (ii) 540 Oe. (Curves (i) and (ii) are nearly coincident.) Between 100 ns and 700 ns the pumping is allowed to exceed the corresponding threshold in cases (iii) and (iv) with bias fields 200 Oe and 540 Oe, respectively. (Source: [176])

An interesting case of nonlinear damping occurs when the factor ξ is negative (or equivalently the factor μ in Eq. 7.8 is negative). At 540 Oe, for the 6 GHz pump used, we demonstrate in Fig. 7.2 that reducing the RF power at 700 ns to a value lower than the threshold does not take the longitudinal component of magnetization, M_z, back to saturation (Fig. 7.2 (iv)). Instead, M_z settles around 0.87 M_S, with $\chi'' = 7.48 \times 10^{-5}$ from its value of ~10^{-12} otherwise. However, at 200 Oe, such a reduction in RF power, to howsoever small a value below the threshold, always returns M_z to saturation (Fig. 7.2(iii)). In other words, an unexpected hysteresis is exhibited in Fig. 7.2(iv) but not in Fig. 7.2(iii), both of which have the same lowering of M_z in the time-range $\mathbb{I}$ (=100ns < t < 700ns). When the simulations were performed for similar χ'' in $\mathbb{I}$, yet again, the bistability was found only for 540 Oe.

The results in Fig. 7.2 (iv) can be interpreted in terms of the nonlinear damping theory with a negative value of $\xi = -0.3$ at 540 Oe. The effective negative damping means that the magnons created (before 700 ns) do not undergo the same relaxation as those created in the case of 200 Oe. Since a reduction in M_z corresponds to the number of magnons present, this also means the possibility of two different magnon numbers for the same RF intensity, i.e., the availability of bistability at 540 Oe.

The negative nonlinear damping is attributed to three-magnon confluence processes [179]. Next, I would like to recount a theoretical explanation for the above observation based on [58], [182]. A parametrically excited spin-wave with wave-vector, k, can combine with a thermal spin-wave with wave-vector,k_1, to produce a k_2 spin-wave,

i.e., $k + k_1 = k_2$ (wave-vector conservation) and $\omega_k + \omega_{k_1} = \omega_{k_2}$(energy-conservation). The relaxation contribution from the confluence, η_k^c:

$$\eta_k^c \propto \int (n_{k_1} - n_{k_2}) \delta(k + k_1 - k_2) \times \delta(\omega_k + \omega_{k_1} - \omega_{k_2}) dk_1 dk_2 \quad (7.10)$$

where n_{k_1}, n_{k_2} represent the number of thermal magnons with wave-vectors: k_1, k_2, respectively. In general, near thermal equilibrium, the relaxation due to confluence processes, $\eta_k^{c,eq} = \beta(n_{k_1} - n_{k_2})$ with a proportionality constant, β. The difference is such that this leads to a positive relaxation. Under the parametric pumping, however, the confluence processes increase the number of k_2 spin-waves and reduce the k_1 spin-waves, thereby reducing the difference $(n_{k_1} - n_{k_2})$. Hence, there are two competing processes: (1) confluence involving parametric magnons trying to reduce the difference and (2) thermal relaxation, which tries to maintain the equilibrium number of magnons. One can set up the following rate equations: $\dot{n}_{k_1} = -\eta_{k_1}(n_{k_1} - n_{k_1}) - \eta_k^c n_k$ and $\dot{n}_{k_2} = -\eta_{k_2}(n_{k_2} - \bar{n}_{k_2}) + \eta_k^c n_k$. In equilibrium, i.e., $\dot{n}_{k_1} = \dot{n}_{k_2} = 0$, for $\beta/[\frac{\eta_k^c}{\eta_{k_1}} + \frac{\eta_k^c}{\eta_{k_2}}] \ll 1$ we recover: $\eta_k^c = \eta_k^0 - \mu_k n_k$; in the case of a dominant mode, we simply have $\mu_k = \mu = \eta_k^0 \beta \left(\frac{1}{\eta_{k_1}} + \frac{1}{\eta_{k_2}}\right)$.

Hysteresis is an interesting effect both from the viewpoint of physics and applications as it can be used to enable bistable states. It is interesting to note that the thermal magnons have an important role to play in such phenomena through 3-magnon scattering processes. This underscores the importance of thermal magnons as they can affect the higher-order scattering processes apart from acting as a source of background noise. In the light of these discussions, from a computational perspective, it becomes

imperative to consider the effective-magnetic field due to thermal fluctuations accurately. It must be pointed out, however, that a direct demonstration of such theoretical considerations remains to be carried out (experimentally or computationally).

7.4 Conclusions

The non-zero value of ξ is suggestive of the importance of the phase-mismatch mechanism and nonlinear damping in magnon interactions above the microwave threshold. The higher the microwave power beyond the threshold, the higher is the importance of the two processes. It has been shown that the two processes can significantly influence magnetic susceptibility, often the quantity of interest for many of the magnetics-based applications. In addition, the role played by the negative nonlinear damping in bringing about hysteresis effects has been demonstrated. The unconventional hysteresis effects based on parametric processes can be useful for enabling dynamic bistability. The results discussed in the chapter, although rather short, provide crucial insights into higher-order magnonic processes, where few studies have been performed historically. These help to advance the understanding of the magnon mechanics for precision magnonic devices. The theoretical results are in excellent agreement with the predictions from simulations. In this chapter, only a limited study involving higher-order has been performed. There remain a lot of interesting and useful phenomena to be explored, especially regarding the confluence and splitting of magnons and their potential applications. Additional factors contributing to relaxation also remain to be investigated. The temperature dependence of hysteresis would be another potentially useful study for the future.

Chapter 8 Heat Assisted Bit Patterned Shingled Recording

As mentioned in Chapter 1, magnetic recording can be considered as an application that involves the interaction of magnetic-material with high-frequency electromagnetic fields [103]. The goal of such an interaction is to locally switch the magnetization in the material - a highly nonlinear process. The process of switching the magnetization is called writing the media. The primary difference from the studies in the previous chapters lies in the strength of the magnetic field. The write fields involved in recording can be a few thousands of Oe as opposed to a few Oe (or even sub-Oe) in the case of microwave-based excitation. In parametric pump studies discussed earlier, the magnetic material remained largely saturated; consequently, the microwave fields were treated as perturbations (e.g., Eq. 7.1). However, now the magnetic fields are high enough to switch the magnetization and, therefore, involve extremely high nonlinearities. The other major difference from the previous chapters lies in the material used. While the microwave-based studies employed YIG- an insulator with low anisotropy, magnetic recording employs the alloy iron platinum (FePt) that is metallic and has relatively high anisotropy. The high anisotropy helps in stabilizing the magnetization of the dots of the bit patterned media (BPM) against thermal fluctuations. This is important since it is the dots of the BPM that represent a bit.

Magnetic recording continues to be the prominent means of data storage, especially when high storage capacities are needed. The exponentially growing demand for data storage in the digital age has continuously pushed the magnetic-recording research frontiers towards higher data densities. State-of-the-art hard disks employing Heat Assisted Magnetic Recording (HAMR) carry a miniature laser to enable data writing while helping achieve higher data densities. Apart from such novel techniques, new storage media and/or

schemes are also being explored to make the hard disks competitive compared to solid-state-based technologies. Important in this context is the BPM, in which dots or islands of magnetic material are used to store information. BPM, as opposed to the continuous media, has shown the capability of offering high data densities exceeding 5 Tbpsi (Terabits per square inch) when used with HAMR [183]-[186]. Such schemes can be employed to increase the storage capacity in the band write/overwrite schemes of recording like shingled recording. In this article, I study and design a shingled writing scheme for BPM to improve writability and Bit Error Rate (BER). Shingled magnetic recording refers to a scheme of recording where the newly written tracks overlap part of the previously written tracks, allowing for higher data density.

In this chapter, I investigate the writing of dots that are not directly under the laser pulse. Such a shifted scheme of writing allows higher densities when used with shingled recording. A further increase in the recording density can be obtained by using composite structures, comprising a super-paramagnetic writing layer and a (doped) FePt storage layer. Effect of head velocity, Curie-temperature variation, track mis-registration, and dot-position jitter on the standard deviation of switching distribution are studied to evaluate the designs that offer data densities as high as ~16 Tbpsi.

8.1 Methodology

The goal here is to design and optimize shingled BPM, which uses HAMR. The basic layout of BPM is shown in Fig. 8.1. A near field transducer (NFT) is used to optically heat the recording layer of the media. The dots are arranged along the cross- and down-

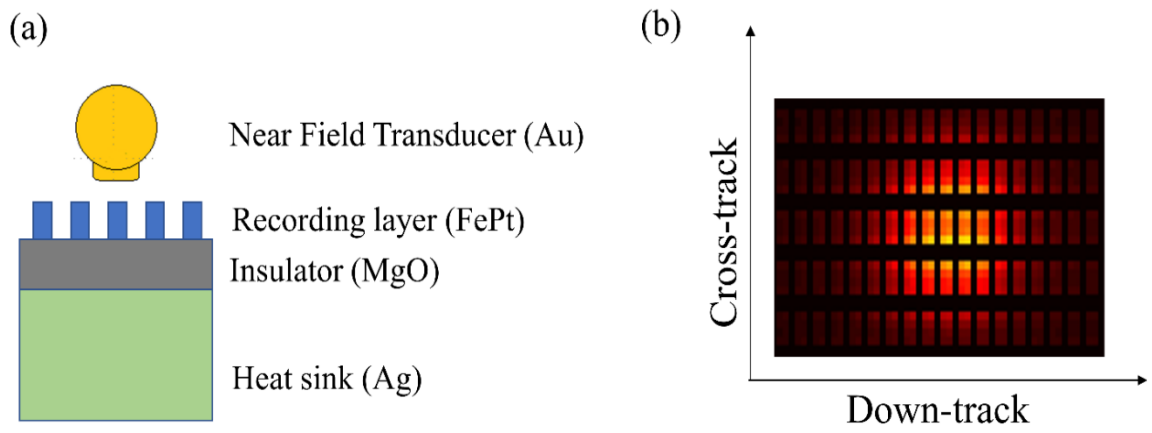

Fig. 8.1. Schematic of Bit Patterned Media (BPM). (a) Side view showing the recording stack comprising various layers. A near field transducer (NFT) flown above the recording layer provides the optical heat pulse. (b) Top view showing the arrangement of magnetic dots along cross-track and down-track directions.

track directions, as shown in Fig. 8.1 (b). The optical head heats up local regions of the recording region, momentarily reducing their anisotropy. A sufficiently strong magnetic field is then applied to the heated dot as it cools down using a write-head (not shown in Fig. 8.1), in order to change its magnetization. The simulation of the recording process, hence, can be thought to be comprised of three steps:

(1) Determination of the optical power input to the recording layer from the NFT.

(2) Calculation of temperature across the recording stack that comprises a recording layer, an insulator, and a heat sink.

(3) Determination of the state of the target bit or dot using atomistic and renormalization simulations. Temperature, as determined from Step 2 along with an applied magnetic field, is used to study the switching probability of the dot.

8.2 Temperature Profile Evaluation

A. Optical power calculation

The optical energy is transferred from the NFT to a small spot on the recording media. The resulting power absorption in the media is evaluated by employing Finite Difference Time Domain (FDTD) calculations as described in [187]. Maxwell's equations are solved to predict the propagation of electromagnetic waves. Different components of the HAMR system are comprised of different optical properties increasing the computational complexity. A lollipop near-field-transducer (NFT) is flown above the storage media at a velocity of 20 m/s. The waveguide consists of Ta_2O_5 core (refractive index = 2.15) wrapped by Al_2O_3 cladding (refractive index =1.65). The lollipop, made up of Gold (Au), is at a distance of 20 nm from the waveguide. The radius of the lollipop is 100 nm with the peg dimensions of 20 nm along the down-track and 24 nm along the cross-track, at the air bearing surface (ABS). The fly height is 7.5 nm.

B. Heat Equation

The heat equation with due consideration to thermal boundary resistance (TBR) was then solved to calculate the heat profile ([91], [188], [189]) of various dots of interest. The heat Fourier equation, shown in Eq. 8.1, describes the heat dissipation and temperature change with time:

$$\frac{\partial T}{\partial t} = D\nabla^2 T + \frac{P}{c} \tag{8.1}$$

where D (=κ/c) is the diffusion coefficient, κ is thermal conductivity, and c is the specific

heat capacity. The power absorption, *P*, is obtained from FDTD simulations. As mentioned earlier, the recording stack comprises multiple layers. Effective thermal conductivity is accordingly considered at each interface to account for the interfacial effect and thermal boundary resistance:

$$\frac{1}{\kappa_e} = \frac{1}{2}\left(\frac{1}{\kappa_1} + \frac{1}{\kappa_2}\right) + \frac{TBR}{d} \tag{8.2}$$

in which κ_1 and κ_2 are the thermal conductivity of the two materials that form the interface, and *d* is the thickness of the interface.

8.3 LLG-based Simulations

The second part of the investigation involves magnetic simulations to study switching probability distribution when a magnetic field is switched at different times as the head moves over the media. At first, I use atomistic simulations to determine the magnetization state of the dot. Similar to the approach taken in earlier works, atomic spin evolution is modeled using the LLG ([188], [190]). The dimensions of the dots involved in BPM are so small (a few nm) that these can be considered to be largely single domain particles. The magnetic fields of importance are the exchange, anisotropy, and thermal fields; the weaker dipolar fields are ignored in the interest of computational simplicity. BPM is often studied using atomistic simulations that provide a more rigorous treatment of the short-range exchange fields by using realistic exchange constants [191], [192]. For FePt, five different exchange constants are used [193].

In addition to the atomistic simulations, I also make use of renormalization simulations. These simulations try to capture the magnetization state near the Curie

temperature using renormalization theory [194] (Nobel prize, 1982). Although the theory strictly applies only at the Curie temperature, we assume it to be applicable in a temperature range around the Curie temperature. The usual LLG based micromagnetic models for HAMR are based on assumptions that are too simplified to capture the magnetization dynamics, especially at temperatures close to T_C, where long-range correlations can develop in the magnetic material. In the renormalization simulations, the system is divided into multiple blocks, and for each block, I assign renormalized parameters for anisotropy, exchange constant, damping constant, etc. Such simulations have been shown to accurately predict the behavior of the magnetic system at high temperatures [195, 196].

8.4 Offset Shingled Writing

In this work, I use an offset shingled scheme [103], wherein the target track, i.e., the track being written, is offset w.r.t the laser. Traditionally, one would write the track directly beneath the laser beam; however, using an offset track can allow higher data densities. In Fig. 8.2, the traditional writing scheme is shown by the laser-pulse (in red) with the smaller peak temperature, wherein it is the *on-track* dot (directly beneath the laser) that gets written. In the new scheme, I employ a different laser pulse – with a higher peak but the same full width at half maxima (FWHM) (in blue) as the former laser pulse, to write an offset track (in red). The idea is to arrange the offset track at a position where the temperature gradient is the highest. This would ensure the highest difference in temperature between the adjacent dots, thus reducing adjacent track erasure (ATE) – a form of noise wherein inadvertent writing occurs on the adjacent tracks.

Using a laser beam, which is offset by a distance X-peak with respect to the dot being written, as shown in Fig. 8.2, allows one to make use of the higher temperature differences that appear between consecutive cross-tracks. The design problem, in this case, aims to find the optimum track pitch ($X_{track\text{-}pitch}$) for an optical pulse of given FWHM such that the temperature difference between the track desired to be written and the previously written adjacent track is enough to ensure a sufficiently small ATE. Further, Bit Aspect Ratio (BAR, i.e., the aspect ratios of the dot) optimization was done to increase the areal storage density. It is evident that the higher the temperature, the closer the tracks can be placed. However, keeping in mind the practical limitations, the highest temperature used in this study is limited to 775 K.

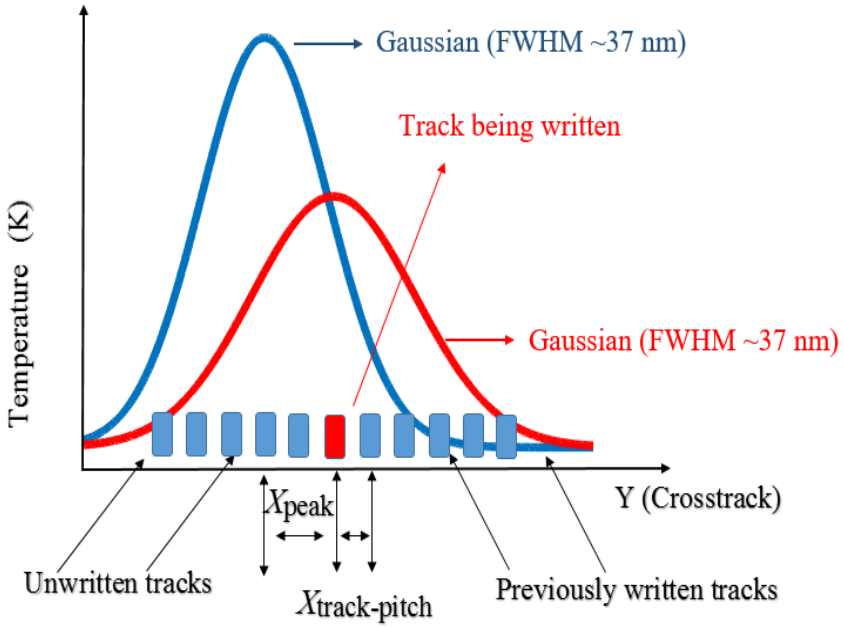

Fig. 8.2. An offset X-peak between the heat-pulse and desired dot allows the dots to be placed closer together compared to the zero offset case. (Source: [103])

8.5 Media Designs

In the next section, possible media designs are explored. At first, I consider the recording layer to be composed of single-layered FePt dots. Thereafter, a composite recording layer with two layers – a magnetically soft layer to aid switching and a magnetically hard storage layer, is studied.

A. FePt Media

A three-layered media comprising a 12 nm FePt (storage layer), 16.5 nm MgO (insulator) and 30 nm of Au (heat sink) is considered (as in Fig. 8.1). The thermal conductivities used are 50, 6 and 200 W/mK, along with specific heat capacities of 3, 2 and 3 MJ/mK, respectively for the three layers [197]. Dimensions of the bits are 10.5 nm (down-track) x 4.5 nm (cross-track) with 6 nm x 3 nm dots. A TBR of $10^{-8}\ m^2$K/W is used. The moving head is centered on the track. The evaluated temperature profile for five adjacent tracks along with that of the on-track, is shown in Fig. 8.3(a).

Two parameters, as described in prior work [188], are of importance in the BPM write process analysis: On-Track bit error rate (BER) and adjacent track BER. On-track BER is determined by using an error-function fit to the switching probability distribution as given in [198]. Note that the probability of error is given by:

$$P(E) = \int_{-\infty}^{\frac{-t_w}{2}+\Delta} p(t)dt + \int_{\frac{t_w}{2}+\Delta}^{\infty} p(t)dt \ = \frac{1}{2}\left[erfc\left(\frac{\frac{t_w}{2}-\Delta}{\sigma_t\sqrt{2}}\right) + \ erfc\left(\frac{\frac{t_w}{2}+\Delta}{\sigma_t\sqrt{2}}\right)\right] \quad (8.3)$$

where Δ denotes the jitter in the position of the dot along the down-track direction. Initially, I assume no jitter ($\Delta = 0$) for the designs. t_w represents the writing window (obtained as the ratio of bit length and head velocity) and σ_t is the standard deviation of the switching

distribution. P(E) represents the probability of error or the on-track BER. For a maximum BER of 10^{-3}, the critical (maximum) value of standard deviation, σ_c, equals 0.079 ns.

Adjacent track erasure is often studied by considering the magnetic decay ratio η^{-1} of a dot of volume V:

$$\eta^{-1} = f_0 \tau \exp\left[-\frac{K(T)V}{K_B T}\left(1 - \frac{H_a}{H_k(T)}\right)^{\frac{3}{2}}\right] \tag{8.4}$$

$K_B = 1.38\,x10^{-16}\,ergs/K$, T = temperature in K. In Eq. (8.4) f_0 and τ are the exposure time and attempt frequency, respectively. K is the anisotropy, H_a is the applied field and

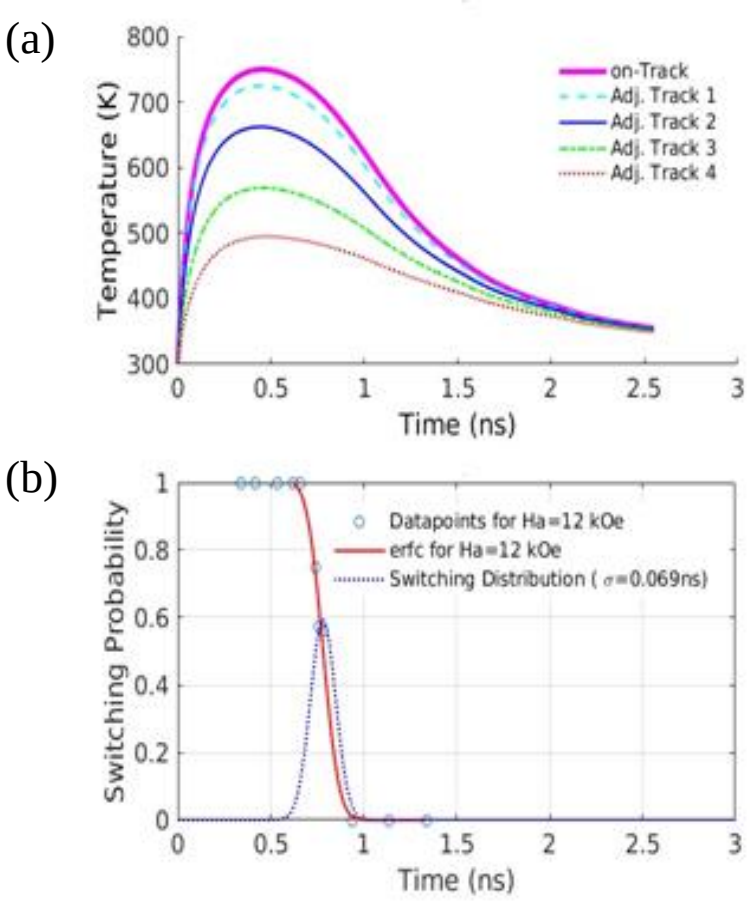

Fig. 8.3. (a) Temperature profile for FePt dots [Bit dimensions 10.5 nm(down-track) x 4.5 nm(cross-track)] (b) Error function (Red curve) fitted to the switching probability, which upon differentiation yields SFD (blue dotted curve) of 0.069 ns. (Source: [103])

H_k is the anisotropy field. Even for our most stressful condition that represents a successful system (temperatures of ~750 K and applied field of 12 kOe), the adjacent track BER was found to be less than ~$3x10^{-6}$.

I chose adjacent-track 2 (AT2) (shown in Fig. 8.3) as the target track because the highest difference in temperature exists between AT2 and AT3. This difference helps to prevent over-write of previously written tracks. However, note that this approach sacrifices the down track thermal gradient that affects the linear density of the system, thus negating part of the gain. For an applied field of 12 kOe and an on-track peak temperature of 750K, $\sigma_t = 0.069$ ns as shown in Fig. 8.3(b) with 0% variation in Tc [as has been done in ([199],

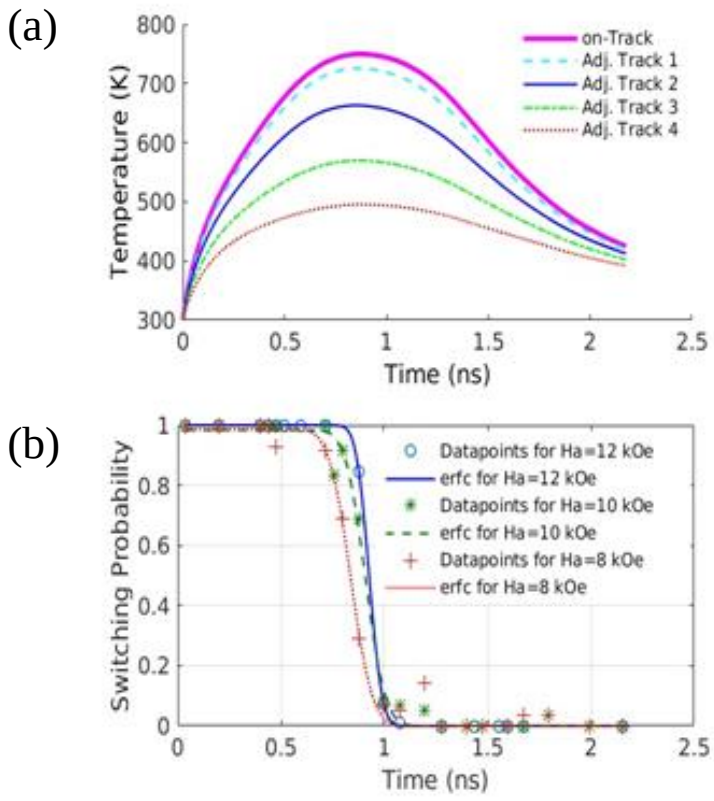

Fig. 8.4. (a) Temperature profile for composite media dots [Bit dimensions 9 nm(down-track) x 4.5 nm(cross-track)]. (b) Error function fit to the switching probability raw data for applied field Ha=8 kOe, 10 kOe and 12 kOe. (Source: [103])

[200])]. Near zero switching probability at the adjacent tracks ensures sufficiently low adjacent-track BER. The temperature difference at the peak between AT2 and AT3, as seen from the figure, is approximately 20 K/nm**.** Allowing 3% variation in critical temperature (Tc) increases the standard deviation of SFD to 0.079 ns while offering an areal density of ~14 Tbpsi.

Also, it can be noted from Fig. 8.3 that except for the bit directly under the laser, the peak temperature for none of the adjacent tracks exceeds the known Curie temperature (~T_c =710 K). However, these bits do switch when magnetic fields switch at appropriate times. This effect has been observed in earlier works on BPM [190]. The bit reversal

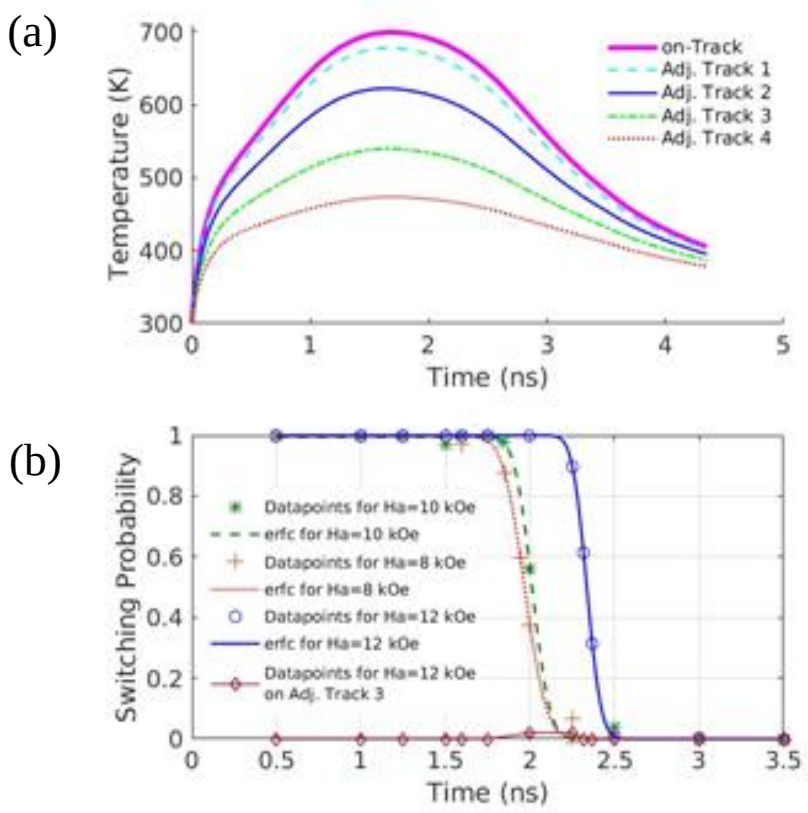

Fig. 8.5. (a) Temperature evolution of composite media dots of dimensions 6 nm (down-track) x 3 nm (cross-track) with a head velocity of 10m/s. (b) Corresponding Switching distribution for applied fields Ha = 8 kOe, 10 kOe, 12 kOe. Also shown is the non-zero switching probability at Ha=12 kOe for the third adjacent track. (Source: [103])

governed by exp (-$\Delta\varepsilon/K_BT$) depends on $\Delta\varepsilon$ (the energy barrier between external-field-dependent favorable and un-favorable orientations). Hence, under-heated (< T_c) switching is explained by a reduction in anisotropy at high temperatures.

B. Composite Media

Composite media uses a superparamagnetic writing layer (corresponding parameters denoted by a subscript wl) and a FePt storage layer (parameters denoted by a subscript sl) [91]. I use the following atomistic values at 0 K: K_{sl}=7e7 $ergs/cm^3$, M_{sl}=1100 emu/cm^3, K_{wl}=11e6 $ergs/cm^3$, M_{wl}=620 emu/cm^3, $T_{c,wl}$=900 K and $T_{c,sl}$=710 K. The exchange constants are assumed to obey: J_{wl}= (J_{sl})*($T_{c,wl}/T_{c,sl}$). Temperature profile calculations and atomistic simulations are done as before in order to obtain the switching profiles. The temperature evolution for a peak temperature of 750 K is as shown in Fig 8.4. A design with an aspect ratio similar to that with FePt gives the standard deviation of SFD as 0.057 ns with 0%Tc variation and 0.063 ns with 3%Tc variation. I now place the bits closer together with bit size of 9 nm (down-track) x 4.5 nm (cross-track) and dot size of 6 nm (down--track) x 3 nm (cross-track) x 9 nm (depth), other layers remaining the same. For a peak on-track temperature of 750K, application of 12 kOe gives standard deviation of 0.05 ns that increases to 0.061 ns when a 3% variation in Tc is allowed. The results are presented in Table 8.1. The DC noise is excluded to ~8 x10^{-3} as only 125 simulations were performed for each configuration. Any designs that suffered from DC noise beyond the transition region have been marked not good. I have also

excluded the designs which showed non-zero switching probability in the nearest adjacent track (adjacent track 3).

Next, the effect of velocity (30 m/s and 10 m/s) on the standard deviation of SFD is studied. The temperature evolution for the two cases for the same distance covered by the head on the media is as shown in Fig. 8.5 and Fig. 8.6, respectively. Note that σ_c takes on new values 0.045 ns and 0.135 ns with velocities of 30 m/s and 10 m/s, respectively.

For 10 m/s, peak OTT of 750 K was found to cause overwriting of the adjacent track. Hence a lower peak temperature of 700 K was used. Even though 12 kOe gives a better standard deviation, it results in adjacent track erasure, owing to the increased time interval in which the adjacent bits are heated. Use of 8 kOe instead of 12 kOe, hence, is found to be more viable at a head velocity of 10 m/s. Results for both velocities are shown in Table 8.1.

Head-velocity → Magnetic field ↓	v=10 m/s $\sigma_c = 0.135$ (700 K)	v=20 m/s $\sigma_c = 0.068$ (750 K)	v=30 m/s $\sigma_c = 0.045$ (750 K)
8 kOe	0.112* (0.125)	0.083**	0.066
10 kOe	0.082**	0.058**	0.047
12 kOe	0.068**(0.080)	0.051*(0.061)	0.031*(0.045)

Table 8.1: Details of simulation results (standard deviation,σ) for different velocities, on-track peak temperatures and applied fields. Values within brackets show σ allowing 3% variation in Tc (for cases in which σ (0% σ_{Tc}) < σ_c). Source: [103]. * Designs which met the BER criteria with no DC noise beyond the transition region. **Designs that met the BER criteria but showed DC noise beyond the transition region. ***Design with adjacent track erasure issues.

The computationally expensive nature of atomistic simulations prevents one from performing a large number of simulations. Renormalization calculations were subsequently performed to look at the same. This technique relies on LLG similar to atomistic

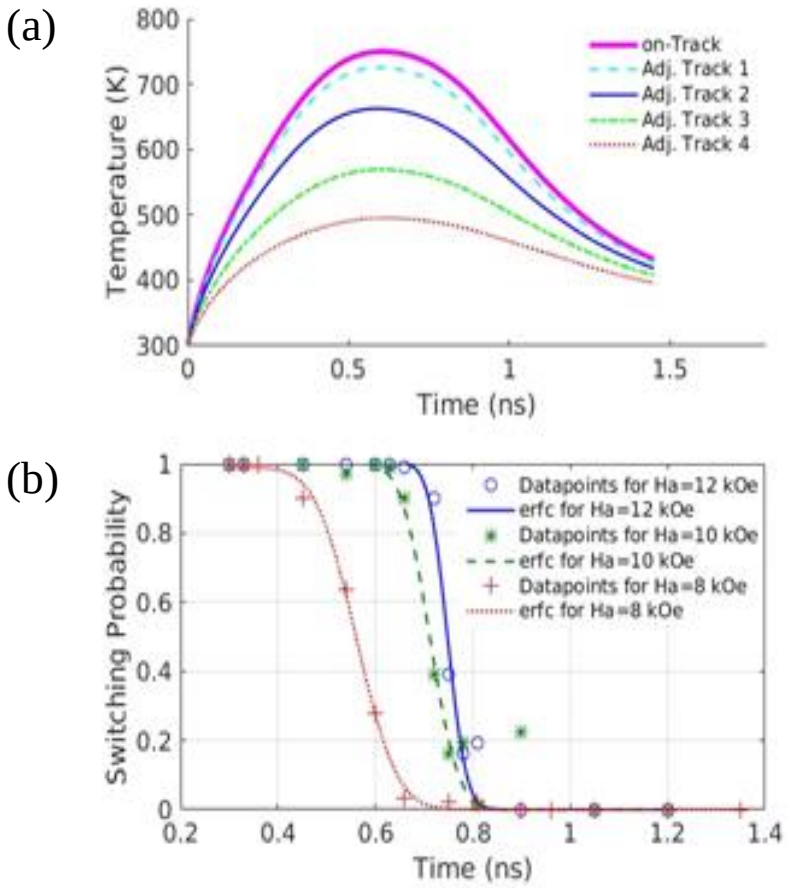

Fig. 8.6. (a) Temperature evolution of composite media dots of dimensions 6 nm (down-track) x 3 nm (cross-track) with a head velocity of 30 m/s, respectively. (b) Corresponding Switching distribution for applied fields Ha = 8 kOe, 10 kOe, 12 kOe. (Source: [103])

simulations; however, the dynamics considered here are of block-spins as opposed to atomistic spins. The block size considered is 1.5 nm x 1.5 nm x 1.5 nm. Temperature-dependent parameters like saturation magnetization, anisotropy energy, damping parameter, and exchange parameters were obtained from previous studies [85]. At least

1000 renormalized simulations were performed for each data point.

As shown in Table 8.2, renormalized results agree well with the earlier results obtained using atomistic simulations; this ensures BER of less than 10^{-3}. Next, the effect of Track Mis-Registration (TMR) is studied. The laser peak, which was centered on-track is now displaced and standard deviations were evaluated. More simulations with higher absolute displacements as in the third row of Table 8.2 were performed. It was found that TMR with a standard deviation of up to 7% is admissible while keeping the BER below 10^{-3}. Finally, I studied the effect of jitter with respect to the positioning of the dots in the down-track direction. BERs evaluated using Eq. (8.3) were $0.91 \times 10^{-3}, 0.98 \times 10^{-3}$ and 0.84×10^{-3} for the velocities 10 m/s, 20 m/s and 30 m/s, respectively. Calculations corresponded to the three cases mentioned in Table 8.2 (renormalized) and were performed using position jitters within a standard deviation of 7% of the bitlength.

Simulation	v=10 m/s Peak OTT = 700 K H_a= 8 kOe $\sigma_c = 0.135$	v=20 m/s Peak OTT = 750 K H_a= 10 kOe $\sigma_c = 0.068$	v=30 m/s Peak OTT = 750 K H_a= 12 kOe $\sigma_c = 0.045$
Atomistic	0.112(0.125)	0.051(0.061)	0.031(0.045)
Renormalized	0.102(0.119)	0.049(0.059)	0.029(0.039)
TMR(%)	0.123(0.131)	0.059(0.062)	0.033(0.045)

Table 8.2 Standard deviations calculated from atomistic and renormalization simulations (v=head velocity, OTT=on track temperature, Ha=Applied field. Values within brackets show standard deviation allowing 3% variation in Tc). Source: [103].

8.6 Conclusions

It has been demonstrated through simulations that shingled writing with bit patterned HAMR can substantially increase storage capacity relative to conventional shingled and to non-shingled HAMR ([183], [201]) (both on BPM). The desired bits herein switch at temperatures lower than the Curie temperature because of reduced anisotropy. Bits of size 9 nm x 4.5 nm with dots of area 6 nm x 3 nm allow a significant increase in density to ~16 Tbpsi. The design is demonstrated to tolerate both TMR and position jitter. The designed density is theoretically the highest data density demonstrated to be possible with due consideration of noise sources like jitter and track mis-registration. Successful realization of BPM, however, would involve overcoming a number of practical challenges. Media fabrication with a track pitch of < 10 nm, would pose a great challenge [202], [85]. In addition, tracking would be another issue that needs to be addressed before data densities as designed herein could be achieved in practice. But nevertheless, the study points out the immense capability of heated dot magnetic recording in achieving extremely high data densities.

Chapter 9 Summary

In this final chapter, I would like to summarize the main conclusions of the research. A state-of-the-art micromagnetics tool has been developed, which allows us to explore the impact of magnon-based nonlinearity. Abstract parametric processes like the three- and four-particle processes have been demonstrated, and their impact on microwave absorption is understood in the context of frequency-selective limiters. It is found that the strength of the microwave should exceed a certain threshold before such processes can be triggered. External and material properties like intrinsic damping, film thickness, microwave field strength, bias field strength, etc., can be used to tailor nonlinear interactions and thereby the desired nonlinear functionality.

A secondary signal near the relaxation rate of the magnetic system is highly efficient in increasing the threshold field. This can also be seen as the modulation of the magnonic phase such that the coupling between the microwave and the dominant magnon is reduced. The significance of the magnon phase in nonlinear processes was demonstrated. Further studies on magnon-phase noise revealed that Gaussian noise leads to an exponential increase in the threshold field. The growth rate of magnons, however, experiences an exponential decrease. It was shown through simulations that spatial and temporal Gaussian phase noises have the same effect on the threshold field. These results can be useful for applications that involve nonlinear processes, as the magnon-phase is found to have a crucial role in such interactions.

Heat-assisted bit patterned media optimization was performed using atomistic and renormalization simulations. A realistic calculation of the optical power incident on the media was performed. Temperature profiles of the dots in the media were determined by solving the heat equation and switching probabilities were calculated using micromagnetic simulations. It was shown that a $9\ \text{nm} \times 4.5\ \text{nm}$ bit with a dot size of $6\ \text{nm} \times 3\ \text{nm}$ would allow an areal density of ~16 Tbpsi under jitter and track misregistration of up to 7%. The design is for shingled heat-assisted bit-patterned media. Such high densities show the immense capabilities of magnetic recording in enabling high-density data storage.

Bibliography

[1] J. D. Adam and F. Winter, “Magnetostatic wave frequency selective limiters,” *IEEE Trans. Magn.*, vol. 49, no. 3, pp. 956–962, Mar. 2013.

[2] M. Shukla, M. Y. Koledintseva, M. Geiler, S. Gillette, M. Hunnewell, A. L. Geiler, “Adaptive interference mitigation using frequency-selective limiters over GPS band for automotive applications,” *IEEE International Symposium on Electromagnetic Compatibility and Signal/Power Integrity (EMCSI)*, Reno, NV, USA, pp. 614–618, 2020.

[3] V. G. Harris, "Modern Microwave Ferrites," *IEEE Trans. Magn.*, vol. 48, no. 3, pp. 1075-1104, Mar. 2012.

[4] M. Geiler, S. Gillette, M. Shukla, P. Kulik and A. L. Geiler, "Microwave Magnetics and Considerations for Systems Design," *IEEE J. Microw.*, vol. 1, no. 1, pp. 438-446, 2021.

[5] A. Chumak, V. Vasyuchka, A. Serga, *et al.*, “Magnon spintronics,” *Nat. Phys.*, vol. 11**,** pp. 453–461, Jun. 2015.

[6] A. Khitun, M. Bao, K. L. Wang, “Magnonic logic circuits,” *J. Phys. D: Appl. Phys.*, vol. 43, no. 264005, 2010.

[7] A. Khitun and K. Wang, “Nano scale computational architectures with Spin Wave Bus,” *Superlattices and Microstructures*, vol. 38, pp. 184–200, Sep. 2005.

[8] M. Vogel, R. Aßmann, P. Pirro, A. V. Chumak, B. Hillebrands, and G. Freymann. “Control of Spin-Wave Propagation using Magnetisation Gradients,” *Sci. Rep.*, vol. 8, no. 11099, Jul. 2018.

[9] X. Zhang, C.-L. Zou, L. Jiang, and H. X. Tang, “Strongly coupled magnons and cavity microwave photons,” *Phys. Rev. Lett.*, vol. **113**, no. 156401, Oct. 2014.

[10] M. Harder, B. M. Yao, Y. S. Gui, and C.-M. Hu, “Coherent and dissipative cavity magnonics.” J. Appl. Phys., vol. 129, no. 201101, May 2021.

[11] A. A. Serga, A. V. Chumak, and B. Hillebrands, “YIG magnonics,” *J. Phys. D: Appl. Phys.*, vol. 43(26), no. 264002, Jun. 2010.

[12] CUDA C++ Programming guide, NVIDIA. Available at: https://docs.nvidia.com/cuda/cuda-c-programming-guide/index.html.

[13] J. Sanders, E. Kandrot, *CUDA By Example: An introduction to general purpose GPU programming*, Boston, MA, USA: Addison-Wesley, 2011.

[14] “Graphics processing unit” Wikipedia: The Free Encyclopedia. Wikimedia Foundation, Web. 7 Aug. 2021. (https://en.wikipedia.org/wiki/Graphics_processing_unit)

[15] S .M. Rezende, “Magnon Spintronics” in *Fundamentals of Magnonics. Lecture Notes in Physics*, vol 96, Cham, Switzerland: Springer, 2020.

[16] T. Bracher, P. Pirro and B. Hillebrands “Parallel pumping for magnon spintronics: Amplification and manipulation of magnon spin currents on the micron-scale,” Phys. Rprts, vol. 699, pp. 1-34, 2017.

[17] S. M. Gillette, M. Geiler, J. D. Adam, and A. L. Geiler, “Ferrite-based reflective-type frequency selective limiters,” in *Proc. IEEE MTT-S Int. Microw. Workshop Ser. Adv. Mater. Process. RF THz Appl. (IMWSAMP)*, Ann Arbor, MI, USA, Jul. 2018, pp. 1–3.

[18] M. H. Francombe and J. L. Vossen, “Magnetostatic waves,” in *Thin Films for Advanced Electronic Devices*, vol. 15. San Diego, CA, USA: Academic, 1991.

[19] J. D. Adam, “*Ferrite Devices and Materials*,” *IEEE Trans. Microw. Theory Techn.*, vol. 50, no. 3, Mar. 2002.

[20] E. Schlomann, *Technical Report R-48*, Research Division, Raytheon Company, Waltham, Massachusetts, 1959 (unpublished).

[21] R.W. Orth, “Frequency-selective limiters and their applications” *IEEE Trans. Electromag. Compat.*, vol. 10, no. 2, pp. 273-283, 1968.

[22] R. Nakane, G. Tanaka, and A. Hirose, “Reservoir computing with spin waves excited in a garnet film,” *IEEE Access*, vol. 6, pp. 4462–4469, Jan. 2018

[23] J. Grollier, D. Querlioz, K. Y. Camsari, K. Everschor-Sitte, S. Fukami and M. D. Stiles, “Neuromorphic spintronics,” Nat. Electron, vol. 3, pp. 360–370, Mar. 2020.

[24] J. Grollier, D. Querlioz, and M. D. Stiles, “Spintronic nanodevices for bioinspired computing,” *Proc. IEEE*, vol. 104, pp. 2024–2039, 2016.

[25] D. D. Awschalom et al., “Quantum engineering with hybrid magnonic systems and materials (Invited Paper),” *IEEE Trans. Quant. Engg.*, vol. 2, pp. 1-36, no. 5500836, 2021.

[26] S. Fauve, *Hydrodynamics and Nonlinear Instabilities*, pp. 387-491, Edited by C. Godreche and P. Manneville, Cambridge, England: Cambridge University Press, 1998.

[27] R.H.J. Grimshaw, N.F. Smyth, Y.A. Stepanyants, “Interaction of internal solitary waves with long periodic waves within the rotation modified Benjamin–Ono equation,” *Physica D: Nonlinear Phenomena*, vol. 419, no. 132867, 2021.

[28] J. Overland, K. Dethloff, J. Francis, R. J. Hall, E. Hanna, S.-J. Kim, J. A. Screen, T. G. Shepherd and T. Vihma, “Nonlinear response of mid-latitude weather to the changing Arctic,” *Nature Clim. Change*, vol. 6, pp. 992–999, Oct. 2016.

[29] R. Boyd, *Nonlinear optics*, 4th edition, London, U.K: Academic Press, 2020.

[30] P. K. Shukla, B. Eliasson, "Nonlinear aspects of quantum plasma physics," *Phys. Usp.*, vol. 53, pp. 51-76, 2010.

[31] B. G. O. Essama, S. N. Essiane, and J. Atangana, “Multi-Sasa Satsuma rogue events and multi-wave trains generation in a nonlinear left-handed transmission line,” *Eur. Phys. J. Plus*, vol. 136, no. 49, Jan. 2021.

[32] S. Kabashima, S. Kogure, T. Kawakubo, and T. Okada, “Oscillatory-to-nonoscillatory transition due to external noise in a parametric oscillator,” *J. Appl. Phys.*, vol. 50, no. 6296, 1979.

[33] B. Yurke, J. S. Denker, "Quantum network theory," *Phys. Rev. A*, vol. 29, no. 3, pp. 1420-1437, Mar. 1984.

[34] T. Kawakubo, A. Yanagita, and S. Kabashima, “External Noise Effect on the Onset of Williams Domain in Nematic Liquid Crystals,” *J. Phys. Soc. Jpn.*, vol. 50, no. 1451, 1981.

[35] D. F. Anderson, "Global Asymptotic Stability for a Class of Nonlinear Chemical Equations," *SIAM J. Appl. Math.*, vol. 68, pp. 1464–1476, 2008.

[36] V. E. Zakharov, R. V. Shamin, A. V. Yudin, “Typical geometry of rogue waves,” *Doklady Earth Sciences*, vol. 462(1), pp. 484-486, May 2015. C. Kharif, E. Pelinovsky, A. Slunyaev, *Rogue waves in the ocean*, Berlin: Springer, 2008.

[37] S. H. Strogatz, D. M. Abrams, A. McRobie, B. Eckhardt and E. Ott, “Crowd synchrony on the Millennium Bridge,” *Nature*, vol. 438, pp. 43–44, Nov. 2005; P. Dallard, T. Fitzpatrick, A. Flint, A. Low, R. R. Smith, M. Willford, M. Roche, "London Millennium Bridge: Pedestrian-Induced Lateral Vibration", *J. Bridge Engg.*, vol. 6(6), pp. 412-417, Dec. 2001.

[38] Veritasium, *The secret of synchronization*, YouTube, Mar. 2021. Available at: https://www.youtube.com/watch?v=t-_VPRCtiUg.

[39] W. Shao, Y. Hu, F. Nunziata, V. Corcione, M. Migliaccio, and X. Li, “Cyclone Wind Retrieval Based on X-Band SAR-Derived Wave Parameter Estimation,” *J. of Atmos. and Oceanic Techn.*, vol. 37, pp. 1907-1924, Oct. 2020.

[40] F. Petrelis, S. Aumaitre, and S. Fauve, “Effect of noise on parametric instabilities,” *Phys. Rev. Lett.*, vol. 94, no. 070603, Feb. 2005.

[41] P. E. Wigen, *Nonlinear Phenomena and Chaos in Magnetic Materials*, Singapore: World Scientific, 1994.

[42] E. Infeld and G. Rowlands, *Nonlinear Waves, solitons and chaos*, 2nd Edition, Cambridge, U.K: Cambridge University Press, 2000.

[43] V.K. Arkad’ev, *Electromagnetic processes in metals*, Part II, Moscow-Leningrad: Main editorial energy literature, 1936.

[44] L. Landau and E. Lifshitz, “On the theory of the dispersion of magnetic permeability in ferromagnetic bodies,” *Phys. Zeitsch. der Sow.*, vol. 8, pp. 153–169, 1935.

[45] A. G. Gurevich and G. A. Melkov, *Magnetization Oscillations and Waves*, Boca Raton, FL, USA: CRC Press, 1996.

[46] A. G. Gurevich, *Ferrites at microwave frequencies*, New York, USA: Consultants Bureau, 1963.

[47] T. L. Gilbert, "A Lagrangian formulation of the gyromagnetic equation of the magnetic field," *Phys. Rev.*, vol. 100(4), p. 1243, 1955. T. L. Gilbert, "A phenomenological theory of damping in ferromagnetic materials," *IEEE Trans. Mag.*, vol. 40 (6), pp. 3443–3449, 2004.

[48] F. Bloch, "Zur Theorie des Ferromagnetismus," *Z. Physk.* (in German), vol. 61, pp. 206–219, 1930.

[49] F.R. Morgenthaler, "Survey of Ferromagnetic Resonance in Small Ferrimagnetic Ellipsoids," *J. Appl. Phys.*, vol. 31, pp. 95S-97S, 1960.

[50] E. Schlomann, J. Green and V. Milano, "Recent Developments in Ferromagnetic Resonance at High Power Levels," *J. Appl. Phys*, vol. 31, p. 386S, 1960.

[51] E. Schlomann "Longitudinal Susceptibility of Ferromagnets in Strong rf Fields," *J. Appl. Phys.*, vol. 33, p. 527, 1962.

[52] N. Bloembergen and R. Damon, "Relaxation Effects in Ferromagnetic Resonance," Phys. Rev., vol. 85, p. 699, 1952.

[53] N. Bloembergen and S. Wang, "Relaxation Effects in Para- and Ferromagnetic Resonance," Phys. Rev., vol. 93, p. 72, 1954.

[54] H. Suhl, "The theory of ferromagnetic resonance at high signal powers," *J. Phys. Chem. Solids*, vol. 1, no. 4, pp. 209–227, Jan. 1957.

[55] E. Schlomann, J. H. Saunder, M. H. Silvertz, “L-Band ferromagnetic resonance at high peak power level,” *Trans. IRE, MTT*, vol. 8, no. 8, pp. 96-100, 1960.

[56] V. E. Zakharov, V. S. L’vov, S. S. Starobinets, “Instability of the monochromatic spin waves,” *Fiz. Tverd. Tela.*, vol. 11, no. 10, pp. 2924-2930, 1969.

[57] V. E. Zakharov, V. S. L’vov, S. S. Starobinets, “Stationary nonlinear theory of parametric excitation of waves,” *Sov. Phys.- JETP*, vol. 32, p. 656, 1971.

[58] V. E. Zakharov, V. S. L'vov, and S. S. Starobinets, “Spin-wave turbulence beyond the parametric excitation threshold,” *Sov. Phys. Usp.*, vol. 17, pp. 896, Dec. 1975.

[59] V. S. L'vov and G. E. Fal'kovich, “On the interaction of parametrically excited spin waves with thermal spin waves,” *Zh. Eksp. Teor. Fi.*, vol. 82, pp. 1562-1577, May 1982.

[60] V.V. Zautkin, V.S. L'vov, S.L. Musher, S.S. Starobinets, Proof of stage-by-stage excitation of parametric spin waves, *Sov. Phys.-JETP Lett.*, vol. 14, p. 206, 1971.

[61] V.V. Zautkin, V.S. L'vov and S.S. Starobinets, “Resonance phenomena in parametric spin wave system,” *Sov. Phys.-JETP*, vol. 36, no. 1, pp. 96-99, 1973.

[62] I. V. Krutsenko, V. S. L'vov, and G. A. Melkov, “Spectral density of parametrically excited waves,” *Sov. Phys. JETP*, vol. 48, no. 3, Sep. 1978.

[63] V.S. L'vov and A.M. Rubenchik, ”Nonlinear Theory of the Parametric Instability of Waves in a Plasma,” *Sov. Phys.-JETP*, vol. 37, no. 2, pp. 263-268, 1973.

[64] V. P. Seminozhenko, V. L. Sobolev, and A. A. Yatsenko, “Excitation of spin waves by parallel pumping in ferromagnets with magnetic imhomogeneities,” *Sov. Phys. JETP*, vol. 51, no. 5, May 1980.

[65] B. I. Orel and S. S. Starobinets, “Radio-frequency magnetic susceptibility and collective resonance of magnons in parallel pumping,” *Sov. Phys.-JETP*, vol. 41, no.1, 1975.

[66] V.S. L'vov and M.I. Shirokov, “Nonlinear Theory of Parametric Excitation of Spin Waves in Antiferromagnets,” *Sov. Phys.- JETP*, vol. 40, p. 960, 1975.

[67] T. S. Hartwick, E. R. Peressini, M. T. Weiss, “Subsidiary resonance in YIG,” *J. Appl. Phys.*, vol. 32, p. S223, 1961.

[68] T. Schneider, A. A. Serga, B. Leven, B. Hillebrands, “Realization of spin-wave logic gates,” *Appl. Phys. Lett.*, vol. 92, no. 022505, 2008.

[69] A. Mahmoud, F. Ciubotaru, F. Vanderveken, A. V. Chumak, S. Hamdioui, C. Adelmann, S. Cotofana, “Introduction to spin wave computing”, *J. Appl. Phys.*, vol. 128, no. 161101, 2020.

[70] J.-N. Toedt, M. Mundkowski, D. Heitmann, S. Mendach, and W. Hansen, “Design and construction of a spin-wave lens,” *Sci. Rep.*, vol. 6, no. 33169, 2016.

[71] T. Fischer, M. Kewenig, D. A. Bozhko, A. A. Serga, I. I. Syvorotka, F. Ciubotaru, C. Adelmann, B. Hillebrands, and A. V. Chumak, “Experimental prototype of a spin-wave majority gate,” *Appl. Phys. Lett.*, vol. 110, no. 152401, 2017.

[72] A. Purbawati, F. Garcia-Sanchez, L. D. Buda-Prejbeanu, and U. Ebels, “Enhanced modulation rates via field modulation in spin torque nano-oscillators,” *Appl. Phys. Lett.*, vol. 108, no. 122402, 2016.

[73] V. G. Harris *et al.*, “Recent advances in processing and applications of microwave ferrites,” *J. Magn. Mat.*, vol. 321, pp. 2035–2047, 2009.

[74] S. O. Demokritov, V. E. Demidov, O. Dzyapko, G. A. Melkov, A. A. Serga, B. Hillebrands and A. N. Slavin, “Bose–Einstein condensation of quasi-equilibrium magnons at room temperature under pumping,” *Nature*, vol. 443, pp. 430–433, 2006.

[75] J. Xu, C. Zhong, X. Zhou, X. Han, D. Jin, S. K. Gray, L. Jiang, X. Zhang, “Coherent pulse echo in hybrid magnonics with multimode phonons,” *Phys. Rev. Appl.*, vol. 16, no. 024009, 2021.

[76] R. W. Damon, “Relaxation effects in the ferromagnetic resonance,” *Rev. Mod. Phys.*, vol. 25, no. 1, p. 239, 1953.

[77] P. W. Anderson and H. Suhl, “Instability in the Motion of Ferromagnets at High Microwave Power Levels,” *Phys. Rev.*, vol. 100, no. 1788, Dec. 1955.

[78] H. Suhl, “The Nonlinear Behavior of Ferrites at High Microwave Signal Levels,” *Proc. IRE*, vol. 44, no. 10, pp. 1270-1284, Oct. 1956.

[79] H. Suhl, “Origin and Use of Instabilities in Ferromagnetic Resonance,” *J. Appl. Phys.*, vol. 29, no. 416, 1958.

[80] M. T. Kief, R. H. Victora, Materials for heat-assisted magnetic recording, *MRS Bull.*, vol. 43, pp. 87-92, Feb. 2018.

[81] L. Pan, D. Bogy, “Heat-assisted magnetic recording,” *Nat. Phot.*, vol. 3, pp. 189–190, 2009.

[82] D. Weller, A. Lyberatos, D. Mitin, N. Y. Safonova, M. Albrecht, “FePt heat assisted magnetic recording media,” *J. Vac. Sci. Techn.*, vol. B34, no. 060801, 2016.

[83] R. E. Rottmayer *et al*., “Heat-Assisted Magnetic Recording," *IEEE Trans. Magn.*, vol. 42, no. 10, pp. 2417-2421, Oct. 2006.

[84] A. Ghoreyshi and R. H. Victora, “Heat assisted magnetic recording with patterned FePt recording media using a lollipop near field transducer,” *J. Appl. Phys.*, vol. 115, no. 17B719, Feb. 2014.

[85] T. R. Albrecht et al., “Bit-Patterned Magnetic Recording: Theory, Media Fabrication, and Recording Performance,” *IEEE Trans. on Magn.*, vol. 51, no. 5, pp. 1-42, May 2015.

[86] R. Ruiz, E. Dobisz, T. R. Albrecht, “Rectangular Patterns Using Block Copolymer Directed Assembly for High Bit Aspect Ratio Patterned Media,” *ACS Nano*, vol. 5, no. 1, pp. 79–84, 2011.

[87] R. A. Griffiths, A. Williams, C. Oakland, J. Roberts, A. Vijayaraghavan, T. Thomson, “Directed self-assembly of block copolymers for use in bit patterned media fabrication,” *J. Phys. D: Appl. Phys.*, vol. 46, no. 503001, 2013.

[88] A. Kikitsu, “Prospects for bit patterned media for high-density magnetic recording,” *J. Mag. Magn. Mat.*, vol. 321, pp. 526– 530, 2009.

[89] R. H. Victora and Xiao Shen, “Composite media for perpendicular magnetic recording,” *IEEE Trans. Magn.*, vol. 41, no. 2, pp. 537-542, Feb. 2005.

[90] R. H. Victora and X. Shen, “Exchange coupled composite media for perpendicular magnetic recording,” *IEEE Trans. on Magn.*, vol. 41, no. 10, pp. 2828-2833, Oct. 2005.

[91] Z. Liu, Y. Jiao, and R. H. Victora, “Composite media for high density heat assisted magnetic recording,” *Appl. Phys. Lett.*, vol. 108, no. 232402, 2016.

[92] C. Mellor, BPM and HAMR. Available at https://rogerluethy.wordpress.com/2011/07/14/bpm-and-hamr/.

[93] J. Towns, T. Cockerill, M. Dahan, I. Foster, K. Gaither, A. Grimshaw, V. Hazlewood, S. Lathrop, D. Lifka, G. D. Peterson et al., "XSEDE: Accelerating Scientific Discovery," *Comput. Sci. Eng.*, vol. 16(5), pp. 62–74, 2014.

[94] A. Fert, V. Cros, J. Sampaio, "Skyrmions on the track," *Nat. Nano.*, vol. 8, pp. 152-156, 2013.

[95] A. K. C. Tan, P. Ho, J. Lourembam, L. Huang, H. K. Tan, C. J. O. Reichhardt, C. Reichhardt and A. Soumyanarayanan, "Visualizing the strongly reshaped skyrmion Hall effect in multilayer wire devices," *Nat. Comm.*, vol. 12, no. 4252, 2021.

[96] M. M. Otrokov *et al*., "Prediction and observation of an antiferromagnetic topological insulator," *Nature*, vol. 576, pp. 416–422, 2019.

[97] S. O. Democritov (Editor), *Spin wave confinement*, Singapore: Pan Stanford, 2009.

[98] T. Bose, S. Trimper, "Correlation effects in the stochastic Landau-Lifshitz-Gilbert equation," *Phys. Rev. B*, vol. 81, no. 104413, 2010.

[99] J. L. Garcia-Palacios and F. J. La'zaro, **"**Langevin-dynamics study of the dynamical properties of small magnetic particles," *Phys. Rev. B*, vol. 58, no. 22, Dec. 1998.

[100] E. Date, M. Jimbo, M. Kashiwara, T. Miwa, "Landau-Lifshitz equation: solitons, quasi-periodic solutions and infinite-dimensional Lie algebras," *J. Phys. A: Math. Gen.*, vol. 16, no. 221, 1983.

[101] D. B. Kirk, W.-M. W. Hwu, *Programming massively parallel processors: A hands on approach*, 3rd edition, Cambridge, Massachusetts, USA: Elsevier, 2017.

[102] NVIDIA Official Website. Available at: https://www.nvidia.com/en-gb/graphics-cards/.

[103] A. Venugopal, A. Ghoreyshi, and R. H. Victora, “High-density shingled heat-assisted recording using bit-patterned media subject to track misregistration,” *IEEE Trans. Magn.*, vol. 53 (11), no. 3101804, Nov. 2017.

[104] T. Taniguchi, “Theoretical condition for switching the magnetization in a perpendicularly magnetized ferromagnet via the spin Hall effect,” *Phys. Rev. B*, vol. 100, no. 174419, Nov. 2019.

[105] J. Xue, R. H. Victora, "Micromagnetic predictions for thermally assisted reversal over long time scales," *Appl. Phys. Lett.*, vol. 77, no. 3432, Nov. 2000.

[106] P.-W. Huang, “Micromagnetic study of heat assisted magnetic recording using renormalized media cells,” Ph.D. Dissertation, Dept. of Electrical and Computer Engineering, Univ. of Minnesota, Minneapolis, USA, May 2014.

[107] A. Venugopal, T. Qu, R. H. Victora, “Parallel computations based Micromagnetic Solver and Analysis Tools for Magnon-Microwave Interaction Studies,” (To be published.)

[108] W. F. Brown, “Thermal Fluctuations of a Single-Domain Particle,” *Phys. Rev.*, vol. 130, no. 5, pp. 1677–1686, 1963.

[109] R. C. O’Handley, *Modern Magnetic Materials Principles and Applications*, NJ, US: Wiley Interscience, 2000.

[110] V. S. L’vov, *Wave Turbulence Under Parametric Excitation: Applications to Magnets*, New York, NY, USA: Springer-Verlag, 1994.

[111] C. Kittel, “Interpretation of Anomalous Larmor Frequencies in Ferromagnetic Resonance Experiment,” *Phys. Rev.*, vol. 71, p. 270, 1947.

[112] A. Venugopal, T. Qu and R. H. Victora, “Nonlinear Parallel-Pumped FMR: Three and Four Magnon Processes,” *IEEE Trans. Microw. Theory Tech.,* vol. 68, no. 2, pp. 602-610, Feb. 2020.

[113] M. Goryachev, W. G. Farr, D. L. Creedon, Y. Fan, M. Kostylev, and M. E. Tobar, “High-Cooperativity Cavity QED with Magnons at Microwave Frequencies,” Phys. Rev. Appl., vol. 2, 054002, Nov. 2014.

[114] A. J. Newell, W. Williams, and D. J. Dunlop, “A generalization of the demagnetizing tensor for non-uniform magnetization,” *J. Geophys. Res., sSolid Earth*, vol. 98, no. B6, pp. 9551–9555, 1993.

[115] T. Qu, A. Venugopal et al., “Nonlinear Magnon Scattering Mechanism for Microwave Pumping in Magnetic Films”, IEEE Access, vol. 8, pp. 216960-216968, Nov. 2020.

[116] A. Venugopal, T. Qu and R. H. Victora, “Manipulation of nonlinear magnon effects using a secondary microwave frequency,” *Appl. Phys. Lett.*, vol. 117,152404, Oct. 2020.

[117] H. G. Bauer, P. Majchrak, T. Kachel, C. H. Back and G. Woltersdorf, “Nonlinear spin-wave excitations at low magnetic bias fields,” *Nat. Comm.*, vol. 6, no. 8274, 2015.

[118] J-N. Toedt and W. Hansen, “Dynamic control of spin-wave propagation,” *Sci. Rep.*, vol. 11, article no. 7821, Apr. 2021.

[119] B. A. Kalinikos and A. N. Slavin, “Theory of dipole-exchange spin wave spectrum for ferromagnetic flms with mixed exchange boundary conditions,” *J. Phys. C Solid State Phys.*, vol. 19, 7013, May 1986.

[120] J. D. Adam and S. N. Stitzer, “FSLs for high dynamic range microwave receivers,” *IEEE Trans. Microw. Theory Techn.*, vol. 41, no. 12, pp. 2227-2231, Dec. 1993.

[121] S. M. Rezende and F. M. De Aguiar, “Spin-Wave Instabilities, Auto-Oscillations and Chaos in Yttrium-Iron-Garnet,” *Proc. IEEE*, vol. 78, no. 6, Jun. 1990.

[122] T. Holstein and H. Primakoff, “Field dependence of the intrinsic domain magnetization of a ferromagnet,” Phys. Rev., vol. 58, pp. 1098–1113, Dec. 1940.

[123] E. Schlomann, “Ferromagnetic relaxation caused by interaction with thermally excited magnons,” *Phys. Rev.*, vol. 121, pp. 1312-1319, 1961.

[124] C. Kittel, *Quantum Theory of Solids*, New York, USA: Wiley, 1987.

[125] H. Suhl, “Theory of the magnetic damping constant,” *IEEE Trans. Magn.*, vol. 34, no. 4, pp. 1834-1838, Jul. 1998.

[126] H. Suhl, *Relaxation processes in micromagnetics*, New York, USA: Oxford, 2007.

[127] E. Schlomann, and J. J. Green, “Spin-wave growth under parallel pumping,” *J. Appl. Phys.*, vol. 34, p. 1291-1293, 1963.

[128] P. Gottlieb, H. Suhl, “Saturation of ferrimagnetic resonance with parallel pumping,” *J. Appl. Phys.*, vol. 33, p. 1508, 1962.

[129] A. Venugopal, T. Qu and R. H. Victora, “Dependence of the Threshold Field Intensity of Ferrite Films on Intrinsic Damping and Secondary Microwave Signal,” *IEEE Trans. Magn.*, doi: 10.1109/TMAG.2021.3087522.

[130] P. Kabos, C. E. Patton, G. Wiese, A. D. Sullins, E. S. Wright, L. Chen, “Butterfly curves and critical modes for second-order spin-wave instability processes in yttrium iron garnet films,” *J. Appl. Phys.*, vol. 80, pp. 3962-3971, 1996.

[131] M. G. Cottam, *Linear and Nonlinear Spin Waves in Magnetic Films and Superlattices*, Singapore: World Scientific, 1994.

[132] S. M. Morgan and R. H. Victora, "Use of square waves incident on magnetic nanoparticles to induce magnetic hyperthermia for therapeutic cancer treatment," *Appl. Phys. Lett.*, vol. 97, no. 093705, Aug. 2010.

[133] N. Perez and L. Lopez-Diaz, "Magnetic field induced spin-wave energy focusing," Phys. Rev. B, *Condens. Matter*, vol. 92, no. 014408, Jul. 2015.

[134] C. Kittel, "On the theory of ferromangetic resonance absorption," *Phys. Rev.*, vol. 73, pp. 155–161, 1948.

[135] H. Kurebayashi, O. Dzyapko, V. E. Demidov, D. Fang, A. J. Ferugson, and S. O. Demokritov, "Controlled enhancement of spin-current emission by three-magnon splitting," *Nat. Mater.*, vol. 10, pp. 660–664, Sep. 2011.

[136] A. Y. Dobin and R. H. Victora, "Intrinsic nonlinear ferromagnetic relaxation in thin metallic films," *Phys. Rev. Lett.*, vol. 90 (16), no. 167203, Apr. 2003.

[137] J. D. Adam and S. N. Stitzer, "Frequency selective limiters for high dynamic range microwave receivers," *IEEE Trans. Microw. Theory Techn.*, vol. 41, no. 12, pp. 2227–2231, Dec. 1993.

[138] C. Vittoria, *Microwave Properties of Magnetic Films*, Singapore: World Scientific, 1993.

[139] D. Stancil and A. Prabhakar, *Spin Waves: Theory and Applications*, New York, USA: Springer, 2009.

[140] H. Kurebayashi, O. Dzyapko, V. E. Demidov, D. Fang, A. J. Ferguson, and S. O. Demokritov, “Spin pumping by parametrically excited short-wavelength spin waves,” *Appl. Phys. Lett.*, vol. 99, no. 162502, Oct. 2011.

[141] S. Flugge and H. P. J. Wijn, *Encyclopedia of Physics Ferromagnetism*, New York, NY, USA: Springer-Verlag, 1966.

[142] M. C. Onbasli *et al.*, “Pulsed laser deposition of epitaxial yttrium iron garnet films with low Gilbert damping and bulk-like magnetization,” *APL Mater.*, vol. 2, no. 106102, Oct. 2014.

[143] OOMMF User’s Guide for Release 2.0 Alpha 1. [Online]. Available: https://math.nist.gov/oommf/doc/, Sep. 2018.

[144] C. Patton, F. Ono, and M. Takahashi, “Direct evidence for a two-magnon contribution to the FMR relaxation in Ni-Fe thin films,” *IEEE Trans.Magn.*, vol. 7, no. 3, pp. 760–763, Sep. 1971.

[145] M. J. Hurben and C. E. Patton, “Theory of two magnon scattering microwave relaxation and ferromagnetic resonance linewidth in magnetic thin films,” *J. Appl. Phys.*, vol. 83, no. 8, pp. 4344–4365, Apr. 1998.

[146] A. O. Boryssenko, S. M. Gillette, M. Y. Koledintseva, “Nonlinear loss model in absorptive-type ferrite frequency-selective limiters,” *IEEE Trans. Microw. Theory Tech.*, vol. 67, no. 12, pp. 4871-4880, Dec. 2019.

[147] T. Qu, A. Venugopal, and R. H. Victora, “Dependence of Nonlinear Magnon Characteristics on Material Properties”, *J. Appl. Phys*, vol. 129, 163903, Apr. 2021.

[148] J. Roychowdhury, "Boolean Computation Using Self-Sustaining Nonlinear Oscillators," *Proc. IEEE,* vol. 103, no. 11, pp. 1958-1969, Nov. 2015.

[149] S. Residori, R. Berthet, B. Roman, and S. Fauve, "Noise Induced Bistability of Parametric Surface Waves," *Phys. Rev. Lett.*, vol. 88, no. 024502, Dec. 2001.

[150] H. Suhl, "Restoration of Stability in Ferromagnetic Resonance," *Phys. Rev. Lett.*, vol. 6, p. 174, Feb. 1961.

[151] T. S. Hartwick, E. R. Peressini, and M. T. Weiss, "Suppression of Subsidiary Absorption in Ferrites by Modulation Techniques," *Phys. Rev. Lett.*, vol. 6, p. 176, 15 Feb. 1961.

[152] F. R. Morgenthaler, F. A. Olsen, and G. E. Bennett, "Suppression of spin wave instabilities associated with ferromagnetic resonance," *Proc. Intrnl. Conf. Magn. Cryst.*, Volume I. Magnetism, Kyoto, pp. 411–415, Sep. 1961.

[153] V. V. Zautkin, V. S. L'vov, B. I. Orel, and S. S. Starobinets, "Large-amplitude collective oscillations and the double parametric resonance of magnons," *J. Exp. Theor. Phys.*, vol. 45, pp. 143–149, 1977.

[154] V. E. Demidov, S. Urazhdin, A. Anane, V. Cros, and S. O. Demokritov, Spin–orbit-torque magnonics, J. Appl. Phys., vol. 127, no. 170901, 2020.

[155] J. D. Adam and S. N. Stitzer, "MSW frequency selective limiters at UHF," *IEEE Trans. Magn.*, vol. 40, no. 4, pp. 2844-2846, Jul. 2004.

[156] G. Loubens, V. V. Naletov, and O. Klein, "Reduction of the spin-wave damping induced by nonlinear effects," *Phys. Rev. B,* vol. 71, no. 180411, 2005.

[157] F. M. de Aguiar and S. M. Rezende, “Observation of Subharmonic Routes to Chaos in Parallel-Pumped Spin Waves in Yttrium Iron Garnet,” *Phys. Rev. Lett.*, vol. 56, no. 1070, Mar. 1986.

[158] M. Hansen, I. Lisenkov, H. Liu, A. Jander, P. Dhagat, “Correlation of Binary-Code-Modulated Microwave Signals by Parametric Pumping of Spin Waves,” *IEEE Magn. Lett.*, vol. 11, no. 5505105, 2020.

[159] A. Eklund *et al.*, “Dependence of the colored frequency noise in spin torque oscillators on current and magnetic field,” *Appl. Phys. Lett.*, vol. 104, no. 092405, 2014.

[160] R. Hertel, R. Wulfhekel, J. Kirschner, “Domain-wall induced phase shifts in spin waves,” *Phys. Rev. Lett.*, vol. 93, no. 257202, 2004.

[161] L.-J. Chang, Y.-F. Liu, M.-Y. Kao, L.-Z. Tsai, J.-Z. Liang, S.-F. Lee, “Ferromagnetic domain walls as spin wave filters and the interplay between domain walls and spin waves,” *Sci. Rep.*, vol. 8, no. 3910, 2018.

[162] C. Bayer, H. Schultheiss, B. Hillebrands, R. L. Stamps, “Phase shift of spin waves traveling through a 180° Bloch-domain wall,” *IEEE Trans. Magn.*, vol. 41, no. 10, pp. 3094-3096, Oct. 2005.

[163] Sebastian Macke and Dagmar Goll, “Transmission and reflection of spin waves in the presence of Néel walls,” *J. Phys.: Conf. Ser.*, vol. 200, no. 042015, 2010.

[164] M. Covington, T. M. Crawford, G. J. Parker, “Time-resolved measurement of propagating spin waves in ferromagnetic thin films,” *Phys. Rev. Lett.*, vol. 89, no. 237202, 2002.

[165] M. Sparks, R. Loudon, C. Kittel, “Ferromagnetic relaxation. I. Theory of the relaxation of the uniform precession and the degenerate spectrum in insulators at low temperatures,” *Phys. Rev.*, vol. 122, pp. 791, 1961.

[166] J.-V. Kim, V. Tiberkevich, A. N. Slavin, “Generation linewidth of an auto-oscillator with a nonlinear frequency shift: spin-torque nano-oscillator,” *Phys. Rev. Lett.*, vol. 100, no. 017207, 2008.

[167] M. W. Keller, A. B. Kos, T. J. Silva, W. H. Rippard, M. R. Pufall, “Time domain measurement of phase noise in a spin torque oscillator,” *Appl. Phys. Lett.*, vol. 94, no. 193105, 2009.

[168] T. J. Silva, and W. H. Rippard, “Developments in nano-oscillators based upon spin-transfer point-contact devices,” *J. Magn. Magn. Mater.*, vol. 320, pp. 1260–1271, 2008.

[169] T. J. Silva and M. W. Keller, “Theory of Thermally Induced Phase Noise in Spin Torque Oscillators for a High-Symmetry Case,” *IEEE Trans. Magn.*, vol. 46, no. 9, pp. 3555-3573, Sept. 2010.

[170] L. Yang *et al.*, “Reduction of phase noise in nanowire spin orbit torque oscillators,” *Sci. Rep.*, vol. 5, no. 16942, 2015.

[171] T. Nagasawa, K. Mizushima, H. Suto, K. Kudo, R. Sato, “Amplitude noise in spin-torque oscillators,” *Appl. Phys. Exp.*, vol. 4(6), no. 063005, 2011.

[172] C. M. Bender and S. A. Orszag, *Advanced Mathematical Methods for Scientists and Engineers*, pp. 549–551, Delhi, India: Springer, 2013.

[173] A. Venugopal and R. H. Victora, “Effective phase noise considerations in magnon based parametric excitations,” *Sci. Rep.*, vol. 11, no. 11322, 2021.

[174] N. Zhu, X. Zhang, X. Han, C.-L. Zou, C. Zhong, C.-H. Wang, L. Jiang, H. X. Tang, "Waveguide cavity optomagnonics for microwave-to-optics conversion," *Optica*, vol. 7(10), pp. 1291-1297, 2020.

[175] D. A. Bozhko, P. Clausen, G. A. Melkov, V. S. L'vov, A. Pomyalov, V. I. Vasyuchka, A. V. Chumak, B. Hillebrands, and A. A. Serga, "Bottleneck Accumulation of Hybrid Magnetoelastic Bosons," *Phys. Rev. Lett.*, vol. 118, no. 237201 , 2017.

[176] A. Venugopal, R. H. Victora, "Dynamic Threshold Control and Higher-Order Processes for Magnetics Based Microwave Devices," *Intnl. Microw. Symp.*, Atlanta, Georgia, USA, Jun. 2021.

[177] V. E. Zakharov, V. S. L'vov, and S. L. Musher, "Transient behavior of a system of parametrically excited spin waves," *Sov. Phys. – Solid State*, vol. 14, p. 710, 1972.

[178] V.P. Krasitskii, "Canonical transformation in a theory of weakly nonlinear waves with a nondecay dispersion law," *Sov. Phys. JETP*, vol. 71, p. 921, 1990.

[179] K. Ando, E. Saitoh, "Spin pumping by bistable exchange spin waves," *Phys. Rev. Lett.*, vol. 109, no. 026602, 2012.

[180] M. Sparks, *Ferromagnetic relaxation theory*, USA: McGraw-Hill, 1964.

[181] H. J. J. Liu, G. A. Riley, C. L. Ordóñez-Romero, B. A. Kalinikos, K. S. Buchanan, "Time-resolved study of nonlinear three-magnon processes in yttrium iron garnet films," *Phys. Rev. B*, vol. 99, no. 024429, 2019.

[182] H. Le Gall, B. Lemair, D. Sere: Solid State Comm., vol. 5, no.12, p. 919, 1967.

[183] R. H. Victora, P.-W. Huang, A. Ghoreyshi, and S. Wang, "Noise mitigation in granular and bit-patterned media for HAMR," *IEEE Trans. Magn.*, vol. 51, no. 3200307, Apr. 2015.

[184] C. Vogler et al., "Heat-assisted magnetic recording of bit-patterned media beyond 10 Tb/in^2," *Appl. Phys. Lett.*, vol. 108, p. 102406, Mar. 2016.

[185] R. H. Victora, Y. Wang, and S. Wang, "Shingled magnetic recording on bit patterned media at 10 Tb/in^2," *IEEE Trans. Magn.*, vol. 49, no. 7, pp. 3644–3647, Jul. 2013.

[186] S. J. Greaves et al., "Microwave-assisted magnetic recording on dual thickness and dual-layer bit-patterned media," *IEEE Trans. Magn.*, vol. 52, no. 7, Jul. 2016, Art. no. 3000904.

[187] A. Ghoreyshi and R. H. Victora, "Heat assisted magnetic recording with patterned FePt recording media using a lollipop near field transducer," *J. Appl. Phys.*, vol. 115, p. 17B719, Feb. 2014.

[188] R. H. Victora and S. Wang, "Simulation of expected areal density gain for heat-assisted magnetic recording relative to other advanced recording schemes," IEEE Trans. Magn., vol. 51, no. 11, Nov. 2015, Art. no. 3201307.

[189] R. H. Victora, S. Wang, P. Huang, and A. Ghoreyshi, "Noise mitigation in granular and bit-patterned media for HAMR," *IEEE Trans. Magn.*, vol. 51, no. 4, Apr. 2015, Art. ID 3200307.

[190] S. Wang, A. Ghoreyshi, and R. H. Victora, "Feasibility of bit patterned media for HAMR at 5 Tb/in2," *J. Appl. Phys.*, vol. 117, p. 17C115, Mar. 2015.

[191] J. Barker, R. F. L. Evans, R. W. Chantrell, D. Hinzke, and U. Nowak, “Atomistic spin model simulation of magnetic reversal modes near the Curie point,” Appl. Phys. Lett., vol. 97, no. 19, p. 192504, 2010.

[192] S. Wang, M. Mallary, and R. H. Victora, “Thermal switching distribution of FePt grains through atomistic simulation,” IEEE Trans. Magn., vol. 50, no. 11, p. 3203304, 2014.

[193] Evans, R.L, PhD Thesis (Atomistic Modelling of Nanogranular magnetic materials), University of York**.**

[194] N. Goldenfeld, *Lectures on phase transitions and the renormalization group*, Levant Books, 2005.

[195] R. H. Victora and P. Huang, "Simulation of Heat-Assisted Magnetic Recording Using Renormalized Media Cells,” *IEEE Trans. Magn.*, vol. 49, no. 2, pp. 751-757, Feb. 2013.

[196] R.H Victora, S. Wang, “Noise Mitigation in Granular and Bit-Patterned Media for HAMR,” *IEEE Trans. Magn.* Vol 51, no.4, 3200307, 2015.

[197] S. Wang, R. H. Victora, “Temperature distribution of granular media for heat assisted magnetic recording,” *J. Appl. Phys.*, vol. 117, p. 17D147, Apr. 2015.

[198] H. J. Richter et al., “Recording on bit-patterned media at densities of 1Tb/in2 and beyond,” *IEEE Trans. Magn.*, vol. 42, no. 10, pp. 2255–2260, Oct. 2006.

[199] T. W. McDaniel, “Areal density limitation in bit-patterned, heat-assisted magnetic recording using FePtX media,” *J. Appl. Phys.*, vol. 112, p. 093920, Nov. 2012.

[200] Y. Jiao, Z. Liu, and R. H. Victora, “Renormalized anisotropic exchange for representing heat assisted magnetic recording media,” *J. Appl. Phys.*, vol. 117, p. 17E317, Mar. 2015.

[201] D. Suess et al., “Fundamental limits in heat-assisted magnetic recording and methods to overcome it with exchange spring structures,” *J. Appl. Phys.*, vol. 117, p. 163913, Apr. 2015.

[202] L. Wan et al., “The limits of lamellae-forming PS-b-PMMA block coploymers for lithography,” *ACS Nano*, vol. 9, no. 7, pp. 7506–7514, Jun. 2015.